Stony Brook University

The electronic structures of organic molecules on metal surface and size-selected clusters on oxide surface

A Dissertation Presented

by

Jing Zhou

to

The Graduate School

in Partial Fulfillment of the

Requirements

for the Degree of

Doctor of Philosophy

in

Chemistry

Stony Brook University

August 2011

Stony Brook University

The Graduate School

Jing Zhou

We, the dissertation committee for the above candidate for the

Doctor of Philosophy degree, hereby recommend

acceptance of this dissertation.

Michael G. White, Ph. D., Advisor
Professor, Department of Chemistry

Trevor Sears, Ph. D., Chairperson of Defense
Professor, Department of Chemistry

Jose Rodriguez, Ph. D., Third Member
Senior Chemist, Brookhaven National Laboratory

Dario Stacchiola, Ph. D., Outside Member
Assistant Chemist, Brookhaven National Laboratory

This dissertation is accepted by the Graduate School

Lawrence Martin
Dean of the Graduate School

Abstract of the Dissertation

The electronic structures of organic molecules on metal surface and size-selected clusters on oxide surface

by

Jing Zhou

Doctor of Philosophy

in

Chemistry

Stony Brook University

2011

In order to improve the performance of molecular electronics and catalysts, it is important to understand the electronic structures of adsorbed molecules or clusters on surfaces. The work presented in this thesis focuses on the characterization of the electronic properties and their relationship with geometric structures using two-photon photoemission, scanning tunneling microscopy and other surface analysis techniques.

Mainly, two types of systems have been studied. One is adsorbed organic molecules (thiophene and aromatic diisocyanides) on a Au(111) surface. On the surface, phenyl diisocyanide molecules lie flat and form one-dimensional molecular chain structures after thermal treatment at 300 K. The molecular chain extends the length of the Au terraces and is composed of alternating diisocyanide molecule and Au adatom in a unit cell. Accompanying the formation of chain structures, photoemission experiments show an unusually large drop in the

work function and the appearance of an unoccupied state at 3.3 eV above the Fermi level. Density functional theory calculations support the favorable energetics for diisocyanide-Au_{ad} bonding and reveal a dipole moment at the interface that results from the molecular chain structure. The dipole moment explains the observed large work function change. Given their considerable length, tunabilities and novel electronic properties, the self-assembled molecular diisocyanide structures may find application as molecular conductors in nanoelectronics.

The other systems investigated are size-selected molybdenum sulfide clusters (Mo_xS_y; x/y = 2/6, 4/6, 6/8, 7/10) deposited on a ultrathin alumina film formed on a NiAl(110) surface. The clusters are produced in a gas-phase magnetron sputtering source and mass-selected prior to being deposited on surface (soft landing). With clusters on the alumina film, the work function determined by 2PPE increases, which is attributed to electron transfer from the alumina substrate to the cluster. The change in work function versus coverage is found to be cluster dependent, but does not simply correlate with cluster size. Interfacial dipole moments derived from the work function measurements are largest for the highly symmetric Mo_4S_6 and Mo_6S_8 clusters which have no permanent dipole. These results suggest strong cluster-support interactions that result in significant interfacial charge transfer.

Table of Contents

List of Tables

List of Figures

List of Abbreviations

2PPE: Two-photon Photoemission

AES: Auger Electron Spectroscopy

BBO: Beta Barium Borate

BPDI: 4,4'-biphenyl diisocyanide

DC: Direct Current

fs: femtosecond

FWHM: Full Width Half Maximum

HOMO: Highest Occupied Molecular Orbital

IPES: Inverse Photoemission Spectroscopy

LDOS: Local density of states

LN_2: Liquid Nitrogen

LUMO: Lowest Unoccupied Molecular Orbital

ML: Monolayer

OLED: Organic Light Emitting Diode

PDI: 1,4-phenylene diisocyanide

PDOS: Projected Density of States

RF: Radio Frequency

SAM: Self-Assembled Monolayer

SHG: Second-Harmonic Generation

STM: Scanning Tunneling Microscopy

STS: Scanning Tunneling Spectroscopy

THG: Third-Harmonic Generation

TPD: Temperature Programmed Desorption

UHV: Ultrahigh Vacuum

UPS: Ultraviolet Photoemission Spectroscopy

XPS: X-ray Photoemission Spectroscopy

Acknowledgements

In my graduate study, I received many generous help and support from many people. Without them, I would not be here today. First, I would like to thank my advisor Dr. Michael White for his guidance and advice for my research and life. He has always been a kind and helpful mentor for his great insights and enthusiasm in science. Also I wish to thank Dr. Nicholas Camillone III and my committee members, Dr. Trevor Sears, Dr. Philip Johnson and Dr. Jose Rodriguez for their time and efforts provided on all my meetings and career development.

In addition, I am grateful to many people in Brookhaven National Laboratory for their support of my research, especially Dr. Ping Liu and Dr. Yan Li, who performed the theoretical work presented in this dissertation. I would also like to thank all my group members for their help and advices on my research and this dissertation. I had wonderful working experiences with them.

Finally, I would particularly like to thank the most important people throughout my PhD period, Dr. Xiaohui Peng, for the encouragement, support and advice she had given me. I am forever indebted to my family for their love and support during the past years.

Chapter 1. Introduction

The interfacial electronic properties of adsorbates on solid surfaces have been extensively investigated because they play a critical role in the performance of molecular electronics and heterogeneous catalysts.[1-4] This dissertation focuses on the electronic structures at the interface of adsorbed organic molecules on metal surfaces and size-selected clusters deposited on oxide surfaces to better understand their relationship with adsorption geometry and the structure of adsorbates.

When two materials are placed in contact, the two Fermi levels will shift to the same level through a local exchange of charge carriers. The interfacial electronic structure resulting from the exchange of charges is fairly well understood for bulk materials such as the well-known Schottky barrier at the metal/inorganic semiconductor interface. When the size of one material is reduced down to nanoscale or single molecular scale, the information about the electronic configuration at the interface is limited although the interfacial electronic properties are critically important for many technical issues. For instance, the efficiency of an organic light emitting diodes (OLED) is determined by the energetic alignment of the HOMO (highest occupied molecular orbital) or LUMO (lowest unoccupied molcuar orbital) of the organic molecule relative to the metal Fermi level.[5,6] The electronic interaction between the molecule and the surface is different with that between bulk materials. For example, the chemisorbed molecules on a surface always form bonds with surface atoms. The adsorbate-surface bonds affect not only the relative positions of molecular orbitals with respect to the surface Fermi level, but also the interfacial electronic coupling. In addition, there is no significant dispersion of electronic states in bonding molecules because the interaction between surface and adsorbed molecule is localized.

There are several techniques to probe the electronic structure at interfaces. Ultraviolet photoemission spectroscopy (UPS) is the most widely used technique to characterize valence electronic structure at interfaces.[7] The adsorption of an UV photon (the photon energy is larger than the work function of investigated system and normally no more than 100 eV) by the surface ejects an electron which is detected by an electron energy analyzer. The kinetic energy of the photoelectron reflects the density of occupied states below the Fermi level. Another technique, inverse photoemission spectroscopy (IPES) probes unoccupied electronic states above the Fermi level. In IPES, an electron beam (<20 eV) with a defined energy is directed on surface. These electrons decay to unoccupied states and the photons emitted in the decay process are detected. The energy resolution in IPES is low due to the relatively high electron energy used and the signal level is low.

Compared to UPS and IPES, two-photon photoemission (2PPE) spectroscopy can detect occupied and unoccupied states simultaneously and can be carried out in a time-resolved manner to study dynamics.[8] The principle of 2PPE technique is illustrated in Figure 1.1. The first photon excites electrons from an occupied state to an intermediate electronic state and the second photon ionizes the electron from the transient state to a final state above the vacuum level (the photon energies of both photons are smaller than the work function of the studied system to avoid one-photon photoemission). The intermediate state can be an image potential state, an unoccupied molecular state or a mixed state resulting from the coupling of molecular orbital to the image potential state or surface states. Besides the possible processes shown in Figure 1.1, the adsorption of the first photon can occur on the adsorbed molecule, followed by the ionization of the excited molecular state by the second photon or a coherent adsorption of the second photon by the molecule. The ejected electron is analyzed in energy, momentum and time. The kinetic

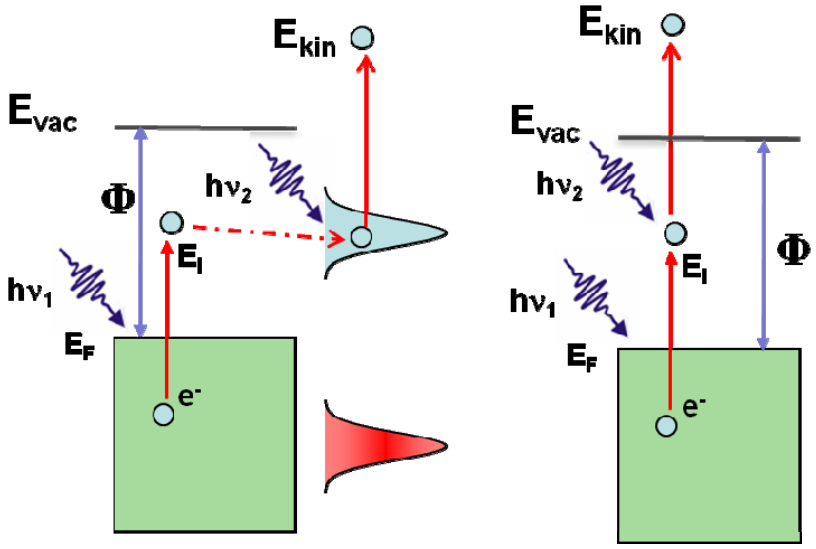

Figure 1.1: Schematic illustration of two-photon photoemission process.

energy of the electron provides the energetic positions of the electronic states involved in the photoemission process. By varying photon energy, the occupied and unoccupied electronic states can be distinguished based on the dependence of the kinetic energy of photoelectrons on photon energy. The dispersion and dynamic experiments measure the extent of delocalization and the decay rate of the electronic state at a particular energy, respectively.

The energetic and dynamical information from 2PPE are valuable for understanding the charge transport at molecule–metal interface and helpful for improving the performance of molecular electronics. For example, the alignment of molecular orbital energies (e.g., HOMO, LUMO) relative to the metal Fermi level determines the energy barrier for electron/hole injection at the interface. Moreover, 2PPE photoemission yield indicates the strength of electronic coupling between a metal surface and a molecule which determines not only the charge transfer barrier but also the dynamics of interfacial charge transfer.[9,10]

The electronic configuration at the molecule–metal interface is sensitive to the molecular adsorption structures which affect the molecular orbital overlap with the metal surface. The adsorption geometry is determined by the balance between adsorbate-metal interactions and intermolecular forces between closely-spaced adsorbate molecules. For example, alkanethiol molecules adsorbed on metals undergo a compressional phase transition with increasing coverage. At low coverage, the adsorbed molecules are "lying-down", with their alkyl chains more nearly parallel to the surface plane; when the coverage is increased, the molecules change to a "standing-up" configuration, with the alkyl chains aligned closer to the surface normal.[11-14] The interfacial electronic states corresponding to the different phase structures show differences in the extent of delocalization.[15] In Chapter 3 of this dissertation, the electronic structure of thiophene adsorbed on Au(111) at different coverages is investigated by 2PPE, temperature

programmed desorption (TPD) and density functional theory (DFT) calculations. The adsorption geometry of thiophene changes with its coverage, which causes different electronic properties. The motivation to choose thiophene as a model system comes from the increasing interest in electronic devices based on polythiophene and its derivatives.[16,17] In addition, the interaction between thiophene molecules and Au surface is different from that of alkanethiols on Au, since thiophene is an aromatic molecule and one lone electron pair of S atom is involved in the π-electrons structure. When adsorbed on Au surface, thiophene molecule binds to the metal surface not only through the S atom, but also by π-electrons of the ring.

Besides the S–metal linkage of the alkane thiols, diisocyanide molecules also have attracted widespread interest for molecular electronics applications as the N≡C triple bond is expected to effectively connect pπ orbitals of aromatic moiety with dπ orbitals of the metal contact. Indeed, the molecules containing isocyanide terminal group have been demonstrated to have higher conductance in Au-CN junctions compared to Au-S interface.[18,19] However, some groups have reported the opposite trend.[20] In Chapter 4 and Chapter 5, we present the studies on the interfacial electronic structure and adsorption structures of diisocyanide molecules on Au(111) surface using 2PPE, scanning tunneling spectroscopy (STS), scanning tunneling microscopy (STM) and DFT calculations. Compared to other molecule–metal interface sensitive techniques such as X-ray adsorption fine structure and X-ray photoelectron diffraction[21] which provide ensemble averages, STM has the capability to obtain the molecular configuration at the atomic scale.[22] By recording the tunneling current versus tip-sample bias, STS experiments provide information on the density of both occupied and unoccupied states with a spatial resolution on the atomic scale as well. Combining STM and STS together, the relationship between adsorption structure and electronic properties can be established for a single adsorbed

molecule. Combined with the macroscopic information collected in 2PPE experiments, a clearer picture has been obtained for the electronic structures of diisocyanid/Au(111) interfaces which is key to understanding the charge transport in diisocyanide-Au contacts.

At the interface, the charge redistribution due to adsorption is important for the catalytic activity of supported heterogeneous catalysts. The resulting interfacial dipole rectifies interfacial electron transfer, concomitantly electronic properties of supported components which are crucial for the adsorption and reaction of adsorbates.[23,24] For instance, Au_8 clusters binding to oxygen vacancy defects on a MgO film are partially negative charged because of electron transfer from the defects. These negatively charged Au_8 clusters can catalyze the low-temperature oxidation of CO. By comparison, the Au_8 clusters deposited on close-to-perfect (oxidized) magnesia surface are chemically inert for the CO oxidation reaction.[23] This kind of interfacial charge redistribution can be probed by surface work function measurements. The Chapter 6 of this dissertation presents the local work function investigation on size-selected molybdenum sulfide deposited on an ultrathin alumina film. Molybdenum sulfide is commonly uses as a hydrotreating catalysts to produce clean petroleum products in order to meet the strict environmental regulations.[25] It is well known that as the size of a material is reduced to nanometer regime, its structural and electronic properties are significantly different from those of the bulk material.[26,27] Small molybdenum sulfide nanoclusters also exhibit size-dependent atomic and electronic structures, and such effects are expected to influence catalytic activities.[28-30] In order to study the properties of molybdenum sulfide clusters with different sizes, a size-selected cluster deposition apparatus was used where the desired cluster with a specific mass is selected in a quadrupole mass filter. As a result, the size and composition of the cluster are precisely controlled. In this work, size-selected molybdenum sulfide clusters, Mo_xS_y (x/y = 2/6, 4/6, 6/8, 7/10), were deposited onto an

ultrathin aluminum oxide film formed on a NiAl(110) surface which serves as a model system for industrial Al_2O_3 supported catalysts. With bulk Al_2O_3 as a support, there is always charging problem during photoemission experiments because it is an insulator. Using ultrathin Al_2O_3 film as a substrate, the charging problem can be avoided. It allows surface science techniques to be used to elucidate the electronic and catalytic properties of the model catalyst.

Chapter 2. Experimental Section

In this chapter, I will discuss the major optical and vacuum instrumentation used to obtain the data presented in this thesis. Section 2.1 will describe the ultrafast laser system for 2PPE experiments. Section 2.2 and 2.3 will provide a description of the UHV chamber where I conducted most of my experiments. Section 2.2 will give a brief introduction to the size-selected cluster deposition apparatus and section 2.3 will focus on the surface analysis chamber which is the end station for cluster deposition as well.

2.1 Two-photon photoemission laser system

2.1.1 Ti:Sapphire Oscillator

In our experiments, the laser source, a Ti:Sapphire oscillator (Spectra-Physics Tsunami), is pumped by a 5 W continuous-wave solid-state Nd:YVO_4 laser at 532 nm (Spectra-Physics Millennia V). It generates pulses with duration around 100 fs, tunable between 720 and 850 nm. When operating at 800 nm, the average power of the Ti:Sapphire laser is 900 mW with a repetition rate of 80 MHz.

The output laser pulse is monitored by a fiber optic spectrometer (Ocean Optics, Inc. HR2000) to measure the spectral bandwidth. The pulse duration is determined by an autocorrelator. This approach converts optical path lengths to temporal differences to measure the ultrafast pulse. The configuration is based on Michelson interferometer as shown in Figure 2.1. The input laser beam is split into two pulses of equal intensity by a beamsplitter. In each beam path there is a retroreflector. One is mounted on a translation stage to adjust path length. The other one is attached to an audio speaker (VIFA, 6.5 inch in woofer, poly cone) in the rapid scanning path. In our experiments, the audio speaker is driven by a sine wave generator operated

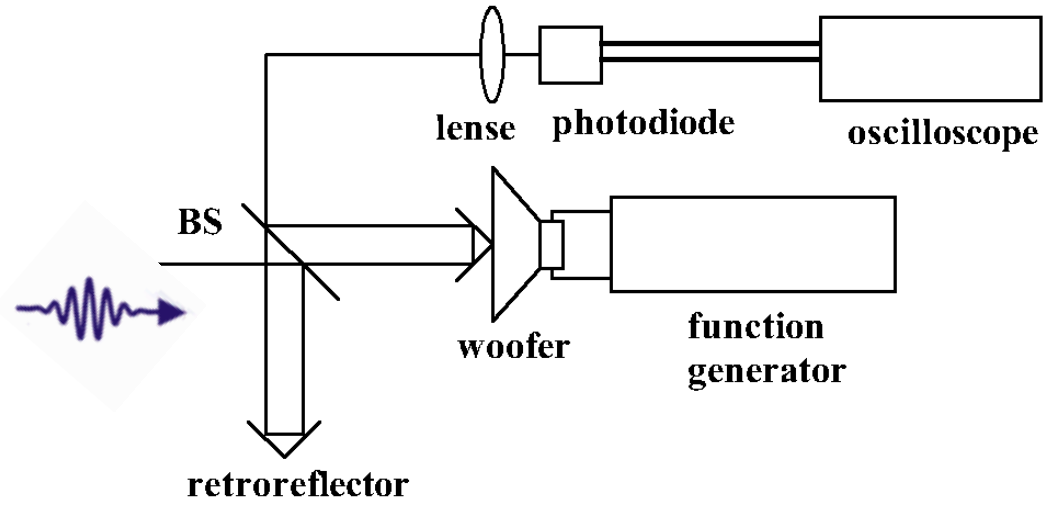

Figure 2.1: Schematic of an autocorrelator for characterizing the laser pulse from Ti:Sapphire oscillator.

at a frequency of 30 Hz. The two beams are recombined using a beamsplitter and focused by a BK7 plano-convex lens with a focal length of 1 inch. A switchable-gain, amplified GaAsP detector (Thorlab, PDA500) is set at the focal point to observe the autocorrelation signals directly from the two-photon-induced photocurrent. Figure 2.2 shows an example of the autocorrelation pattern of a laser pulse with a center wavelength of 800 nm shown on the oscilloscope display. The advantage of using GaAsP photodiode is that the desired two-photon response and the transformation of light into electric current are combined into a single solid-state device.[31] The experimental results demonstrate that the measured pulse duration, τ_p, follows the relationship with spectral bandwidth, $\Delta\nu$, for the transform-limited pulse with Gaussian shape from Tsunami.

$$\tau_p \times \Delta\nu = 0.441 \qquad (2.1)$$

Based on this time-bandwidth product, the pulse duration can be calculated using the spectral bandwidth for daily experiments.

2.1.2 Nonlinear optical harmonic generation system

For Ti:Sapphire operated at 800 nm, the photon energy is ~1.55 eV which is not enough for exciting electrons out of a typical metal surface. For example, the work function of Au(111) is 5.55 eV.[15] In order to explore electronic states over a large energy range in a metal or a semiconductor, we use a nonlinear optical crystal to generate frequency doubled and tripled light which have photon energies of 3.10 and 4.65 eV, respectively. In this section, we describe the second and third harmonic generation process in our optical system.

Non-linear conversion of the Ti:Sapphire laser output to UV wavelngths is accomplished by a time-plate harmonic generator (Photop TP-2000B). The first step is to generate a second

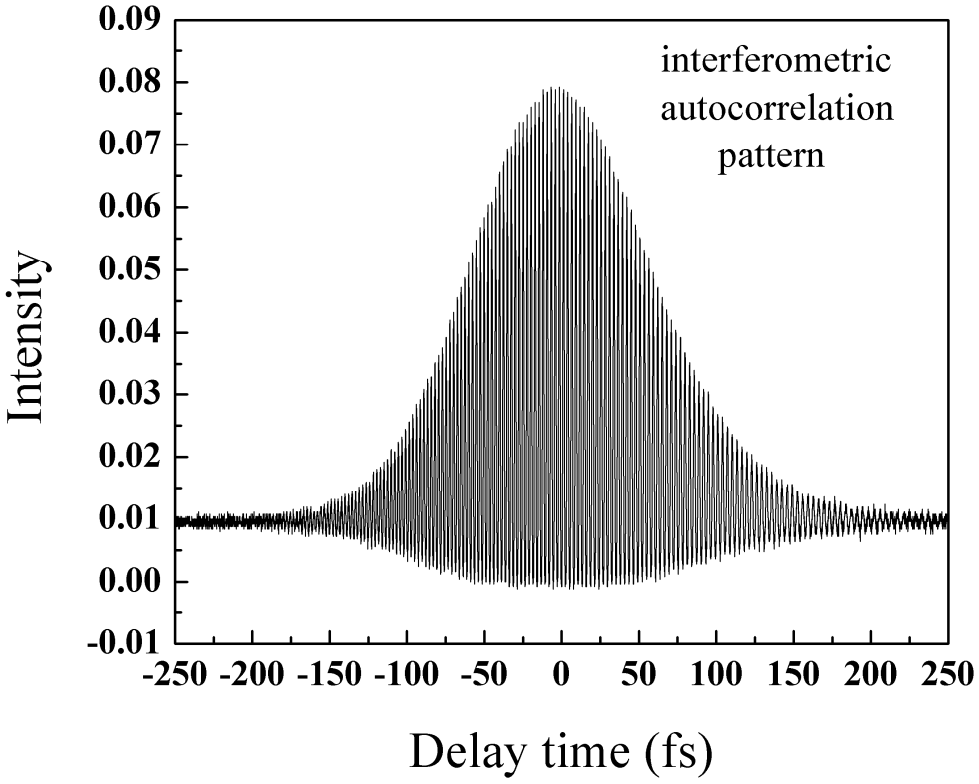

Figure 2.2: The autocorrelation pattern of a laser pulse with a center wavelength of 800 nm shown on the oscilloscope display.

harmonic wave. A BBO crystal is used for this purpose and the conversion efficiency is described by[32]

$$\frac{P_{2\omega}}{P_{\omega}} = 8\left(\frac{\mu_0}{\varepsilon_0}\right)^{\frac{3}{2}} \frac{\omega^2 \left(d_{ijk}\right)^2 L^2}{n^3} \left(\frac{P_{\omega}}{Area}\right) \frac{\sin^2\left(\Delta k \cdot L/2\right)}{\left(\Delta k \cdot L/2\right)^2} \tag{2.2}$$

where L is the effective conversion length in the BBO crystal, d_{ijk} is the appropriate nonlinear susceptibility tensor element for the incoming fundamental and outgoing second harmonic waves of specific polarization, and Δk is the wave vector difference between the fundamental and second harmonic waves. In order to achieve the highest conversion efficiency, the BBO crystal needs to be operated under a phase matching condition, $\Delta k = 0$. Otherwise, the generated second harmonic wave will not combine constructively. In the BBO crystal, fundamental light (red light) and the generated second harmonic (blue light) are polarized perpendicular to each other. As shown in Figure 2.2, only at a specific angle, θ_0, the extraordinary beam of blue light has the same index of refraction with the ordinary beam of red light, $n_{o\omega} = n_{e2\omega}$, and the phase matching condition is achieved. In our experiments, the BBO crystal is mounted on a stage which can be translated and rotated. We adjust the angle of the crystal and the distance between focus lens and BBO crystal to maximize the power of the second harmonic wave.

A type 1 BBO crystal is used in the THG process. There are two main issues that need to be addressed for reaching high conversion efficiency. One is that the polarization of the fundamental and second harmonic should be in the same direction for a type 1 BBO crystal. However, these beams are polarized perpendicular to each other after the SHG process. To solve this problem, a half-wave plate is set in the beam path to rotate the polarization of the fundamental beam (red light) and the second harmonic wave is unaffected. The other problem is related with the temporal overlap of fundamental and second harmonic waves. Because the group

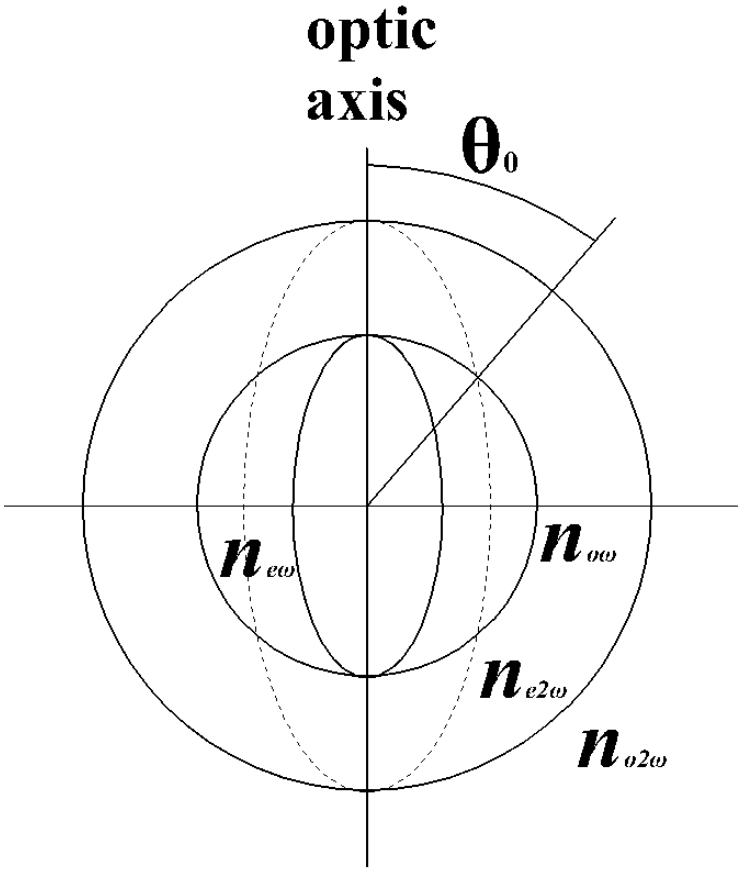

Figure 2.2: The phase matching condition for a nonlinear optical crystal

velocity difference between fundamental wave and second harmonic wave in the half-wave plate introduces a time delay between these two waves, the conversion efficiency will be limited especially for a femtosecond pulse. One solution is utilizing different optical path lengths of fundamental and second harmonic waves to compensate the time delay. Specifically, two beams are split into two different beam paths where one can be adjusted precisely using a translation stage and recombined before the BBO crystal for THG. In our experiments, a group velocity compensation plate is applied instead of setting up two different beam paths. This compensation plate is a negative uniaxial BBO crystal which has a lower refractive index for the extraordinary wave. In our case, the optical axis of the plate is perpendicular to the polarization of the fundamental wave so that the second harmonic wave becomes the extraordinary wave and experiences a lower index of refraction than the fundamental. By tuning the compensation plate to a particular angle, the time delay can be adjusted. This plate must be installed in front of the half-wave plate since it only works for beams with different polarizations. As a result of the type 1 BBO crystal, the polarization of the third harmonic wave is perpendicular to those of the fundamental and second harmonic waves.

2.1.3 Two-Photon photoemission experiments

Figure 2.3 shows a schematic optical setup for the 2PPE experiment. The laser pulses chosen for the experiments are incident at 47.5° with respect to the surface normal and the polarization of the laser can be controlled by a half-wave plate in each beam path. The beam is focused at the sample surface by an achromatic lens with a 38 cm focal length (Special Optics). The size of the focused beam on the surface is less than 250 μm. After the focus lens, a flipper

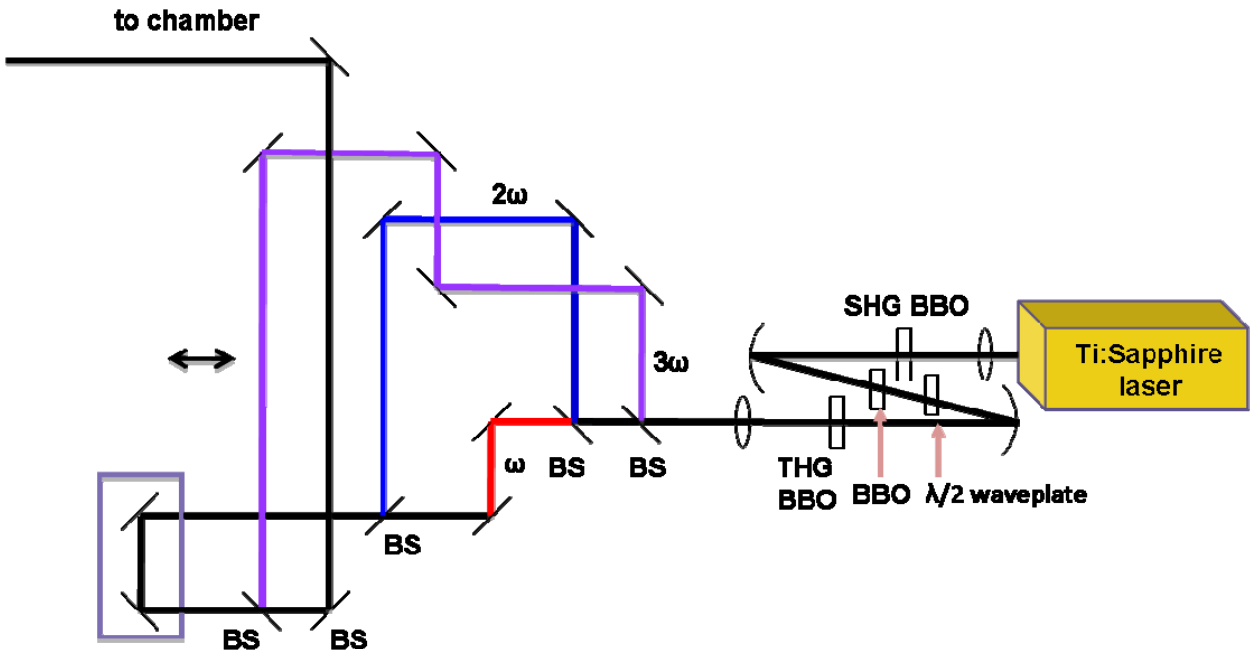

Figure 2.3: Schematic of the optical setup for 2PPE experiment

mirror is used to reflect the beam passing through an iris in order to check the spatial overlap of different laser pulses.

Photoelectrons are detected with a hemispherical electron energy analyzer (Specs Phoibios 100) with an instrumental resolution of 40 meV under our detection conditions. A bias voltage is applied to the sample to improve the collection efficiency for low energy electrons. This allows for a more accurate determination of the low energy secondary electron cutoff from which the surface work function is calculated. The work function, Φ, is determined from 2PPE spectra by the expression

$$\Phi = 2h\nu - E_F + E_{cs} \tag{2.3}$$

where $h\nu$ is the photon energy and E_F and E_{cs} are the observed energies for the cutoff of photoemission from near the Fermi level and the half maximum of the secondary electrons edge at the photoemission threshold, respectively. Figure 2.4 displays a 2PPE spectrum of NiAl(110) as an illustration. The 2PPE spectra are measured with the sample perpendicular to the electron energy analyzer axis except for those acquired in the angle-resolved experiments. Angle-resolved measurements are performed by rotating the crystal relative to the analyzer to investigate the dispersion of the 2PPE photoemission bands. The latter is characterized by an effective electron mass (m*) assuming a simple parabolic band model,[33] i.e.,

$$E_{kin} = E_0 + \hbar^2 k_{\parallel}^2 / 2m^* \tag{2.4}$$

where E_{kin} is the kinetic energy of the electron photoemission. The parallel momentum vector $k_{\parallel}$ is calculated from

$$k_{\parallel} = (2m_e E_{kin})^{1/2} \sin\theta / \hbar \tag{2.5}$$

where θ is the angle of electron detection with respect to the surface normal and m_e is the electron mass which is a quantitative measure of the extent of localization/delocalization.

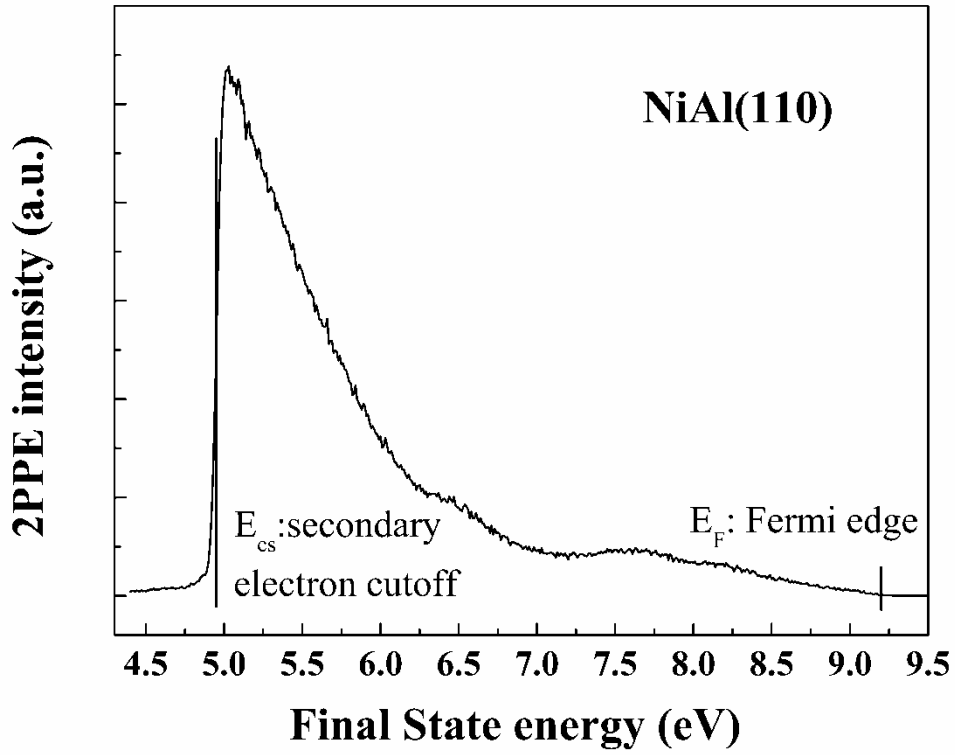

Figure 2.4: Monochromatic 2PPE spectra of NiAl(110). The photon energy is 4.60 eV.

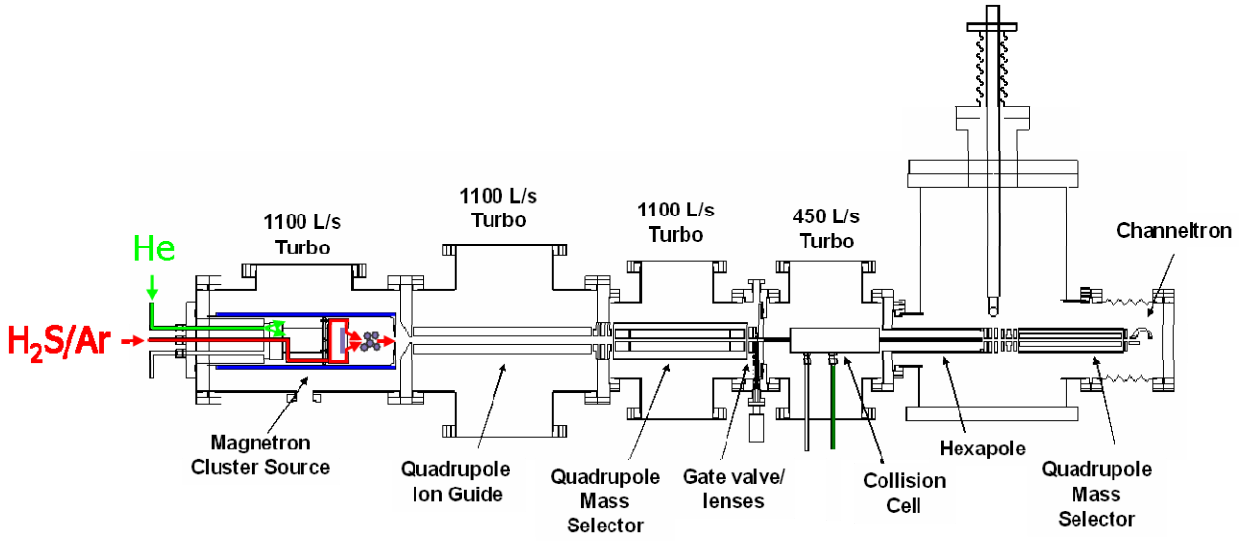

Figure 2.5: Schematic of the cluster deposition apparatus.

2.2 Size-selected cluster deposition apparatus

The size-selected cluster deposition apparatus, which includes five main parts, is shown schematically in Figure 2.5. They are a magnetron sputtering source, quadrupole ion guide, quadrupole mass selector, hexapole ion guide (includes a collision cell for gas phase studies) and quadrupole bender. The first four parts are equipped with turbomolecular pumps for differential pumping to isolate the high-pressure magnetron ion source (a few Torr) from the UHV environment in analysis chamber (1×10^{-9} Torr).

In this work, the clusters are produced in a magnetron sputtering source (Oxford Applied Research NC200U) whose design is based on the concept originally developed by Haberland.[34,35] The magnetron target is located above a rare earth magnet and both of them are water cooled. The discharge gas (Ar in this case) is introduced into the magnetron source from the cover. When a high bias voltage is applied through the water cooling line and the cover is kept at ground, a flow discharge is formed above the target. The magnets confine the plasma above the target and the applied bias voltage accelerates the Ar^+ ions towards the target. In order to make molybdenum sulfide, a gas mixture containing 4% H_2S in Ar is used as a sputter gas. The sputtered atoms and small clusters are ejected into a high pressure region where they collide with an aggregation gas (He in this case), other sputtered atoms and clusters. During this process, small clusters aggregate into large clusters and high kinetic energy is dissipated. The composition and size distribution of clusters can be controlled by several parameters, which include sputtering gas pressure, discharge voltage on metal target, aggregation gas pressure and volume of aggregation area. Usually, the pressures of H_2S/Ar and He are 12 Torr and 30 Torr, respectively. The discharge voltage on the target is 180~200 V. A typical mass spectrum of Mo_xS_y cluster ions is shown in Figure 2.6a.

Two quadrupole systems are used for the ion guide and mass selector. A detailed description of the quadrupole mass filter and rigorous theoretical treatment can be found in Peter Dawson's classic book "Quadrupole mass spectrometry and its applications".[36] Here I will only give a brief introduction of how a quadrupole works and describe our experimental conditions. A quadrupole consists of two pairs of metal rods oriented with their centers coinciding with the corners of an imaginary square. They are mutually parallel and electrically isolated to make the electric field between them hyperbolic. In our experiments, opposite pairs of quadrupole rods are electrically connected and a combination of DC and RF voltage is applied to rods. A DC pole bias determines the centerline potential of the quadrupole and the RF potentials are 180 degree out of phase with equal magnitude. The quadrupole ion guide is running in RF-only mode without DC voltage applied to the rods such that it acts as a high pass filter for transport of clusters from the ion source to the mass selected region. The quadrupole mass selector has rods with diameters of 19 mm and a commercial RF and DC power supply from Extrel (150-QC; 40 KHz). This provides good ion transmission and a unit mass resolution range up to 4000 amu for our experiments. By varying the RF amplitude and DC voltage, we can scan a mass spectrum of all cluster species or select a single mass, which allows only the specific cluster with stable trajectories to go through the quadrupole for deposition.

The mass-selected clusters are extracted to the UHV analysis chamber by a hexapole ion guide which is used as a collision cell to investigate gas phase reactions as well. In gas phase experiments, reactive gas is introduced into the collision cell to react with clusters and products can be focused into another quadrupole mass spectrometer for analysis. In cluster deposition experiments presented in this dissertation, selected clusters go through the hexapole ion guide and are deflected by a quadrupole bender to separate them from neutral species before they are

deposited onto a surface. In a magnetron cluster source, not only ions but also a significant amount of neutral clusters are produced. Some of neutral species will extend to the final UHV chamber although a large amount of them are pumped away in each chamber section. For cluster deposition experiments, it is important to know the composition and amount of clusters that land on the surface, which makes it necessary to separate cluster ions from neutral species. In our experiments, this goal is achieved by a quadrupole deflector. An electronic field deflects the ion species by 90 degree onto the surface, while neutral ones are unaffected and pass straight through the bender.

A Faraday cup, about a few millimeters away from the final lens of the quadrupole bender, is used to detect the cluster intensity. The magnetron source, RF-amplitudes of ion guide, DC pole bias voltage, electrostatic lenses and bender electrode voltages are set to maximize the ion intensity of the cluster to be deposited. Typical ion current for molybdenum sulfide clusters is 1~3 nA dependent on cluster composition and source conditions. The kinetic energy distribution of a cluster is determined by applying a DC voltage ramp on the Faraday cup while monitoring the cluster ion current. Figure 2.6b displays the kinetic energy distribution of the Mo_6S_8 cluster fitted with a Gaussian function. The center is located at 1.38 eV and the FWHM is 2.64 eV. This gives a per-atom energy of ~0.1 eV which is low enough to achieve "soft landing" conditions.[37-39] Specifically, the collision induced deformation is elastic and the clusters that land on the surface keep their identity. After maximizing the cluster ion intensity and determining the distribution of kinetic energies, the Faraday cup is translated away and the crystal is positioned for deposition. The ion current on the crystal is measured with a picoammeter (Keithly). A LabVIEW program is used to set the selected mass and monitor the cluster coverage based on the ion current on crystal. The coverage is calculated using the estimated cluster radius (3 Å) and the

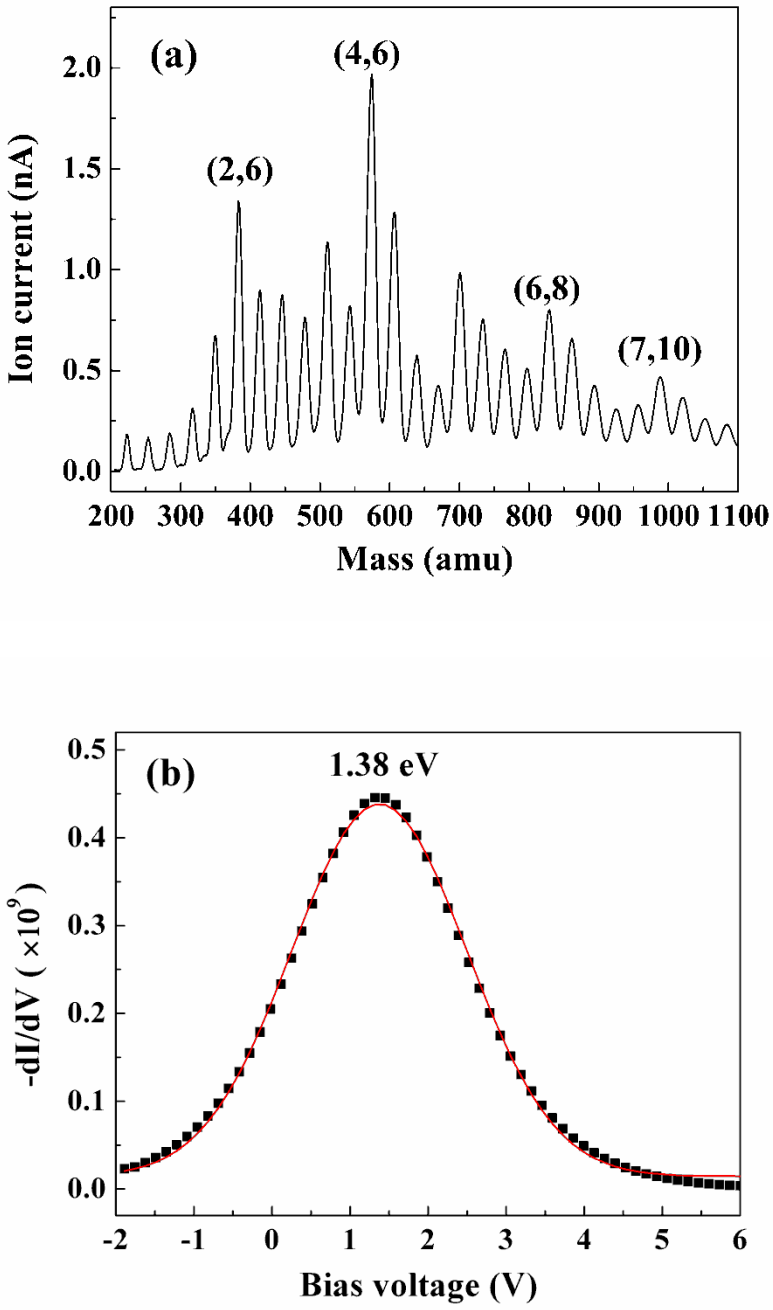

Figure 2.6: (a) mass spectra of Mo_xS_y cluster formed in magnetron sputtering source. (b) The negative first-derivative of the Mo_6S_8 cluster ion current over bias voltage (black squares). The red curve is a Gaussian fitting for experimental data.

deposition area (~10–17 mm^2). The cluster radius was determined by Density Functional Theory (DFT) calculations on gas-phase Mo_xS_y clusters.[40,41] The details of calculating the deposition area will be given in section 6.2.

2.3 UHV surface analysis chamber

Figure 2.7 shows a schematic of upper level and lower level of the UHV analysis chamber. This chamber has a base pressure lower than 1×10^{-9} Torr and is equipped with surface instrumentation for cleaning the crystal surface, performing thermal desorption and photoemission measurements. This section will describe the single crystals and main surface characterization techniques used in this work.

2.3.1 Single crystal substrate

My experiments involve Au(111) and NiAl(110) crystals. They are mounted by a 0.5 mm (diameter) Ta wire wrapped around a groove machined in the edge of the crystal. The two ends of the wire are spot welded to two W wires and connected to an inverted instrumentation feedthrough attached to the bottom of a stainless steel hollow tube that acts as a reservoir for liquid nitrogen (LN_2). The top of the tube is mounted on an XYZ manipulator and rotation stage allowing precise positioning of the sample. Temperature control of the crystal (85–1000 K) is accomplished by LN_2 cooling and resistive heating. Prior to each experiment, the surface of the crystals are cleaned by sputtering with Ar^+ ions (for Au(111), two cycles at 1 kV and one cycle at 0.5 kV; for NiAl(110), two cycles at 2 kV), and annealing between each sputtering cycle (Au(111) and NiAl(110) crystals are annealed at 800 K and 1300 K respectively). No impurities are detected by XPS and AES after the cleaning procedure.

a)

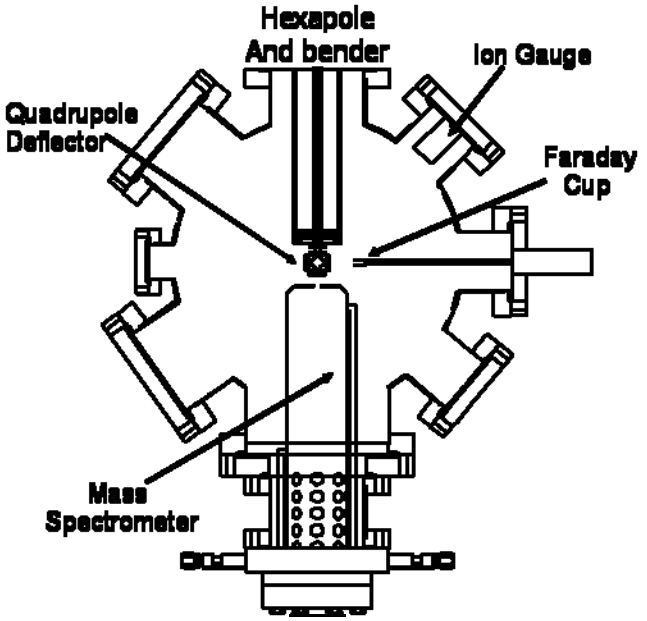

b)

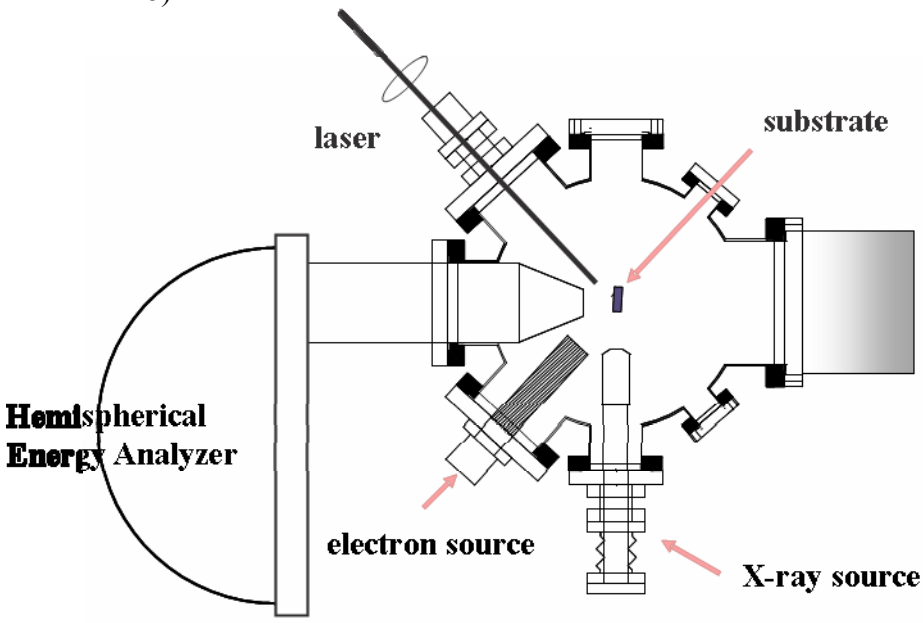

Figure 2.7: Schematic of the UHV analysis chamber, a) lower level and b) upper level.

2.3.2 Temperature Programmed Desorption experiments

On a surface, any adsorbed species must be bound to the surface with some energy and will desorb at a rate determined by the Boltzmann factor. Heating the surface will increase this desorption rate. Temperature Programmed Desorption (TPD) is a method to study the temperature dependence of the desorption rate and leads to information on the binding energy of the adsorbates on the surface. If binding energy, E_{ad}, is independent of surface coverage, for first-order desorption process, the Redhead model is often used to estimate E_{ad}:[42]

$$E_{ad}/RT_p^2 = (\nu/\beta)\exp(-E_{ad}/RT_p) \qquad (2.6)$$

where T_p is the temperature at which the desorption rate is a maximum, v is the pre-factor and β is the heating rate. This equation shows that T_p is independent of coverage and thus the activation energy, E_{ad}, can be estimated from T_p:

$$E_{ad}/RT_p = \ln((\nu/\beta)*T_p)-3.64 \qquad (2.7)$$

The pre-factor is normally taken as 10^{13} sec^{-1} and this equation can provide a reliable value for adsorption energy for $10^{13} > v/\beta > 10^8$ K^{-1}.

In our experiment, the UHV chamber is backfilled with the desired gas to some pressure via a leak valve. The applied dose is monitored in term of Langmuir (L), where 1 L = 10^{-6} Torr·sec. After exposure for a measured length of time, the sample is brought to the lower level of the chamber (shown in Figure 2.7a) and rotated to face a quadrupole mass spectrometer (Hiden). The sample is resistively heated at a rate (normally 2 K/s) which is controlled by a process control unit (Eurotherm) and desorbed molecules are detected by the mass spectrometer. The mass spectrometer is shrouded by a LN_2 reservoir to reduce background gas signal. Typically, the ion emission current is 0.1 mA and multiplier voltage is 2100 V.

2.3.3 X-ray Photoelectron Spectroscopy and Auger Electron Spectroscopy

X-ray Photoelectron Spectroscopy (XPS) and Auger Electron Spectroscopy (AES) are surface sensitive analysis techniques due to the relatively short mean free path of excited photoelectrons.[43] In XPS, a monochromatic x-ray beam with photon energy of *hv* excites a core electron from the surface to vacuum if the photon energy is greater than the binding energy of the electron. The kinetic energy of the emitted electron equals to the difference between the photon energy and the binding energy. Since the binding energy of a core electron is elemental specific, XPS can provide information about the composition of the sample surface. More important information that we can gain from XPS is the chemical shift of the binding energy for elements. This shift has its origin in either initial-state or final-state effects.[44] The initial-state effect involves the charge of atom prior to photoemission and the final-state effect occurs following photoelectron emission, such as the polarization of surrounding ions and core hole screening. In our experiments, we usually ascribe binding energy shifts to intial state effects, e.g., changes in charge localized at an atomic site due to chemical or structural changes.

In our XPS experiments, an x-ray source (XR-50, Specs) is used to provide monochromatic x-rays from either Mg (Kα line: 1253.6 eV) or Al (Kα line: 1486.6 eV). With two different anodes, it is easy to distinct Auger or photoemission process. The excited electrons are detected with the same hemispherical electron energy analyzer as in 2PPE experiments. The crystal is grounded to prevent charging and placed at 45° with respect to the x-ray source and the analyzer. The distance between the crystal and the x-ray anode face is about 14 mm. The XPS data is fitted using either CasaXPS or XPSPEAK software. Both programs give similar results. Briefly, the data is first subjected to a Shirley background correction to account for the inelastic scattered electron background. Then it is fitted using Gaussian-Lorentzian peak shapes with

some constraints on fitting parameters based on the physical nature of the sample investigated. After the fitting procedure, information about the peak positions, FWHM, area, etc. can be extracted.

In the Auger process, an electron beam with sufficient energy excites an electron from a core level. The resulting hole is filled by an electron from a higher state. During this process, the loss of energy for the electron transferring from higher state to the hole at lower state results in fluorescence or the ejection of an Auger electron from higher energy state. The kinetic energy of the Auger electron is independent of the photon energy and determined by the energy difference between the electronic states involved, which are elemental specific. As a result, an Auger spectrum provides a fingerprint of the chemical composition of the surface. Not only qualitative analysis but also quantitative analysis from AES is applied in our experiments. We use the peak-to-peak intensity height in the differential mode to estimate the relative amount of size-selected clusters deposited on the surface. This peak-to-peak height is approximately proportional to peak area. Experimentally, the electron beam is provided by an electron gun (EQ 22/35, Specs) operating at 5 kV. It is located 45° with respect to the hemispherical analyzer. The sample is positioned normal to the analyzer entrance and is held at ground potential to avoid charging.

Chapter 3. Electronic structure of the thiophene/Au(111) interface probed by two-photon photoemission

This section was published in *J. Phys. Chem. C*, 114, 13670−13677, 2010

3.1. Introduction

Knowledge of the electronic structure at the interface between a molecule and a metal electrode is important for understanding the performance of molecular devices with potential applications in chemical and biological sensors,[45] photonics[46] and solar photoconversion.[3] For instance, the energetic alignment of the molecular states (e.g., HOMO, LUMO) with respect to the Fermi level determines the charge injection barrier which is critical in molecular electronics.[47,48] The interfacial electronic structure is also sensitive to structural transformations which alter the geometry of the adsorbed molecule and hence the orbital overlap with the metal surface. Changes in geometry are driven by the balance between adsorbate-metal interactions and intermolecular forces between closely-spaced adsorbate molecules. Examples include the well-studied alkanethiols on Au(111), Ag(111) and Cu(111) single crystal surfaces which undergo a compressional phase transition with increasing coverage from a phase in which the molecules are "lying-down", with their axes more nearly parallel to the surface plane, to one in which the molecules are "standing-up", with their axes oriented closer to the surface normal.[11-15] Such phase changes alter the interfacial electronic structure through changes in orbital hydridization at the thiol–metal contact and the loss of direct chain–surface interactions.

One of the more effective experimental probes of interfacial electronic structure is two-photon photoemission (2PPE) which can provide spectroscopic and dynamic information on both the occupied and unoccupied resonant states of the metal substrate and adsorbate.[47] In the case of

methanethiol adsorbed on Ag(111), 2PPE experiments showed that an adsorbate-induced unoccupied state was localized (non-dispersive) at low coverage where the S–C bond is parallel to the surface. At higher coverage, where molecules lying parallel and perpendicular to the surface co-exist, both localized and delocalized (dispersive) unoccupied states were observed.[12] Coverage dependence was also observed in 2PPE for the 1-hexanethiol/Au(111) interface, where the binding energy and the effective electron mass of an unoccupied state changed as the molecules tilted away from the surface at higher coverage.[15]

Similar coverage-dependent structural transformations have also been observed for aromatic molecules such as pyridine (C_5H_5N) and thiophene (C_4H_4S) where binding to the metal surface involves interactions with the heteroatom (e.g., N or S) and π-electrons of the ring.[49-52] Unlike the R–S–metal thiolate linkage which has configurational flexibility about the single bonds, the rigid aromatic ring structure means that changes in the ring orientation relative to the metal surface will in turn strongly modify the heteroatom-metal bonding interactions. In the case of pyridine adsorbed on Cu(111), two $n = 1$ image states were observed by 2PPE and assigned to two different phases of the pyridine adlayer, i.e., lying-down and standing-up, associated with different coverages and exhibiting different local work functions.[49] In the case of thiophene on Au(111), as well as on Ag(111) and Cu(111), XPS,[50] NEXAFS,[51] IRRAS[53,54] and STM[55,56] studies have shown that the angle bewteen the molecular plane and the surface increases with increasing coverage. Qualitatively, this coverage dependence suggests the importance of π-π intermolecular interactions at high coverage, however, the effects of binding configuration on the interfacial electronic structure have not been reported. In particular, it is not known if the thiophene–Au bond involves localized orbitals on the S-atom or extends over the ring structure and whether this changes as a function of the thiophene-surface angle.

In this work, we investigated the interfacial electronic structure of thiophene adlayers on Au(111) using 2PPE spectroscopy and density functional theory (DFT) calculations. Our choice of thiophene as a model system is motivated by interest in electronic devices based on polythiophene and its derivatives, e.g., photovoltaics, photodiodes and field effect transistors, in which charge transfer at the polythiophene-metal contacts plays an important role.[16,57-59] For the thiophene/Au(111) surface, we observe an unoccupied state which grows in intensity as the density of thiophene overlayer increases. DFT calculations performed as a function of thiophene coverage suggest that the observed unoccupied level is a LUMO-derived state of mixed sulfur and carbon p-π character. The calculations also show that with increasing coverage the molecules tilt away from the surface plane and the thiophene binding energy decreases. The change in tilt angle at higher coverage is accompanied by a narrowing of the thiophene-derived unoccupied bands and energy shifts away from the Fermi level. The former is consistent with our 2PPE results, while the latter is contrary to the small increase in the 2PPE final state energy of the S_u state with increasing coverage. We attribute the coverage-dependent S_u energy shift to a balance between changes in the thiophene-Au interaction, and changes in the charge-induced interaction of the transient S_u anion state with the Au(111) surface and surrounding thiophene molecules.

3.2. Experimental and Theoretical Methods

The UHV chamber and the main experimental methods used to conduct the experiments in this chapter are described in details in chapter 2. Briefly, Au(111) crystal can be resistively heated to 1000 K and cooled down to 90 K with LN_2. The crystal was cleaned by sputtering with Ar^+ ions and annealing at 800 K between each sputtering cycle. The cleanliness was verified by XPS, AES and 2PPE experiments. The thiophene (99%, Aldrich) was purified by several freeze-

pump-thaw cycles prior to dosing. The dosing was performed by back-filling the chamber through a leak valve, and all reported exposures are in Langmuir units (1L = 10^{-6} Torr·sec) based on the ion gauge reading. For TPD experiments, desorbing thiophene was detected with a quadrupole mass spectrometer (Hiden) at the parent ion mass (84 amu).

In 2PPE experiments, approximately 70 mW of the third (~267 nm) harmonic beam was used. The laser pulses were incident at 47.5° with respect to the surface normal. The beam was focused at the crystal surface by an achromatic lens. Photoelectrons were detected with a hemispherical electron energy analyzer (Specs Phoibios 100) with an instrumental resolution of 40 meV under our detection conditions. A bias voltage of -4.3 V was applied to the sample to improve the collection efficiency for low energy electrons. All 2PPE experiments were carried out with a crystal temperature of 100 K.

DFT was used to investigate the chemical interaction of thiophene with Au(111). The calculations were performed using the code DMol^3.[60,61] The generalized gradient approximation proposed by Perdew and Wang[62] was employed for the exchange and correlation functional. All electrons were treated explicitly and relativistic effects were introduced into the core. The wave functions were expanded in terms of a double-numerical quality basis set with polarization functions. A global orbital cutoff of 5.5 Å was used. The substrates were modeled by a three-layer slab separated by a 20 Å-thick vacuum layer, with the bottom two layers of atoms fixed in their optimized bulk positions while the top layer was allowed to relax together with the adsorbed thiophene molecule. Brillouin-zone integrations were performed on a grid of 3×3×1 Monkhorst-Pack special k-points[63] to calculate the energetics and geometry of thiophene on Au(111) for the (4×4) and (3×3) unit cells, corresponding to coverages of 0.0625 and 0.11 ML, respectively (1 ML is defined as one adsorbed thiophene molecule per surface gold atom). A grid

of 5×5×1 Monkhorst-Pack special k-points and a (2×2) unit cell were employed at the coverage of 0.25 ML. The adsorption energy of thiophene on Au(111) was calculated by:

$$E_{ad} = E[thiophene/Au(111)] - E[Au(111)] - E(thiophene) , \quad (3.1)$$

where *E[thiophene/Au(111)]*, *E[Au(111)]* and *E(thiophene)* are the total energies of the thiophene adsorbed on Au(111), the clean Au(111) and the gas phase thiophene molecule, respectively.

3.3. Results and Discussion

3.3.1 Thermal desorption

Figure 3.1 displays a series of TPD spectra of thiophene adsorbed on Au(111) as a function of exposure. The overall features of the TPD spectra are similar to those observed in previous work for the same system.[50,64] For very low exposure (0.014 L), we resolve two desorption features. The higher-temperature feature near ~293 K is very weak and rapidly-saturated, and we attribute it to thiophene adsorbed at surface defect sites. The lower-temperature feature at ~260 K increases continuously in intensity and shifts to lower temperature (186 K) with increasing exposure (up to 2.4 L). We assign this feature to thiophene molecules bound at terrace sites on the Au surface. The shift to lower temperature implies a repulsive interaction between the adsorbed thiophene molecules. Further increases in thiophene exposure result in the development of a peak at 173 K whose intensity saturates at ~4.0 L, and the growth of a sharp peak at 139 K which does not saturate at the highest exposures we have investigated (6.0 L). Analyzing the leading edge (121–132 K) of the 139 K TPD peak, we calculate an activation energy for desorption of 0.32 ± 0.02 eV which is consistent with the heat of vaporization (0.34

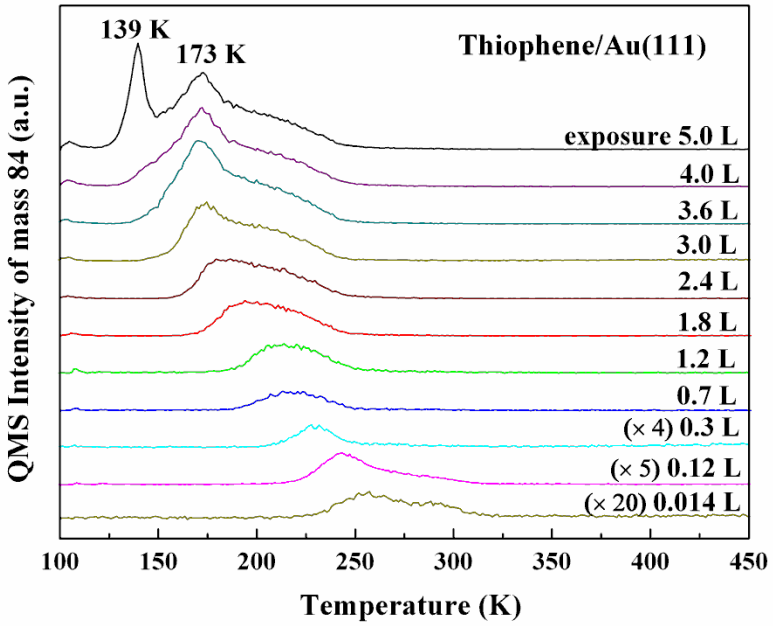

Figure 3.1: TPD spectra for thiophene adsorbed on Au(111) at 95 K as a function of exposure. The baselines are offset for viewing clarity.

eV) of solid thiophene.[65] Based on these considerations, we attribute the 139 K peak to desorption from a second layer or multilayer of weakly bound thiophene molecules.[50] Consequently, a vapor-saturated surface of chemisorbed thiophene molecules is reached for an exposure of ~4.0 L at 95 K and higher exposures lead to the formation of thiophene multilayers.

To estimate the absolute thiophene coverage in our experiments, we compare our TPD spectra with those obtained by Milligan et al., under similar dosing conditions [51]. In that work a quantitative measure of the thiophene coverage on Cu(111) was achieved by calibrating the S-atom Auger intensities against a surface prepared with a known S-atom coverage (0.43 ML; 1 ML was defined as one S-atom per surface copper atom). Based on such a calibration, the saturated coverage for the lying-down and standing-up (compressed) phases of thiophene/Cu(111) were determined to be 0.08 ± 0.03 ML and 0.14 ± 0.03 ML, respectively.[51] Substantially higher thiophene coverages of ~0.4 ML (two thiophene molecules per five surface gold atoms) were found for a self-assembled monolayer (SAM) formed on Au(111) by immersion in an ethanolic solution of thiophene.[66] Based on similarities in the TPD spectra, we expect the saturated chemisorbed layer on Au(111) prepared in this work (~ 4 L) to be similar to that determined for thiophene on Cu(111), i.e., 0.14 ML,[51] which is about one-third of that of the thiophene SAM.[66]

According to previous studies, the desorption peaks at 260–186 K and 173 K are associated with two phases of chemisorbed thiophene molecules with different binding configurations.[50,51,53,64] Specifically, the desorption feature at 260–186K is associated with molecules lying with their axes tilted slightly out of the surface plane, whereas, the peak at 173 K corresponds to desorption from a compressed layer, in which the molecules are tilted farther from the surface. Assuming first order desorption kinetics (Redhead model)[42] and pre-

exponential factors of 10^{13} s^{-1}, we calculate desorption energies of 0.46 eV and 0.70 eV for the TPD peaks at 173 K and 260 K, respectively. These energies are in excellent agreement with the results of previous studies that reported desorption energies of 0.48 eV for the "lying-down" state and 0.69 eV for the "standing-up" state of chemisorbed thiophene.[64]

3.3.2 Two-photon photoemission

Figures 3.2 and 3.3 show 2PPE spectra of clean Au(111) and thiophene adsorbed on the Au(111) taken at a photon energy of 4.659 eV for a range of exposures up to 4.0 L. The spectra are displayed as a function of final state energy referenced to the Fermi level (E_F),

$$E_{final} - E_F = E_{kin} + \Phi, \qquad (3.2)$$

where E_{kin} is the measured kinetic energy (corrected for the applied bias) and Φ is the work function (see Equation 3.3, below).

In acquiring the 2PPE spectra, we found no evidence for photoinduced desorption or decomposition of the thiophene; the spectra did not change with laser exposure time and post-irradiation TPD measurements did not show other molecular species aside from thiophene desorbing from the surface. In addition, the clean Au(111) surface could be restored by flashing the surface to 450 K, as verified by a change in the work function back to that measured for the bare Au(111) surface (5.55 eV) prior to exposure to thiophene, as well as the re-appearance of the Au(111) surface state near the Fermi level (See Figure 3.3).[67,68]

The prominent shift of the photoemission threshold from ~5.55 to ~4.75 eV in 2PPE spectra shown in Figure 3.2 indicates a decrease in the work function with increasing thiophene coverage. The work function, Φ, shown in the inset of Figure 3.2 was determined from the 2PPE spectra by the expression:

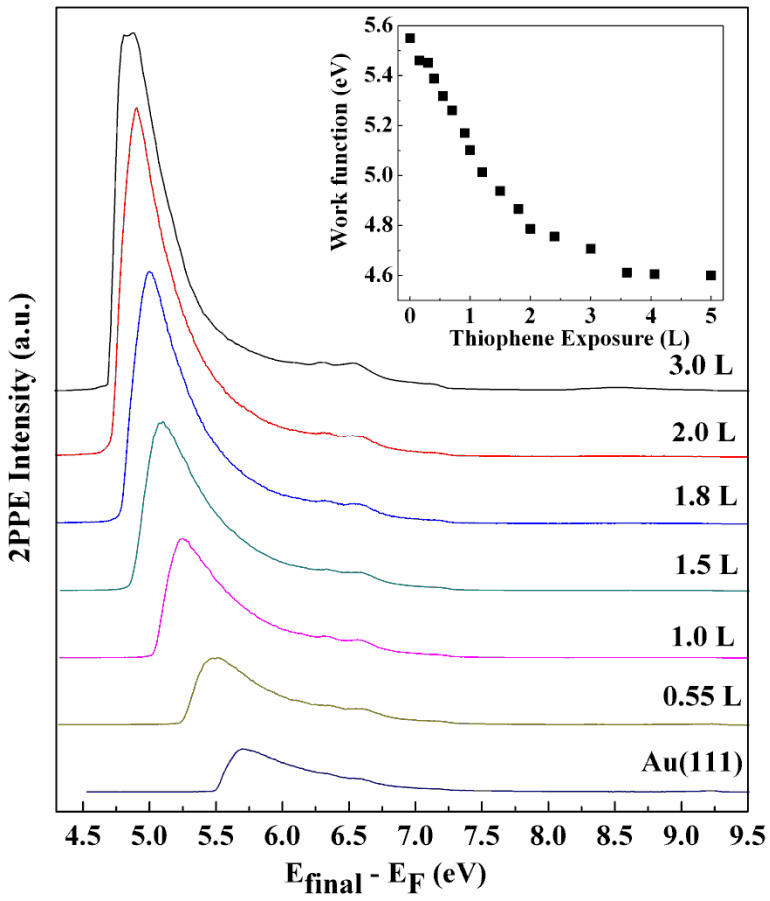

Figure 3.2: Monochromatic 2PPE spectra of thiophene on Au(111) as a function of exposure. The inset shows the work function variation with the exposure, determined according to Equation 3.3 in the text. The photon energy was 4.66 eV.

$$\Phi = 2h\nu - E_F + E_{cs} \tag{3.3}$$

where $h\nu$ is the photon energy and E_F and E_{cs} are the observed energies for the cutoff of photoemission from near the Fermi level and the cutoff of the secondary electrons at the photoemission threshold, respectively. The observed work function monotonically decreases with increasing thiophene exposure up to 4.0 L, beyond which it levels off to a value of 4.60 eV. The decrease in the work function is related to the dipole moment at the thiophene/Au(111) interface induced by the adsorbed thiophene molecules. As described by the Helmholtz equation, the work function change is proportional to the number of adsorbed molecules and the interface dipole moment of each molecule.[69] We note that the total change in work function relative to the bare Au(111) surface, $\Delta\Phi \approx$ -0.95 eV, is comparable to that observed for a fully-saturated thiophene adlayer on Si(100) which was prepared at a similar thiophene exposure.[70]

Figure 3.3 shows an expanded view of the 2PPE spectra at high final state energies. For exposures below ~1.0 L, the surface state of Au(111) near E_F is the most prominent feature. The small rise in the photoemission intensity in the bare Au(111) spectrum near 8.2-8.3 eV has been previously assigned to the unoccupied upper band edge (UBE) of the Au(111).[71,72] As the thiophene exposure is increased above 1.0 L, the photoemission intensity between 8.2 eV and 8.9 eV increases significantly and the Au(111) surface state is no longer discernable. Above an exposure of ~1.5 L, the intensity gain takes the form of a broad feature (denoted as S_u) that evolves into a distinct peak with a final state energy of ~8.46 eV at saturation coverage (4 L exposure). Although relatively broad, the S_u feature appears to become narrower and shift to lower final state energy (~0.18 eV) with increasing thiophene exposure.

In 2PPE experiments, the origin of photoelectrons from either an occupied or unoccupied state can be distinguished by measuring the dependence of the photoelectron kinetic energy on

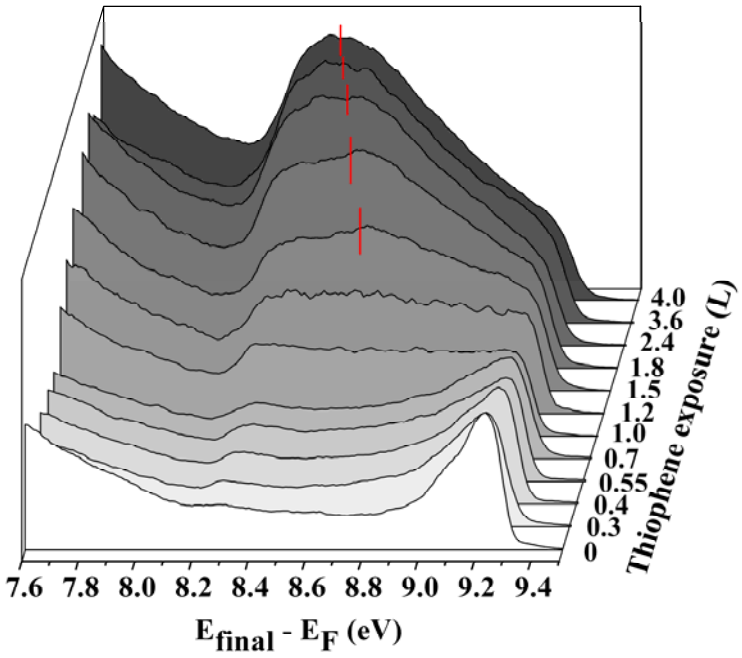

Figure 3.3: High final state energy region of monochromatic 2PPE spectra of thiophene on Au(111) as a function of exposure. The vertical bars indicate the estimated peak position of the unoccupied state, S_u.

photon energy. Figure 3.4 (left panel) shows that the slope of the kinetic energy shift of the S_u peak is equal to one, within experimental uncertainty, indicating that the S_u peak originates from an unoccupied state. With this assignment, the observed change in final state energy with coverage (see Figure 3.3) corresponds to a shift in the S_u peak towards E_F with increasing thiophene coverage. At saturation coverage in our experiments (~4.0 L), the position of the S_u unoccupied state lies 3.80 ± 0.01 eV above the Fermi level.

Unoccupied states observed in the 2PPE spectra of Au(111), Ag(111) and Cu(111) surfaces with molecular adlayers can usually be assigned to image potential states of the metal surface, or unoccupied states of the adsorbate/metal system.[1,73,74] The latter is populated in 2PPE by photoinduced electron transfer from the valence band (substrate mediated excitation). Image potential states are typically distinguished by narrow 2PPE peaks, strict symmetry constraints and energy dispersive behavior typical of a free electron.[74-77] On bare Au(111), the n = 1 image state is located at 4.75 eV above the Fermi level and can not be reached with a photon energy less than 4.95 eV. [78] The adsorption of thiophene would be expected to shift the image state to lower energies as has been reported in 2PPE studies of tetra-*tert*-butyl-azobenzene/Au(111),[79] where the n = 1 state appears at ~0.6 eV below the vacuum level. Given a work function decrease of 0.5–1.0 eV, this would place the n = 1 image state in the same final state energy region as the broad S_u state in our spectra. Alternatively, the S_u peak could result from the excitation of an unoccupied level formed by the interaction of the affinity or LUMO levels of thiophene with the Au surface. The LUMO orbitals of thiophene are known from gas-phase studies to lie at ~5.16 eV above the ground state.[80,81] Electronic interactions with the Au(111) surface would be expected to lower the LUMO energies so that some would lie below the vacuum level of the thiophene/Au(111) surface (≥ 4.6 eV) and be accessible to the UV excitation

energy (~4.66 eV) used in this work. In comparison to the n = 1 image potential state of Au(111), the unoccupied levels of the thiophene/Au(111) surface could exhibit a wider range of possible band symmetries, 2PPE peak widths and band dispersion behavior that are sensitive to the details of the adsorbate-metal bonding. A more detailed discussion of the electronic structure of the thiophene/Au(111) surface is presented in Section 3.3c.

Angle-resolved 2PPE measurements were performed to determine the dispersion of the S_u state. Figure 3.4 (right panel) shows the results of these measurements where the S_u peak position is plotted versus electron momentum ($k_{\parallel}$). The very small kinetic energy shifts are indicative of a non-dispersive band, and a fit to the parabolic band model results in a relatively large effective electron mass, $m_{eff} = (19 \pm 5)\, m_e$. The observation of a high m_{eff} would suggest that the S_u is not an image state (n = 1) originating from Au surface as these typically exhibit free electron behavior with parabolic dispersive bands with small m_{eff}.[77] A strong corrugation of the electrostatic potential in the adlayer, however, can result in localization of an image state such as that found for C_{60} on Cu(111) where there is substantial charge transfer from the metal to the C_{60} layer.[73,82] The relatively weak interaction of thiophene with the Au(111) surface results in very little charge transfer from Au to thiophene and the resulting electrostatic corrugation of a thiophene adlayer would be expected to be substantially less. The alternative assignment for the S_u state is that it is associated with an unoccupied level with substantial electronic contributions from adsorbed thiophene (e.g., LUMO orbital). The large effective mass, $(19 \pm 5)\, m_e$, suggests the interaction and/or ordering of neighboring thiophene molecules is insufficient to introduce band dispersion, e.g., the S_u state is localized on individual thiophene molecules.

Additional insight into the nature of the S_u state is provided by the polarization dependent measurements shown in Figure 3.5. For these experiments, 2PPE spectra were taken with both

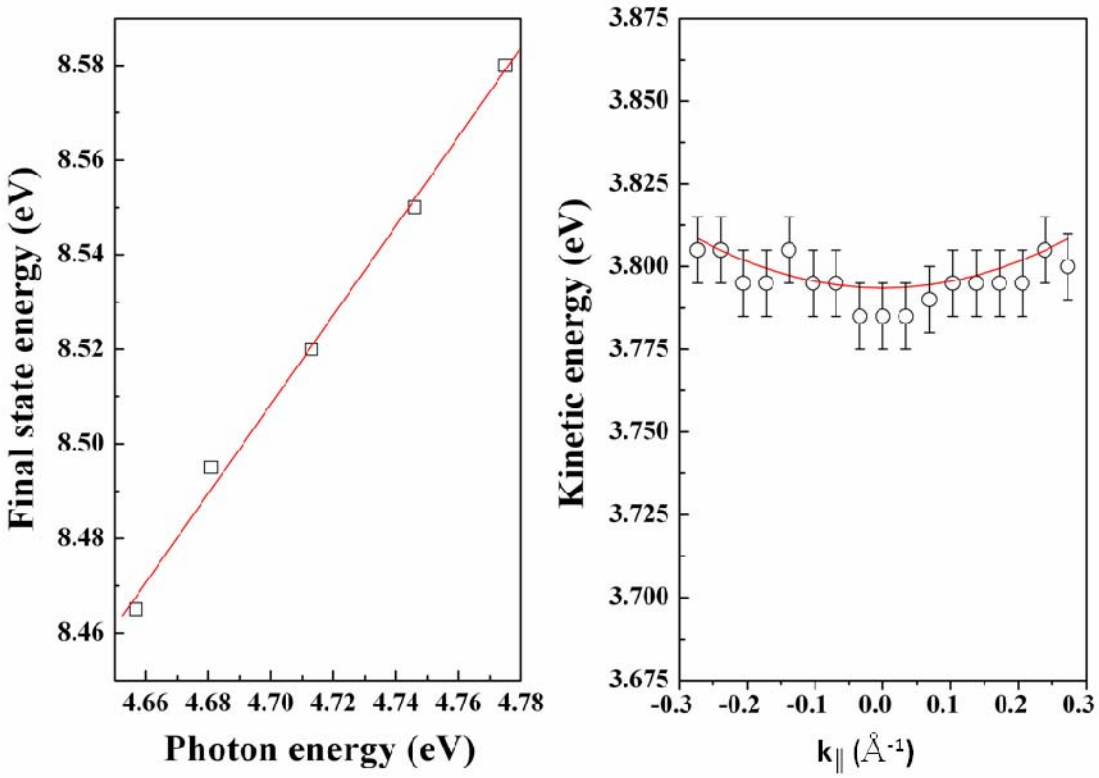

Figure 3.4: (Left) The photon energy dependence of the unoccupied state S_u for a thiophene exposure of 4.0 L on Au(111). The solid line is a linear fit with a slope of 0.94 ± 0.10. (Right) Dispersion of the unoccupied state S_u measured for a thiophene exposure of 4.0 L on Au(111). The solid line is a parabolic fit to free-electron-like dispersion with an effective electron mass of (19 ± 5) m_e. The photon energy was 4.60 eV.

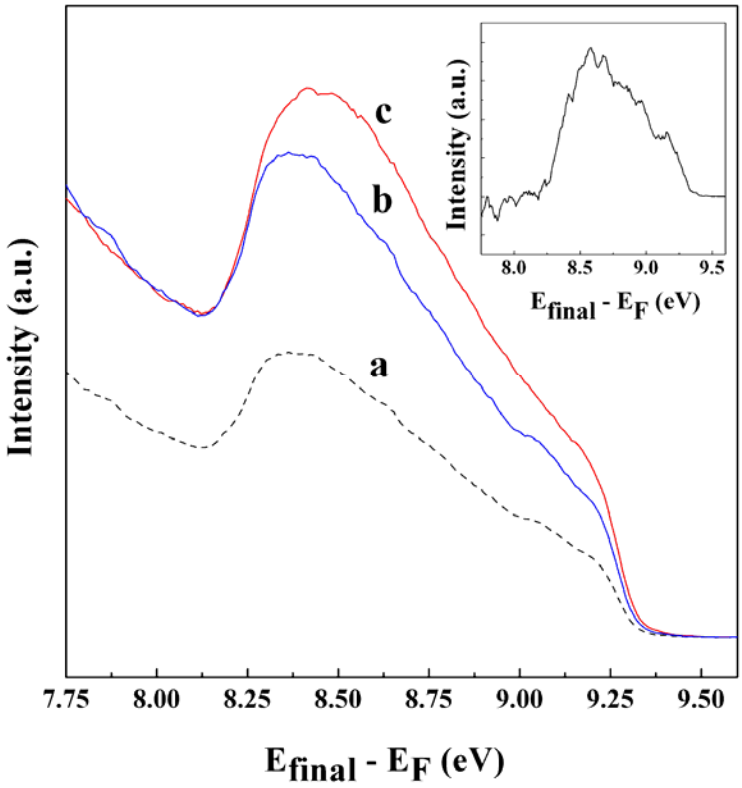

Figure 3.5: Polarization dependence of the high final state energy region of monochromatic 2PPE spectra for a thiophene exposure of 4.0 L on Au(111). (a) s-polarized pump and probe; (b) s-polarized with intensity normalized at the low final state energy, as discussed in the text; (c) p-polarized pump and probe. The inset shows the difference of 2PPE spectra pump and probe by p-polarized and s-polarized light after normalization.

pump and probe photons having either s-polarization (Figure 3.5a) or p-polarization (Figure 3.5c). As seen in Figure 3.5, the S_u state decreases by only a factor of ~1.7 in changing the pump and probe pulses from p-polarized to s-polarized. By contrast, image potential states of the (111) surfaces of the metals Cu, Ag and Au are observed to vanish when using s-polarized light for the probe (ionization) laser pulse (σ symmetry).[49,76,83,84] Although diminished in intensity, the S_u state is clearly observable with s-polarized light which supports the assignment of the S_u peak to an unoccupied level containing both thiophene and Au orbital contributions.

More information on the symmetry properties of the S_u state can be obtained by a quantitative comparison of the s- and p-polarized 2PPE spectra. Specifically, Figure 3.5b shows the s-polarized spectrum normalized to the p-polarized data at lower final state energies (7.75-8.15 eV) where we expect the photoelectrons to originate primarily from the Au valence bands. In this energy range, the change in 2PPE intensity is expected to be simply proportional to the change in the absorbance of the Au(111) surface for s- and p-polarized light at a given incidence angle and pump photon energy.[76] Using optical constants for Au at photon energy of 4.66 eV and an incident angle of 47.5°, we calculate the ratio of the absorbance of s-to-p polarized light to be ~0.64.[85] This calculated value is very close to the normalization factor, 0.6, needed to overlap the s- and p-polarized 2PPE spectra at energies away from the S_u resonance (Figure 3.5, traces b and c). Assuming an indirect (substrate mediated) excitation process, the residual change in the intensity of the S_u state after normalization could result from symmetry constraints imposed on the transition dipole of the ionization step, which in turn reflects the symmetry of thiophene and Au orbitals contributing to the S_u state.[76] As the molecules are expected to be tilted away from the surface normal at all coverages studied in this work, the S_u state will contain admixtures of orbitals with σ and π symmetry. As a result, the transition dipole for ionization of the S_u

intermediate state will likely lie at an angle to the surface normal and yield signal intensity for probe photons with both s- and p-polarization. This expectation is consistent with the data in Figure 3.5, but we also note that the S_u state peak position appears to shift to slightly lower final state energy when s-polarized light is used. The difference spectrum between the p-polarized and normalized s-polarized 2PPE spectra shown in the inset in Figure 3.5 exhibits a peak at higher final state energy compared to the S_u state peak excited by p-polarized light. This observation may indicate the presence of more than one overlapping intermediate state resonances with different symmetries.

As noted above, the lack of dispersion for the S_u state suggests that the intermolecular distance is too large or the ordering is insufficient for effective electronic overlap that could give rise to band formation. This conclusion is based on comparison with previous 2PPE and STM studies of other sulfur-containing molecules on Ag and Au surfaces. For example, an unoccupied state observed for methylthiolate on Ag(111) was observed to be non-dispersive at low coverage with large intermolecular spacing, whereas an effective electron mass of 0.5 m_e was observed at high coverage,[12] where the intermolecular spacing is 4.4 Å.[86] Similar behavior was observed for 1-hexanethiol SAMs adsorbed on Au(111).[15] For the latter, an unoccupied σ* state from the Au–S bond was localized ($m_{eff} > 12\, m_e$) at low coverage where the molecules lie down on the surface. At high coverage the molecules tilt ~60° from the surface plane to form the well-known c(4×2) phase with an intermolecular spacing of ~5 Å in the surface plane (~4.5 Å spacing perpendicular to the molecular axes), a packing similar to that in bulk paraffins.[87-90] At this packing density, the effective electron mass of the σ* state was observed to decreased slightly (9 m_e).[15] These observations suggest that delocalization occurs when the molecules are able to pack at distances approaching their van der Waals diameter. Thus, for thiophene, we might

expect delocalization to become important when the intermolecular π–π spacing approaches ~3.6 Å (the van der Waals diameter of sulfur) to 3.35 Å (the interlayer spacing of graphite).[91] This limit is approached for thiophene SAMs on Au(111), which form rows of molecules with intermolecular distances of 4–5 Å and inter-row spacings of 8.8 Å and 12 Å depending on thiophene density (0.23 ML - 0.4 ML).[66,92] However, because the vapor-saturated chemisorbed layer in our experiment corresponds to a thiophene coverage of about 0.1–0.2 ML, the molecules are spaced at an intermolecular distance in the range of 6–9 Å; thus their packing density is too low to result in significant band formation and dispersion.

3.3.3 Comparison with DFT calculations

To gain more insight into coverage-driven changes of molecular geometry and the origin of the S_u electronic state, we performed DFT calculations for three thiophene coverages spanning the range investigated experimentally. The optimized thiophene binding structures are displayed in Figure 3.6, and the corresponding adsorption energies and structural parameters are given in Table 3.1, along with experimental activation energies for desorption for comparison. For all coverages studied, thiophene binds with the S-atom residing on an Au-atom top-site and has an internal molecular structure which is essentially the same as that of the isolated molecule. A similar preference for top-site binding was found for thiophene on Cu(111) using x-ray standing wave adsorption experiments[51] and on Cu(110) by *ab initio* calculations.[57] At coverage of 0.062 ML, the thiophene adsorption energy is -0.37 eV and molecule is tilted from the surface plane by 23.3° with a S–Au bond length of 2.62 Å. As the coverage increases to 0.25 ML, the thiophene molecule tilts up to 48.5°. Over the same range of coverage, the S–Au distance increases (+0.48 Å) while the adsorption energy decreases (+0.20 eV) due to decreased

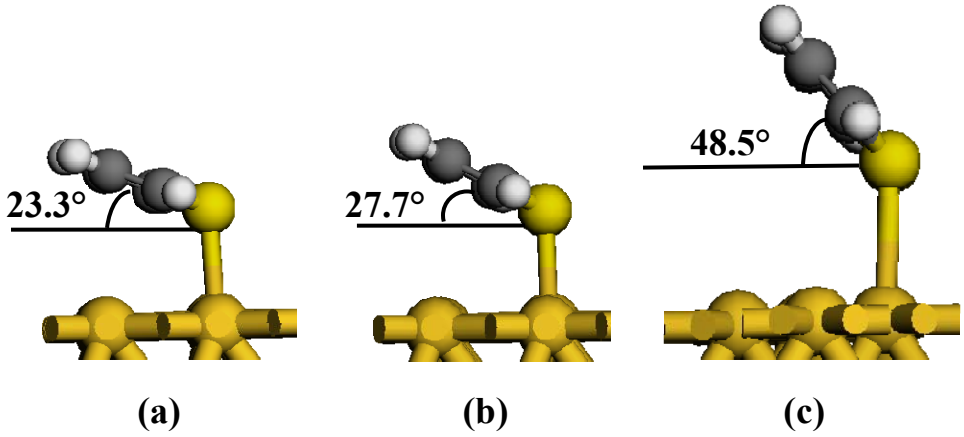

Figure 3.6: The DFT-optimized configurations for thiophene molecule adsorbed on Au(111) at different coverages: (a) 0.062ML, (b) 0.11 ML, and (c) 0.25ML.

Table 3.1: Adsorption energies and structural parameters for the DFT-optimized geometries of thiophene adsorbed at the on-top site of the Au(111) surface and corresponding activation energies for desorption extracted from the TPD measurements.

Thiophene coverage (ML)	θ (°)[a]	r(S-Au) (Å)[b]	E_{ad} (eV)	Experimental E_d (eV)[c]
0.062	23.3	2.62	-0.37	0.70[d]
0.11	27.7	2.53	-0.35	0.50
0.25	48.5	3.10	-0.17	0.46

[a] The tilt angle of thiophene (θ) is defined as the angle of the thiophene molecular plane with respect to the surface plane.

[b] The r(S-Au) is the distance between the S atom and the surface Au atom on which thiophene adsorbs.

[c] Experimental activation energies estimated using Redhead's peak temperature method.

[d] Thiophene coverage approaching < 0.01 ML.

electronic interaction with the Au substrate (see Table 3.1, and discussion of density-of-states results below). These results are consistent with the shift of the thiophene TPD peak to lower desorption temperatures with increasing thiophene exposures (see Figure 3.1). In addition, our calculations agree well with those of Nambu, et al., who studied the tilt angle of thiophene on Au(111) by NEXAFS measurements.[50] In that work, the tilt angle between the thiophene and surface plane was determined to be 22 ± 3º and 55 ± 5º for coverages corresponding roughly to exposures of 2.4 L and 4.0 L, respectively, in our experiments (based on comparison to the coverages cited for the carefully-calibrated TPD measurements of Milligan et al.).[51] The agreement with our calculations supports an assignment of a transition from a structure wherein the thiophene is lying roughly parallel to the surface to one where it is tilted closer towards the normal at exposures greater than approximately 2.4 L. The calculated adsorption energies at all coverages are smaller than the estimated activation energies from TPD results, which we attribute to the well-known tendency of GGA to underestimate the adsorption energies.

Figure 3.7 shows the results of DFT density of states calculations for the 5d orbitals of the Au atom bound to the thiophene molecule (Figure 3.7a), the projected density of states (PDOS) of the entire thiophene molecule (Figure 3.7b) and the PDOS of the sulfur 3p orbital (Figure 3.7c). The contributions from the Au 5d orbitals to the unoccupied DOS above the Fermi level are very weak and featureless, and thus inconsistent with the well-resolved S_u peak observed in 2PPE (Figure 3.3). On the other hand, contributions from the thiophene molecular orbitals to the unoccupied DOS (Figures 3.7b and 3.7c) are much more pronounced and lie ≥ 2.5 eV above the Fermi energy. The latter would appear close to the thiophene-induced features seen in the experimental 2PPE spectra (Figure 3.3 and Figure 3.5) which correspond to intermediate state energies of 3.5–4.5 eV above E_F.

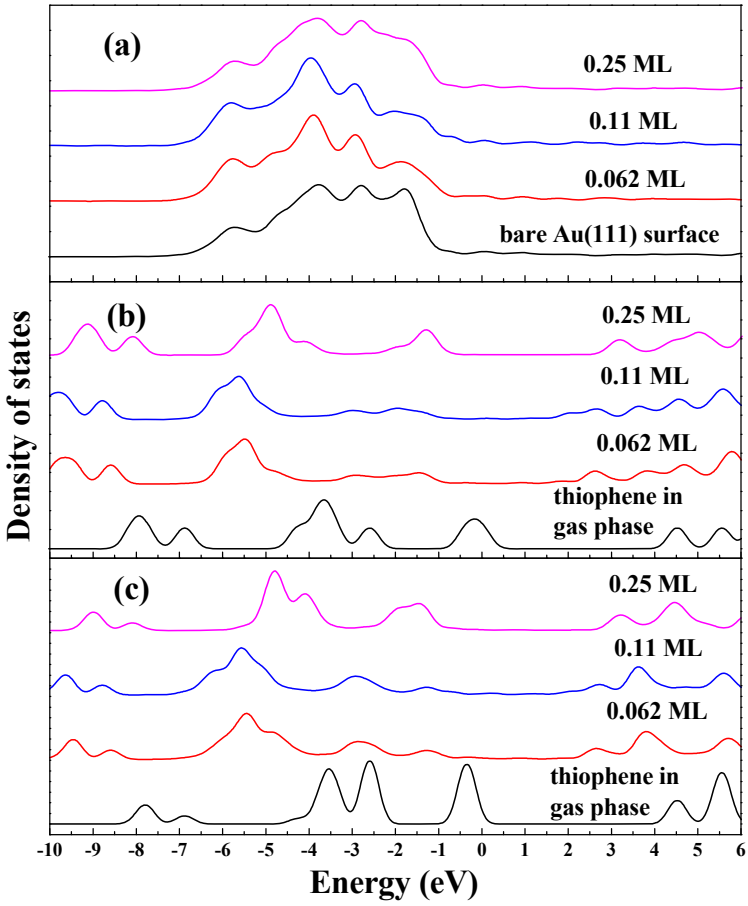

Figure 3.7: Calculated PDOS for thiophene adsorbed on Au(111) as a function of coverage. (a) PDOS of the 5d orbital of the surface Au atom interacting with thiophene directly; (b) PDOS of the thiophene molecule; (c) PDOS of the S 3p orbital.

Upon closer inspection, the DOS results reveal a significant coverage dependence of the nature of the thiophene–Au interaction. At the lowest coverage (0.062 ML), the redistribution of the Au atom DOS (Figure 3.7a) and the significant downshift and rehybridization of the thiophene orbitals (Figure 3.7b) are consistent with reasonably strong bonding between the thiophene molecule and the Au(111) surface. As the coverage increases to 0.25 ML, the calculations indicate that the degree of rehybridization with the Au surface is diminished; the PDOS for both Au and thiophene shift and become narrower, evolving to resemble more closely that of the bare surface and free molecule.

The narrowing of the thiophene PDOS with increasing coverage is consistent with the observed coverage-dependence of the width of the S_u peak (Figure 3.3). At low coverage (0.062 ML and 0.11 ML), photoexcitation into the broad thiophene PDOS would lead to broad features in the 2PPE spectra that are also weak due to the low thiophene coverage. At high coverage (0.25 ML), 2PPE via the narrowed intermediate states should result in more intense and narrower photoelectron peaks. These trends are qualitatively similar to that observed in the 2PPE spectra where a broad feature at low thiophene exposures (1.0–1.8 L) evolves into a stronger, well-defined peak (S_u) at saturation coverage (~4.0 L). The polarization data in Figure 3.5 suggest that even at saturation coverage, the S_u resonance may be composed of overlapping bands with different thiophene-Au orbital hybridization (symmetry).

As noted above, the DFT results indicate a shift in the molecular PDOS away from the Fermi level as the coverage increases (see Figure 3.7). This trend is opposite to the 2PPE results which show a small shift (~0.2 eV) of the thiophene-induced states toward the Fermi level. This discrepancy between the DFT calculations and 2PPE experiments is likely a result of the charge induced polarization of the Au surface and the surrounding molecules which are not accounted

for in static DFT calculations. Substrate-mediated photoexcitation to the S_u state of adsorbed thiophene can be viewed as charge transfer to form a transient anion which subsequently rapidly decays back to Au surface or is photodetached in the probe ionization step. The transient anion will induce an image charge interaction with the Au(111) surface and an ion-induced dipole interaction with the surrounding thiophene molecules. The former is given by given by -Ry/(2κz), where Ry is the Rydberg constant, z is the adsorbate-surface distance, κ is the permittivity in atomic units.[49,93] According to the DFT calculations summarized in Table 3.1, the thiophene-Au bond distance increases with increasing coverage, and as a result the image charge interaction will decrease. This will have the effect of shifting the energy of the S_u peak away from the Fermi level, contrary to what is observed in the 2PPE experiment. However, stabilization of the transient anion resulting from charge-induced polarization of the surrounding molecules increases with increasing coverage and counters the trend in the image charge interaction. Dipole-induced polarization of surrounding adsorbates has also been invoked to explain the shifts in LUMO resonances of C_{60} adsorbed on Au(111) and Cu(111).[94,95] The polarization energy of surrounding molecules can be estimated from the Born formula which assumes a point charge embedded in a continuous dielectric medium.[96] To calculate the Born polarization energy, we use the estimated intermolecular distance of thiophene molecules at saturation coverage, 9 Å, as the radius of thiophene anion and assume that the surface value is only half that of the bulk.[97] The resulting polarization energy is ~0.25 eV. By comparison, the decrease in the image-charge attraction potential is less than 0.16 eV using the calculated increase in bond length (2.62 Å to 3.10 Å) from Table 3.1. Although these calculations are crude estimates at best, they do show that it is possible to rationalize the observed coverage dependent

shift of the S_u level as a combination of opposing shifts in the PDOS, image charge and charge-induced dipole interactions.

3.3.4 Comparison to pyridine on Cu(111)

Finally, we compare our results for thiophene on Au(111) to that of the another heteroatom aromatic system, pyridine, on Cu(111).[49] The TPD spectra are similar in that both systems exhibit two desorption peaks corresponding to two different phases. Specifically, the TPD and 2PPE data were interpreted as indicating that the pyridine molecules undergo a change in configuration from molecules lying-down (π-bonded) to molecules tilting up from the surface (lone-pair interaction of the N-atom with Cu; "n-bonded") as the coverage increases to fill the monolayer. The total change in work function for pyridine/Cu(111) at high coverage is substantially greater ($\Delta\Phi \approx$ -2 eV) than that of thiophene/Au(111) ($\Delta\Phi \approx$ -0.95 eV) which is consistent with the much larger dipole moment for pyridine (2.2 D) compared with thiophene (0.55 D).[98] The pyridine/Cu(111) 2PPE spectra also differ substantially from those for thiophene/Au(111) due to the presence of two narrow photoelectron features which were assigned as n = 1 and n = 2 image states. In the mixed phase region, the 2PPE spectra exhibited two n = 1 image states attributed to different monolayer phases (π-bonded and n-bonded) with different local work functions. A weak 2PPE feature lying ~1.4 eV below the vacuum level was attributed to unoccupied π* states from chemisorbed pyridine molecules. This assignment implies a downward shift of the π* states of ~2–2.6 eV relative to their gas-phase position. For thiophene/Au(111), we observe a shift of similar magnitude; the S_u unoccupied state lies ~0.7–0.8 eV below the vacuum level which corresponds to a shift of ~1.8–1.9 eV relative to the LUMO measured in the gas-phase.[99] In the pyridine/Cu(111) case, the unoccupied states shift to

lower final state energy with increasing coverage and change in bonding geometry, similar to the behavior observed here for the S_u state in thiophene/Au(111) (see Figure 3.3).

3.4. Summary

2PPE and DFT calculations have been used to investigate the interfacial electronic properties of thiophene/Au(111). Adsorption of thiophene on Au(111) lowers the work function ($\Delta\Phi \approx$ -0.95 eV) as a result of the induced dipole layer at the Au-thiophene interface. Interaction between thiophene and Au(111) also induces an unoccupied state, S_u, which shifts down in binding energy (referenced to the Fermi level) with increasing thiophene coverage. DFT calculations suggest that the unoccupied state can be assigned to a thiophene LUMO-derived state of mixed sulfur and carbon p-π character. The energy width and position of this state is dependent upon the adsorption geometry of thiophene molecules. Specifically, when the molecules tilt up away from the surface plane with increasing coverage, the unoccupied state becomes narrower and shifts to lower energy. DFT calculations show broad unoccupied states whose decreasing width correlates well with the narrowing observed in 2PPE spectra with increasing coverage. The shift of the S_u state towards to the Fermi level is attributed to stabilization of the transient anion due to the polarization of the surrounding thiophene molecules. The vapor-saturated thiophene layer exhibits an unoccupied state located 3.80 eV above the Fermi level; an electron excited to this level is substantially localized, as indicated by its large effective electron mass of (19 ± 5) m_e. Localization of the electron is consistent with the large intermolecular distances that limit π-π interactions at the relatively low coverages investigated in our experiments. Such localization of the unoccupied state would be expected to have a negative impact in possible molecular electronics applications where conduction of

charge from molecule to molecule is important. This work provides an example of a system wherein the interfacial electronic structure is sensitive to the molecule–surface binding and molecular packing, showing that control of interfacial electronic properties requires detailed control of the structure of the interface.

Chapter 4. Adsorption structures and electronic properties of 1,4-phenylene diisocyanide on Au(111)

This section was submitted to *J. Phys. Chem. C*

4.1. Introduction

The electronic properties of organic molecules on metal substrates are of significant interest because of their central role in molecular electronics.[3,4,100] Specifically, the energy level alignment of molecules bound to the metal surface determines the efficiency of charge transport between adsorbed molecules and metal substrate.[3,47] Of particular importance are the energy positions of the highest occupied molecular orbital (HOMO) and lowest unoccupied molecular orbital (LUMO) relative to the Fermi edge (E_F) of the metal contact, which are indicative of the junction bias required for hole and electron conduction, respectively. As a consequence, experimental characterization of the level structure of molecule-metal interfaces is essential to understanding and predicting the performance of molecular electronic devices.

The thiol-gold interaction is the most extensively studied contact in molecular electronics applications, largely because the strong chemical bond between the sulfur and gold atoms allows the formation of ordered overlayers, e.g., self-assembled monolayers (SAMs).[88,101,102] However, susceptibility to oxidation[102-104] and a high electron transfer barrier[15] have motivated the search for new molecular junctions. More recently, isocyanides have attracted widespread interest for this application as the N≡C triple bond is expected to act as an effective bridge for connecting pπ orbitals of aromatic molecules with dπ orbitals of the metal contact. Indeed, recent conductance measurements using nanoparticle-molecule junctions showed that molecules containing terminal isocyanide groups exhibit an order of magnitude increase in conductance over the same molecule

with a terminal thiol group.[18] Theoretical calculations also predicted a six-fold increase in conductance of Au-CN junctions compared to Au-S interfaces.[19] However, some groups have reported the opposite trend. For instance, conducting probe atomic force microscopy was used to investigate SAMs of several aromatic systems with isocyanide and thiol terminal groups on a Au surface and found that the Au-CN junctions were more resistive.[20] The apparent disagreement among experiments and theory means that no clear picture has emerged as to the effectiveness of the Au-CN interface for charge transport. Moreover, meaningful comparisons with theory will require more direct experimental probes of the interfacial electronic structure on isocyanide-covered surfaces where the molecular coverage and morphology are known.

In this work we examined the morphology and electronic structure of 1,4-phenylene diisocyanide (PDI) molecule adsorbed on a Au(111) surface. The PDI/Au(111) system is an attractive model for studies of metal-isocyanide interactions as it represents the simplest aromatic isocyanide that can act as a π-conjugated molecular bridge between two metal electrodes. Previous experimental measurements of the conductance gap of PDI SAMs on a Au(111) surface placed the HOMO level 0.38 ± 0.1 eV below E_F.[105] To our knowledge, no experimental information on the relative energy of the LUMO level of PDI–Au contacts has been reported. Inverse photoemission studies of the related molecule, 4,4'-biphenyl diisocyanide (BPDI) with two phenyl rings between the –NC end groups, on Au(111) revealed a broad feature at 4 eV above E_F. After deconvolution, a peak at 5.3 eV above E_F was assigned to the LUMO level of BPDI.[106] Considering that PDI has a somewhat smaller HOMO–LUMO gap (8.6 eV[107]) than BPDI (10.0 eV[106]) in the gas-phase, the LUMO–E_F energy gap for PDI/Au(111) would be expected to be somewhat lower than 5 eV, but likely still a substantial barrier to electron transmission across the metal–molecule interface.

The electron transport properties of PDI–metal junctions have been the subject of a number of theoretical studies. Xue and Ratner, using a Green's function method and a single PDI molecule bridging two Au electrodes, predicted the LUMO level to be in near resonance with E_F of the Au contact.[108] Calculations of electron transmission across the Au–PDI–Au bridge showed a large zero-bias conductance which was attributed to near resonant tunneling through the LUMO. More recently, Li et al., explored the electronic structure of PDI on Au(111) at low coverage under the assumption that the molecules are bound with their molecular axes perpendicular to the surface via one Au–CN linkage.[107] The LUMO–E_F gap for the Au–CN contact was calculated to be 0.7 eV suggesting a substantially smaller barrier for electron transmission compared to that expected based on the inverse photoemission measurements of BPDI/Au(111).[106] However, DFT calculations generally underestimate HOMO–LUMO gaps compared to experiment.[109] To address this, Li et al., performed additional calculations including self-energy corrections and surface polarization effects. With these corrections, the LUMO state of PDI on Au(111) shifted further from the E_F level by about 1.5–2 eV,[110] a value still significantly smaller than that for BPDI/Au(111).[106] The general discrepancy among experimental and theoretical studies makes it important to obtain direct experimental determinations of the energy level alignment of the Au–PDI interface for understanding and interpreting the more macroscopic transport measurements.

In addition to direct determination of the LUMO level energy, it is important to understand the relationship between the electronic structure and the molecule–metal chemical interactions and molecular binding geometry. In both the experimental and theoretical studies discussed above it has been assumed the PDI molecules bind end-on to the Au surface through a single Au–C bond with a terminal η^1 geometry. This bonding geometry is consistent with

infrared spectroscopy measurements which indicate the presence of two C≡N frequencies corresponding to a free –N≡C group and one shifted to higher frequency which was assigned to –N≡C–Au.[111-114] Assuming an end-on geometry, Li et al., used DFT to calculate binding energies and arrangements for a 1 ML coverage of PDI molecules bound at atop sites on Au(111), with both parallel ($\sqrt{3} \times \sqrt{3}$) and herringbone ($2\sqrt{3} \times \sqrt{3}$) configurations.[107] Very recent STM imaging experiments of PDI deposited on Au(111) at low coverage (0.05 ML), however, showed one-dimensional (1-D) chain-like structures whose repeat distance is consistent with chains of alternating PDI molecules and Au adatoms, i.e., $[–Au–PDI–]_n$ monomer subunits.[115] In this model, the PDI molecules lie parallel to the surface and are bonded at each end to Au adatoms which are pulled from the surface (or step edge) by the strong Au-isocyanide interaction. It is not known if this chain-like structure is retained at the much higher coverage corresponding to a PDI SAM. A surface morphology of extended molecular wires with interspersed Au contacts offers interesting possibilities for charge transfer, but coverage dependence studies are clearly needed to examine how such structures influence the electronic structure of PDI–Au surfaces.

In this work, we have studied the adsorption structures and electronic properties of PDI on Au(111) with temperature programmed desorption (TPD), two-photon photoemission (2PPE) spectroscopy, scanning tunneling microscopy (STM) and spectroscopy (STS). STM images show that molecules deposited at 95 K adsorb in small disordered patches and at step edges. 2PPE measurements of such surfaces indicate that the work function decreases rapidly with increasing coverage and reveal the presence of an occupied electronic state 0.88 eV below the Fermi level. The occupied state is also observed by STS. Annealing to 300 K results in a remarkable change in both the physical and electronic structure of the interface. STM images show a dramatic rearrangement: the disordered structures found at 95 K give way to long linear (1-D) chains

extending essentially uninterrupted for many tens of nanometers, entirely covering the surfaces of the Au(111) terraces. The lengths over which the chains remain straight are essentially limited by the size of the underlying Au terraces. At high coverage the chains dominate the surface topography with essentially all of the molecules bound in chain structures. The periodicity of the corrugation along the chains is equal to that observed at much lower coverages by Boscoboinik et al.,[115] and consistent with the formation of an extensive overlayer consisting of parallel [–Au–PDI–]$_n$ chains. This structural rearrangement is accompanied by a large decrease in the work function at all coverages. In addition, an *unoccupied* state with an energy of 3.32 eV *above* the Fermi level is observed in the 2PPE spectra. This relatively large LUMO–E_F energy gap suggests that the PDI–Au contact has a relatively high barrier for metal–molecule electron transmission.

4.2. Experimental methods

The experiments were performed in an ultrahigh vacuum (UHV) chamber (base pressure $< 1\times10^{-9}$ Torr) equipped with facilities for surface cleaning and thermal desorption and photoemission measurements. The Au(111) surface was cleaned following the procedure described in the previous paper.[116] The cleanness of Au(111) surface was verified by Auger electron spectroscopy (AES) and x-ray photoelectron spectroscopy (XPS). The solid PDI (99%, Aldrich) was placed in a sealed glass tube which was connected via a gate valve to a 10 mm diameter stainless steel dosing tube. The entire source was baked under vacuum to remove any impurities from the stainless steel tubes. The sample was pumped by a turbomolecular pump before each dose and the purity was confirmed by mass spectrometry. When dosing, the PDI sample was kept at room temperature and the Au(111) crystal was located ~5 cm in front of the

stainless steel tube. For the experiments reported here, the Au(111) sample was held at 95 K during the PDI dose. The coverage of PDI was varied by controlling the exposure time of the Au(111) surface to PDI vapor. For TPD experiments, the crystal was resistively heated at a rate of 2 K/s, and desorbing PDI molecules were detected with a quadrupole mass spectrometer set to monitor the flux of the parent molecular ion (128 amu). No decomposition products were observed.

The setup for 2PPE experiments has been described in detail elsewhere,[116] and a brief description is given here. Laser radiation for the 2PPE experiments was generated by a Ti:sapphire oscillator (Spectra-Physics Tsunami) pumped by a 5 W continuous wave solid-state Nd:YVO_4 laser at 532 nm (Spectra-Physics Millennia V). The tunable Ti:sapphire fundamental wavelength (700–900 nm, 80 MHz repetition rate, 0.9-W average power, 100-fs pulse width) was frequency doubled and tripled in a time-plate harmonic generator (Photop TP-2000B). Both second (~400-nm) and third harmonic (~267-nm) beams were used to perform single-color 2PPE experiments. The laser pulses were p-polarized and incident at 47.5° with respect to the surface normal. The beam was focused at the sample surface by an achromatic lens with a 38-cm focal length.

Photoelectrons were detected with a hemispherical electron energy analyzer (Specs Phoibos 100) with an instrumental resolution of 35 meV. A bias voltage of -4 V was applied to the gold crystal in order to improve the collection efficiency of low-energy electrons. This allows a more accurate determination of the low-energy secondary electron cutoff from which the surface work function is calculated. The 2PPE spectra were all taken with the crystal perpendicular to the electron energy analyzer.

STM experiments were conducted in a Createc low-temperature STM instrument located at the Center for Functional Nanomaterials at Brookhaven National Laboratory. The base pressure in the STM chamber was lower than 5×10^{-11} Torr. The Au(111) crystal was cleaned by repeated cycles of Ar ion sputtering at 1 kV followed by annealing to 800 K. The clean Au(111) surface showed extended terraces with the characteristic $\left(22\times\sqrt{3}\right)$ herringbone reconstruction pattern. PDI adlayers were deposited in a preparation chamber that could be vacuum isolated from the STM instrument and made use of the same line-of-sight doser used for the TPD and 2PPE measurements. All STM images presented here were acquired at 80-95 K using a tungsten tip in constant current mode.

4.3. Experimental results

4.3.1. PDI binding and morphology on Au(111)

A combination of TPD and atomic imaging by STM were used to probe the coverage and temperature dependence of PDI binding interactions and surface structure. Figure 4.1a shows a series of TPD spectra for increasing exposure of PDI onto a Au(111) surface at 95 K. It was not possible to identify a single feature in these data with desorption from a saturated "monolayer." As shown in Figure 4.1b, however, the intensities of the two high-temperature peaks observed for surfaces prepared at 95 K and then annealed to 300 K were found to saturate at relatively low exposures of PDI. To establish a scale on which to measure coverages, we equate the integrated intensity of these two peaks to a coverage which we define as 1 ML; coverages for layers deposited at other exposures and temperatures are determined from the integrated intensity of their TPD spectra relative to this value. Hence, the calculated coverages in Figure 4.1a for surfaces dosed at 95 K are based on the total PDI desorption intensity relative to the residual

TPD intensity for surfaces annealed to 300 K (Figure 4.1b). Because it is independent of the sticking coefficient, this intensity normalization provides a much more precise means for

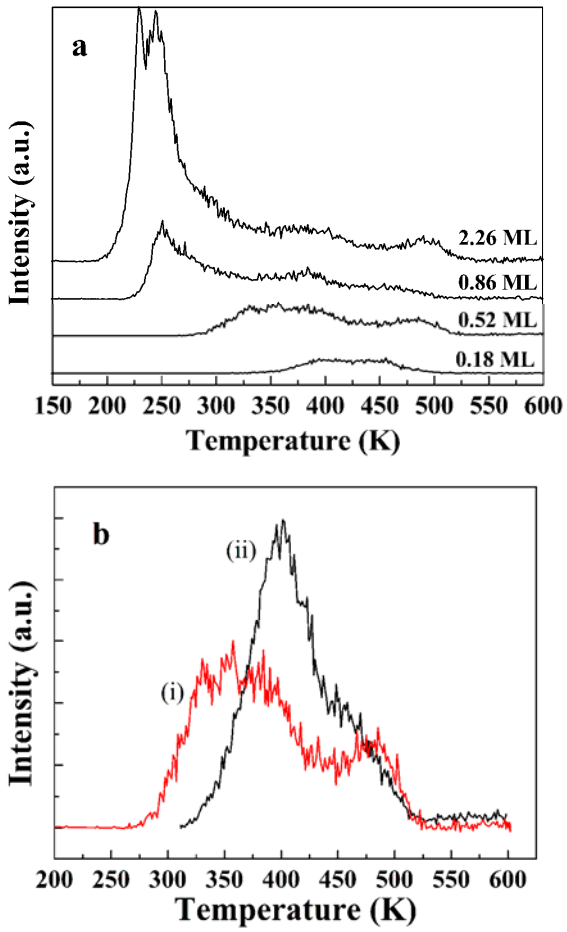

Figure 4.1: (a) TPD spectra for PDI adsorbed on Au(111) at 95 K. The baselines are offset for viewing clarity; (b) TPD spectra for PDI adsorbed on Au(111) (i) PDI dosed at 95 K and annealed to 300 K; (ii) saturated 1.0 ML PDI dosed at 300 K.

tracking the relative amount of PDI on the surface than does the exposure time.

At the lowest coverage studied here (0.18 ML), the TPD spectrum for PDI dosed at 95 K exhibits a broad desorption feature between ~325 K and ~500 K (see Figure 4.1a). As the coverage is increased (0.52 ML and 0.86 ML), this desorption band broadens to lower and higher temperatures, with the low temperature side building in intensity to a relatively sharp peak at 245 K. At even higher coverage (2.26 ML), the intensity of the desorption peak at 245 K continues to grow along with the appearance of second, low temperature peak at 230 K. The intensity of the 230 K peak does not saturate up to the highest exposure studied (equivalent to 4.35 ML) and is assigned to the desorption of weakly-bound PDI molecules. The latter most likely originate from physisorbed multilayers. The TPD spectra at intermediate coverage (0.52-2.26 ML) also suggest the presence of two broader features at 365 K and 480 K. The intensities of these features appear to be saturated in the TPD spectra for coverages ≥ 0.86 ML. Similar features are more clearly observed in the TPD spectra for PDI/Au(111) surfaces annealed to 300 K (Figure 4.1b).

Possible assignments of the features observed in the TPD spectra (Figure 4.1) are derived from STM images of surfaces dosed and held at 95 K (Figure 4.2a) and those dosed at 95 K and then briefly heated to 300 K (Figure 4.2b and 4.2c). In both cases, the PDI exposure was similar to that which resulted in the TPD spectrum at 0.86 ML in Figure 4.1, and the STM images were recorded at 80–95 K. As shown in Figure 4.2a, PDI molecules dosed and held at 95 K exhibit a wide range of surface morphologies that include three-dimensional (3-D) islands, short molecular chains and individual molecules bound at step edges. The latter are imaged as bright features whose lateral size is consistent with individual molecules. It is expected that the PDI molecules bound to coordinatively unsaturated Au atoms at the step edges would exhibit the

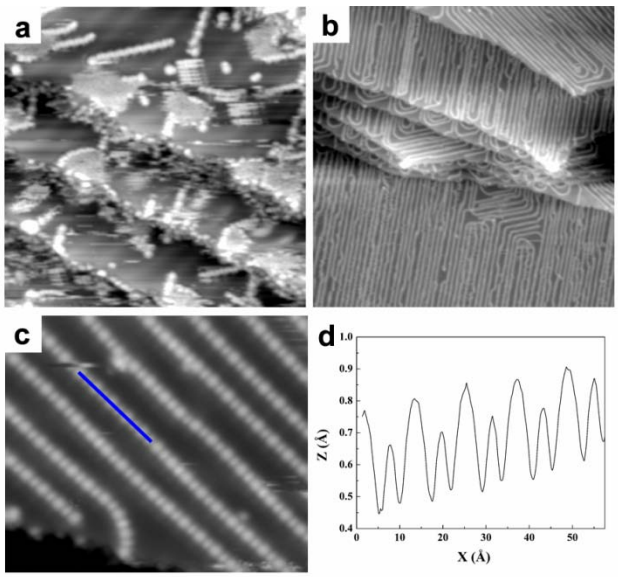

Figure 4.2: (a) STM image of PDI on Au(111) dosed at 95 K (35×35 nm; tunneling parameters: sample bias voltage (V_b) = -1.14 V; current set point (I_t) = 0.33 nA); (b-c) STM images of PDI on Au(111) dosed at 95 K and annealed to 300 K (V_b = -1.03 V; I_t = 0.17 nA; b: 140×140 nm; c: 17.5×14.8 nm); (d) profile of a molecular chain segment showing the repeating distance between basic units.

highest binding energy and lead to a high temperature TPD peak that saturates at low PDI exposures. Based on these considerations, we assign the TPD feature at 480–490 K in Figure 4.1 to desorption from step edges (and other defects).

On the terraces of Au(111) surfaces dosed and held at 95 K (see Figure 4.2a), we see two characteristic PDI morphologies corresponding to small 3-D islands and short molecular chains with a maximum length of ~10 nm. The terraces also exhibit bare regions where the Au(111) herringbone reconstruction is clearly visible. The apparent height of the islands is higher than that of the short molecular chains, which suggests the formation of a second layer of PDI molecules. Generally, it was not possible to obtain molecular resolution on the islands, likely because they are disordered 3-D structures and because weakly-bound PDI molecules may be displaced by the STM tip during scanning. Desorption of molecules from multilayer structures typically results in narrow desorption peaks whose intensities do not saturate with increasing dose. This describes the observed characteristics of the TPD peak at 230 K (see Figure 4.1a), and we therefore assign this TPD feature to desorption of PDI molecules from the top layers of the islands.

The second characteristic morphology observed immediately after dosing at 95 K is that of short molecular chains whose images consist of alternating large and small features. The lengths of the chains vary and some of the shorter chains are seen to move with the tip during the scan and appear as series of closely-spaced blurred features. We attribute the broad desorption band centered near 365 K in the TPD spectra (see Figure 4.1) to the desorption of PDI molecules resulting from the thermal breakup of these molecular chains. As discussed below, this assignment is consistent with TPD and STM images of the PDI/Au(111) surfaces annealed to 300 K (Figure 4.1b). Variations in desorption energy with chain length could contribute to the

broad width of the desorption feature. The binding morphology of PDI molecules responsible for the TPD peak at 245 K cannot be assigned with certainty, although they are likely to include the more strongly-bound PDI molecules in the first layer of the molecular islands. In summary then, we attribute the broad spectrum of the desorption yield extending from the peak at 245 K to the "defect" peak at 480 K as resulting from: (i) PDI molecules in direct contact with the Au surface that originate from the thermal breakup of small islands, at the low temperature end, (ii) the breakup and desorption of molecular chains in the 300–450 K range, and (iii) the desorption of molecules bound at step edges and other defects at the high temperature end.

Annealing to 300K results in a dramatic reorganization: long 1-D molecular chains form across the entire Au(111) surface as shown in Figure 4.2b. Molecules still occupy the step edges, but all of the 3-D islands and short chain structures have disappeared. It is immediately apparent from this observation that molecules in the long 1-D chains formed during annealing are more tightly bound to the surface than those comprising the 3-D islands, consistent with our earlier assertions that the low temperature TPD features at 230 K and 245 K for the surface dosed and held at 95 K (Figure 4.1) are associated with molecular islands and the TPD features near 365 K and 480 K are due to desorption from molecular chains and the step edges (and other defects), respectively. The majority of the chains are aligned along the $\langle 1\,\bar{1}0 \rangle$ (nearest-neighbor) directions of the Au(111) surface. The chains are largely straight, but exhibit 60° changes in direction, and kinks, as well as loops that allow the chains to remain continuous without crossing a step edge. Some of the molecular chains are more than 100 nm in length. The line profile shown in Figure 4.2d along one of the chains gives a repeat distance of 1.17 ± 0.02 nm which is the same as that found along the shorter chains observed immediately after deposition at 95 K. At the coverage shown in Figure 4.2b, the lateral distance between PDI chains is 2.15 ± 0.1 nm.

From the STM images, we estimate a coverage of 0.3 ML, which is in reasonable agreement with that obtained from TPD measurements.

4.3.2. Electronic Structure of PDI/Au(111) surfaces

To probe the electronic structure of the PDI/Au(111) surface, we used 2PPE and STS, both of which are sensitive to the density-of-states above and below the Fermi edge. STS has the advantage of probing single molecules, whereas 2PPE is capable of higher energy resolution, can be used to obtain accurate measurements of the work function, and allows for probing both unoccupied and occupied states relatively far (~4.5 eV) from E_F where field emission and electron-induced chemistry at the high applied biases required to probe these states with STS can be prohibitive. For 2PPE experiments of PDI on Au(111), we used both the 2nd harmonic ($h\nu$ = 3.00–3.20 eV) and the 3rd harmonic UV ($h\nu$ = 4.5–4.8 eV) generated with the time-plate doubler-tripler. The 2nd harmonic was used to investigate changes in the work function (Φ) because the 3rd harmonic photon energy exceeds the work function at high PDI coverages, and results in one-photon photoemission with very large yields at energies close to the secondary electron energy cutoff. The interfacial electronic structure was probed primarily with 3rd harmonic radiation because it provided access to a larger range of states by virtue of its relatively large two-photon energy ($2h\nu$ = 9–9.6 eV). In principle, unoccupied (occupied) states as far as ~4.5 eV above (below) E_F could be observed. STS measurements were taken at 95 K with a tip bias range of -1.5 to +1.5 V.

Figure 4.3a displays the 2PPE spectra of PDI on Au(111) with different coverages dosed and held at 95 K. These spectra were obtained using 2nd harmonic radiation with a photon energy of 3.02 eV (410 nm). The PDI binding configurations under these dosing conditions correspond

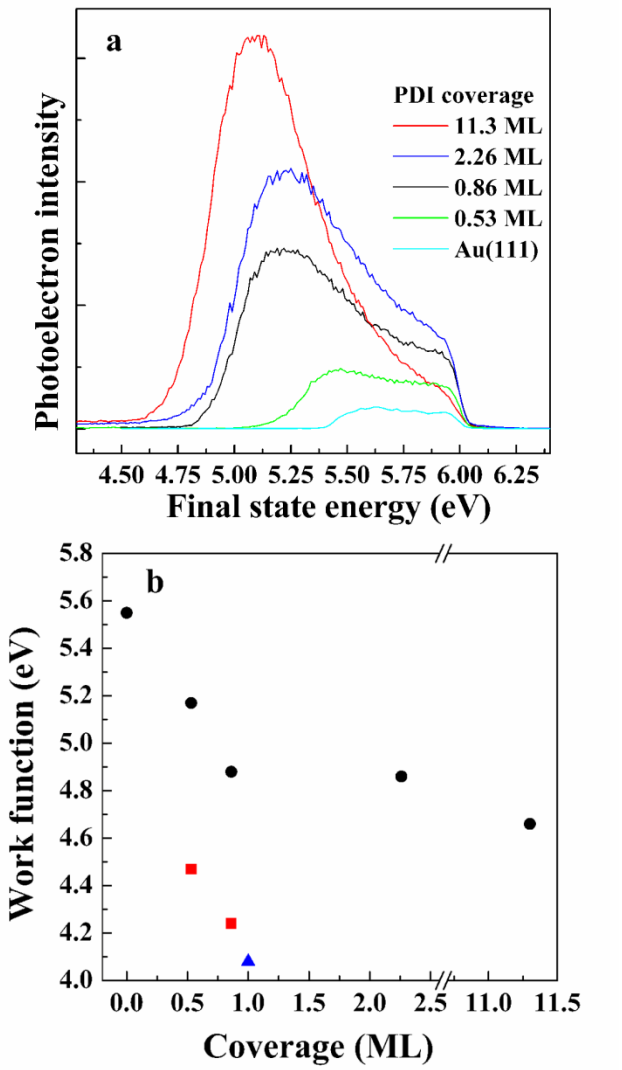

Figure 4.3: (a) One-color 2PPE spectra of PDI on Au(111) as a function of coverage. The photon energy is 3.02 eV; (b) The work function of PDI on Au(111) versus coverage; Circles: PDI on Au(111) dosed at 95 K; Squares: PDI dosed on Au(111) at 95 K and annealed to 300 K; Triangle: PDI on Au(111) dosed at 300 K.

to the TPD data in Figure 4.1a and the STM image in Figure 4.2a. The shift of the low energy photoemission threshold in 2PPE spectra indicates a decrease in work function with increasing PDI coverage. The work function, Φ, is determined from the 2PPE spectra by the expression

$$\Phi = 2h\nu - E_F + E_{cutoff}$$

where $h\nu$ is the photon energy, and E_F and E_{cutoff} are the observed energies for the onset of photoemission from the Fermi level and the cutoff of the secondary electrons at low final state energies, respectively. As seen in Figure 4.3b, the work function decreases monotonically over the whole coverage range out to 11.3 ML. The rate of decrease is greatest at coverages below 1 ML, above which Φ changes more slowly. Recent DFT calculations predicted that Φ would decrease relative to bare Au at low coverage (0.33 ML) and then increase at 1 ML due to a reversal in the surface dipoles.[107] A vertical PDI binding geometry was used in these calculations, which may only be appropriate for PDI species in the small islands or at step edges. As noted above, we do observe a significant change in the rate at which Φ decreases above 1 ML, however, this is also the point at which we begin to see evidence for the growth of 3-D islands in the TPD spectra (see Figure 4.1a). Thus, we see no evidence for the reversal of dipoles predicted by the DFT calculations. Similarly for a related system, 4-methylphenyl isocyanide (mPNC) on Au(111), there is no evidence for such a reversal. Rather, the work function for the mPNC multilayer is observed to be lower than that for 1 ML coverage.[117]

After annealing a surface with 0.53 ML PDI to 300 K, the work function drops dramatically from 5.17 eV to 4.47 eV (see Figure 4.3b). This change is not due to desorption of PDI molecules since the integrated intensity of the TPD spectrum is not changed by annealing at this coverage. At a higher coverage of 0.86 ML, annealing to 300 K results in the desorption of the more loosely-bound PDI molecules (Figure 4.1a), yet the work function still declines by 0.64

eV. This is surprising, because, all else being equal, the work function would be expected to increase back toward the clean-surface value as adsorbates are removed from the interface. For example, Sohn and White reported that annealing mPNC adlayers on Au(111) to 250 K removes physisorbed molecules and increases Φ by 0.8 eV.[117] In general, changes in Φ are proportional to the number of adsorbates and their dipole moments at interface.[117,118] For mPNC on Au(111), the loss of physisorbed molecules after annealing decreases the total surface dipole and consequently leads to an increase in the work function. In the present case, we attribute the rapid decrease of Φ after annealing to 300 K to the reorganization of PDI molecules into the 1-D chains shown in Figure 4.2b and 4.2c. In this ordered structure, more PDI molecules are in direct contact with the Au surface and apparently induce a larger surface dipole and therefore a larger decrease in work function. The result is also consistent with a thermally-induced change in the PDI binding to the gold surface that acts to increase the surface dipole (as will be considered further in the Discussion). Previous STM experiments on CH_3NC on Pt(111) surface suggested a similar reorganization with thermal treatment.[119] Specifically, at low coverage the CH_3NC molecules tend to form pairs when dosed at 50 K and distribute more uniformly after annealing to 150 K. For PDI deposited at 300 K, the work function is a minimum of 4.1 eV for a saturated monolayer, which is similar to that found for fully saturated monolayers of mPNC (Φ = 4.0 eV)[117] and 4,4'-ethyneylphenyl-1-benzyl isocyanide (Φ = 4.1 eV) on Au(111).[120] Both mPNC and 4,4'-ethyneylphenyl-1-benzyl isocyanide are dipolar molecules with only one isocyanide linkage to Au so that increases in coverage should increase the number of surface dipoles and cause Φ to drop significantly. A comparable change in Φ also occurs for the 1-D PDI chains at higher coverage, but here the nature of the surface polarization is quite different and includes both molecular and Au-adatom contributions.

The 2PPE spectra taken with 3rd harmonic radiation (4.65 eV) shown in Figure 4.4 provide more specific information on the electronic states of the PDI/Au(111) system. Figure 4.4a shows 2PPE spectra dosed and held at 95 K as a function of PDI coverage. The prominent peak near E_F in the bare Au(111) spectrum corresponds to the well-known surface state.[67,72] As PDI molecules are added to the surface at 95 K, the peak intensity of the surface state decreases and the peak is no longer discernible at a coverage of 0.86 ML. At the same time, a band of emission ranging from ~8.0 to 8.75 eV and weakly-peaked at a final state energy of 8.21 eV grows in. This feature has an apparent maximum intensity around 1 ML. At the highest coverage (2.26 ML), the intensity of this feature appears to decrease relative to the background photoemission. Spectra (i) and (ii) in Figure 4.4b show the effects of annealing the 2.26 ML sample dosed at 95 K. After annealing to 300 K, the peak at 8.21 eV becomes considerably stronger and more distinct from the background photoemission. In addition, annealing the surface also leads to the emergence of a small peak at 7.83 eV. Because both of these 2PPE features become distinct after annealing, they are clearly associated with the 1-D molecular chains in direct contact with the Au(111) surface. To explore this assignment further, we dosed 0.86 ML PDI onto the Au(111) surface at 95K that had been pre-dosed with 1 ML of *n*-heptane. The resulting 2PPE spectrum is given in Figure 4.4b(iii). The *n*-heptane adlayer was prepared by saturation dosing at a surface temperature of 165 K. The coverage of 1 ML was verified by TPD experiments and comparison with previous studies.[121] With *n*-heptane acting as a spacer layer between the PDI molecules and Au(111) surface, the feature at 8.21 eV is no longer observable (compare to 0.86 ML spectrum in Figure 4.4a). This result shows that the peak at 8.21 eV originates from an state due to a direct PDI–Au contact. Because 8.21 eV peak is attenuated at a coverage of 2.26 ML, these results also indicate that PDI molecules physisorbed in multilayer

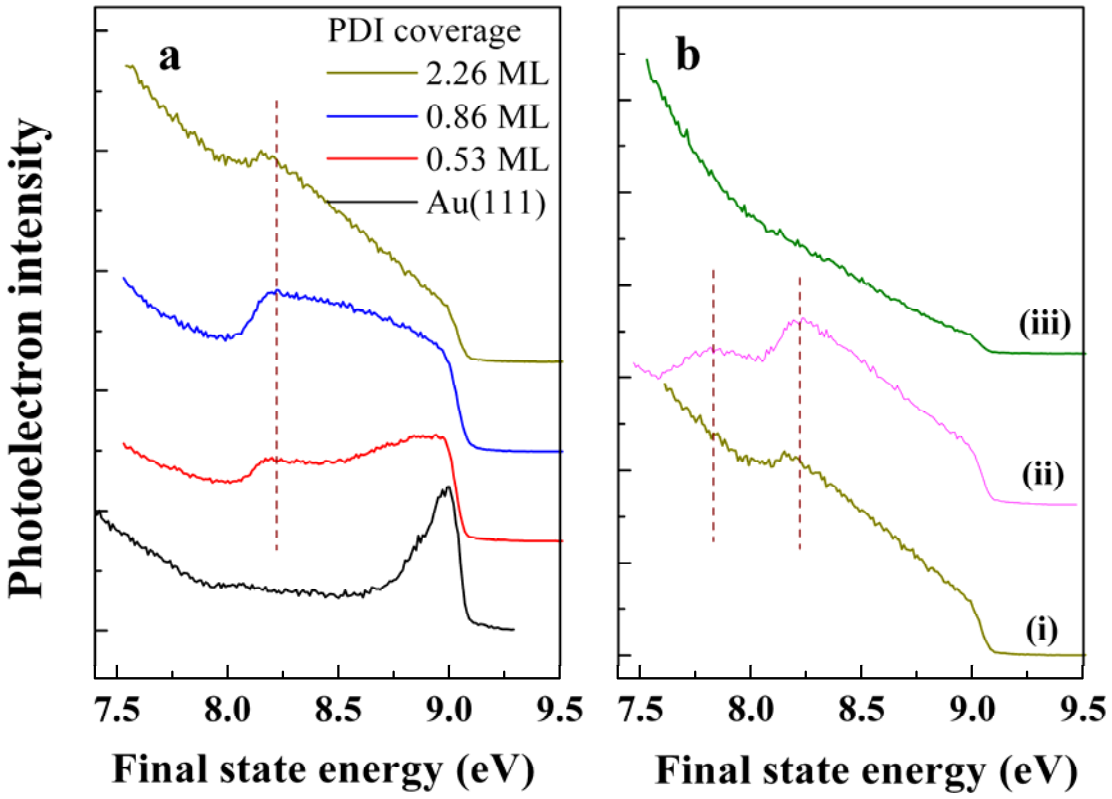

Figure 4.4: The high final state energy region of one-color 2PPE spectra of PDI dosed on Au(111) at 95 K. The photon energy is 4.54 eV; (a) 2PPE spectra at different PDI coverage; (b) 2PPE spectra for different PDI dose conditions: (i) 2.26 ML; (ii) 2.26 ML after annealing to 300 K; (iii) 0.86 ML dosed on 1.0 ML *n*-heptane covered Au(111).

islands are not in close contact with the Au surface and do not contribute to the interfacial state. Rather, multilayer molecules scatter electrons emitted from the PDI–Au interface state, preventing them from being detected.

To discern whether the two 2PPE peaks shown in Figure 4.4b(ii) originate from an occupied or unoccupied state, we have measured the dependence of the photoelectron kinetic energy on photon energy. These measurements were performed on a 0.86 ML PDI/Au(111) surface prepared at 95 K and then annealed to 300 K. The 2PPE spectra before and after annealing are shown in Figure 4.5a. As shown in Figure 4.5b, the slope of the final state energy shift for the peak at 8.21 eV is equal to 1.85 ± 0.10 indicating that this peak originates from an *occupied* state with a binding energy of 0.88 eV below E_F. On the other hand, the peak at 7.83 eV exhibits a slope of 1.10 ± 0.15 and, therefore, corresponds to an *unoccupied* initial state located at 3.32 eV above E_F. Since both 2PPE peaks are most prominent after annealing to 300 K, these initial states are associated with interfacial states of the 1-D PDI molecular chains.

The 2PPE results can also be compared to STS (or dI/dV) experiments conducted on the molecular chains after annealing to 300 K (see Figure 4.6). The STS spectra were found to vary slightly between the "large" and "small" features in the molecular chains (see Figure 4.2c), and these differences are currently under investigation. For comparisons with the surface-averaged 2PPE spectra, the STS spectrum shown in Figure 4.6 represents an average of many STS scans at different points along several different chains. At negative bias, the STS spectrum exhibits a prominent feature centered at about -1 V which we associate with the occupied state observed at 0.88 eV below E_F in the 2PPE spectra for the annealed surfaces (see Figure 4.5a). At positive bias, the STS spectrum is featureless, which suggests that no additional unoccupied state is formed up to +1.5 eV above E_F. Unfortunately, the unoccupied electronic state at +3.32 eV

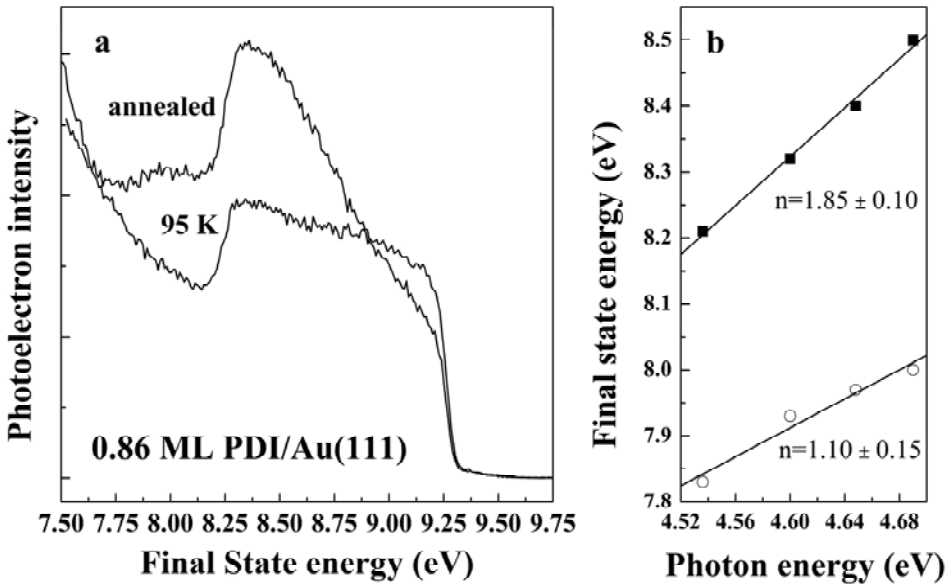

Figure 4.5: (a) The high final state energy region of one-color 2PPE spectra of 0.86 ML PDI dosed on Au(111) at 95 K before and after annealing at 300 K. The photon energy is 4.65 eV; (b) dependence of the peak positions (solid square for the occupied state and open circle for the unoccupied state) as a function of photon energy for 0.86 ML PDI on Au(111). The solid lines are the results of linear regression fits with slopes of 1.85 ± 0.10 (occupied state) and 1.10 ± 0.15 (unoccupied state), respectively.

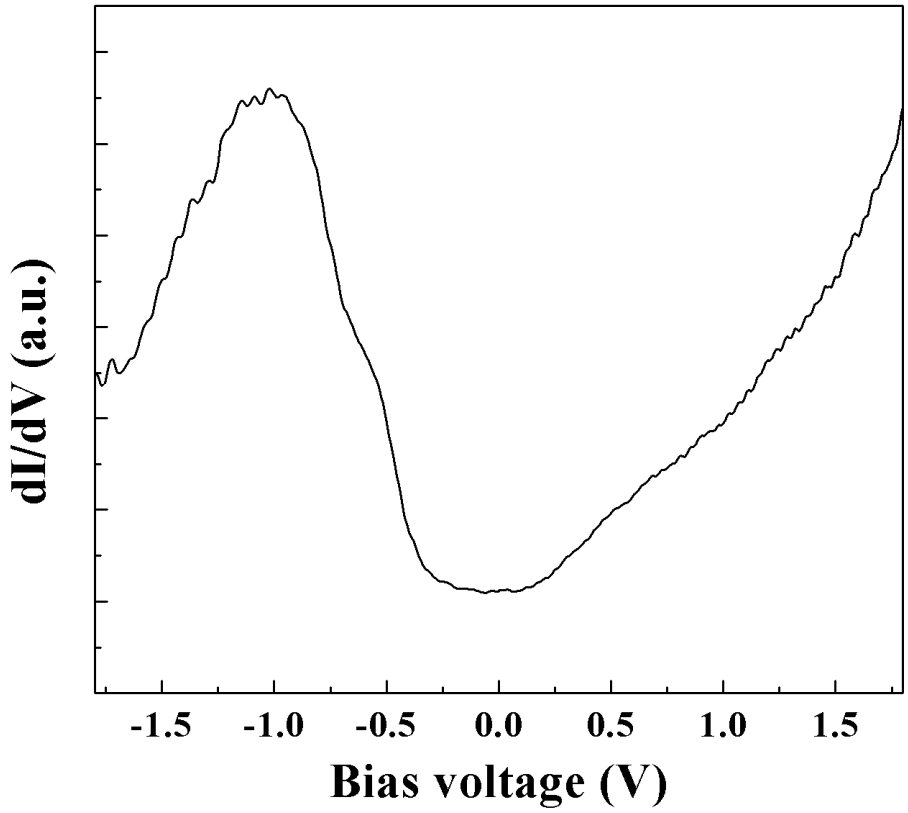

Figure 4.6: *dI/dV* spectrum of a 1-D PDI chain formed after annealing at 300 K. The spectra were measured after recooling to 80~90 K and many measurements taken at randomly selected spatial locations on the 1-D molecular chain were averaged to obtain the curves.

above E_F observed in 2PPE was inaccessible because at high positive bias the tunneling current became unstable as a result of field emission.

4.4. Discussion

4.4.1 PDI binding and morphology on Au(111)

The long 1-D chains observed in the STM image in Figures 4.2b and 4.2c are similar to those recently reported by Boscoboinik et al., for PDI deposited and imaged at 300 K on a Au(111) at very low coverage (~ 0.004 ML).[115] In their STM images, long, 1-D chains were observed oriented along the $\langle 1\,\bar{1}0 \rangle$ directions of the Au(111) surface with a monomer repeat distance of 1.13 ± 0.3 nm. Based on various models for PDI intermolecular bonding, Boscoboinik et al., concluded that the bonding morphology most consistent with the STM observations involves PDI molecules lying flat on the surface and interconnected via isocyanide bonds to Au adatoms, i.e., $[–Au–PDI–]_n$ oligomer chains. Although the coverage of PDI in our experiments is 100× greater than in the work of Boscoboinik et al., the 1-D PDI chains observed here have the same morphology, orientation and monomer repeat distance. Moreover, the maximum height from Figure 4.2d is only 0.2 nm which is consistent with PDI molecules lying parallel to the surface. Hence, based on the assignment made by Boscoboinik et al., we attribute the 1-D structures in Figure 4.2b and 4.2c to $[–Au–PDI–]_n$ molecular chains. This assignment clarifies the role of annealing the PDI/Au(111) surface to 300 K, since thermal energy is needed to give PDI molecules mobility and assist in lifting Au adatoms from the surface. One of the interesting aspects of the present work is that the Au(111) herringbone reconstruction remains mostly intact even though a substantial number of Au adatoms are required to build the $[–Au–PDI–]_n$ chains shown in Figure 4.2b and 4.2c, i.e., the number of Au atoms displaced must be

equal to the number of PDI molecules adsorbed in the chains. A more detailed STM study of the initial growth, and coverage and temperature dependence of PDI adlayers on Au(111) is currently underway.

In contrast to the PDI chains formed by vapor deposition, PDI SAMs formed on Au(111) from solution are thought to be composed of molecules with their long axes aligned roughly perpendicular to the surface plane.[112-114,122,123] Support for upright binding in the PDI SAMs is based on IR vibrational spectroscopy which indicated the presence of two chemically inequivalent isocyanide groups, one bound to the Au surface and one unbound free end. These results would suggest that the favored geometry for PDI binding changes from lying down in the 1-D molecular chains at low coverage typical of this work to a more vertical packing at the high coverage of a SAM. Such behavior has been found for 1,6-diisocyanohexane binding on Au(111) for which both isocyanide groups bind to the Au surface at low coverage, whereas the molecules stand up with one free isocyanide group at higher coverage.[124] In our experiments, the packing density of the PDI film formed by vapor deposition is expected to be smaller than that in solution-grown SAMs. Previous experiments report an intermolecular distance of 4–5 Å in thiophene SAMs on Au(111).[66,92] By contrast, the distance is 6–9 Å for a vapor-saturated thiophene monolayer on Au(111).[116] Boscoboinik et, al. proposed that at high coverage, additional PDI molecules could bind vertically to the Au adatoms within the molecular chains and thereby give rise to both bound and free isocyanide groups.[115] The STM images in Figure 4.2b and 4.2c were taken at much higher coverage (~0.3 ML) than in the earlier study of Boscoboinik et al., (~0.004 ML), however, no height variations consistent with vertically aligned PDI molecules were observed in STM topography scans along the chains (see Figure 4.2d). It is likely that differences in deposition conditions, i.e., vapor deposition in vacuum versus

deposition from solution in the presence of solvent molecules, play an important role in determining the lowest energy bonding configuration of PDI on the Au(111) surface.

The bonding of PDI molecules to two Au adatoms with low coordination is expected to be stronger than in a vertical configuration involving a single Au–CN bond. Hence, it is reasonable to suggest that the thermal breakup of the $[–Au–PDI–]_n$ chains followed by desorption of the PDI molecules would be reflected in a higher desorption temperature. Assuming first order desorption, the desorption energy of PDI from the 1-D chains can be estimated from the desorption peak at 365 K (see Figure 4.1). Using the Redhead expression[42] and a preexponential factor of 10^{13} s^{-1}, we obtain a PDI desorption energy of 1.00 eV (96.1 kJ/mol). This is somewhat higher than that calculated in a recent DFT study which reported a binding energy of 0.71 eV for PDI vertically bound at an atop Au site (fcc; 0.33 ML coverage).[107] Our derived desorption energy, however, is similar to that reported for PDI from Pd(111), 1.17 eV,[113] and desorption of 4-methylphenyl isocyanide (mPNC) from Au(111) and Cu(111), i.e., 1.02 eV and 0.98 eV, respectively.[117] The surface binding of PDI on Pd(111) or mPNC on Au(111) and Cu(111) has not been examined by STM, but all three cases exhibit coverage dependent TPD spectra that are very similar to that observed in this work for PDI on Au(111) (see Figure 4.1).[113,117] Vibrational spectra for PDI on Pd(111) showed evidence for bound and free isocyanide groups and at least two different binding sites (σ/π-type and σ-type) consistent with vertically aligned PDI molecules. The observation of only vertically aligned PDI molecules on Pd(111) may be a consequence of stronger π-back bonding which favors a perpendicular configuration. It should be noted, however, that the same IR study of PDI/Pd(111) also included a comparison with PDI/Au(111) and concluded that PDI on the Au(111) surface was also bonded via only one isocyanide group.[113] For mPNC on Au(111), a combination of

TPD and XPS were used to identify two different binding sites that were attributed to vertically bonded mPNC molecules at atop sites (β_1) and mPNC molecules in a slightly bent geometry resulting from increased sp^2 hybridization at 3-fold hollow sites (β_2).[117] DFT calculations for phenyl isocyanide on a Au_{14} single layer slab showed that the most favorable adsorption structure has the isocyanide moiety bound at the 3-fold hollow site and the molecular axes tilted by 27° from the surface normal.[125] The fact that the PDI desorption energy from the [–Au–PDI–]$_n$ structure is similar to other isocyanide-metal single bonds, may indicate that the PDI molecules preferentially desorb from the ends of the chains where they are tethered by only one Au-CN bond. Moreover, it is possible that all of these isocyanide-metal systems involve bonding to adatoms, as adatom formation on Au(111) and Cu(111) surfaces is facile at room temperature with the help of adsorbed molecules.[126,127] Adatom binding has also been implicated as a key structural component in the binding of thiol molecules to Au surfaces[128] where the reconstructed surface acts as a source of adatoms and where the S–Au and isocyanide–Au bond strengths are similar.

4.4.2. Electronic Structure of PDI/Au(111) surfaces

Since the isocyanide group is isoelectronic with CO, bonding interactions of isocyanides on metal surfaces have been described by the Blyholder model for CO–metal interactions involving synergistic 5σ lone-pair donation and $2\pi^*$ back-donation.[129,130] As both orbitals have anti-bonding character, 5σ charge donation to the surface strengthens the C–O bond whereas back-donation from the metal to the $2\pi^*$ orbital weakens the C–O bond. Previous studies of Au-bonded isocyanide groups using infrared and surface-enhanced Raman experiments show a ~60–70 cm^{-1} blue shift in the C–N stretching frequency compared to "free" CN groups, suggesting

that σ charge donation is the dominant contribution to bonding.[131] In the case of mPNC on Au(111), XPS chemical shifts for the N atom also support the conclusion that the bond between the isocyanide group and the Au surface is of predominantly σ character. In addition, the insensitivity of the C–N stretch frequency to the nature of the group attached to the isocyanide group, e.g., aromatic ring or alkane chain, indicates that charge transfer is mainly determined by the isocyanide-metal interaction.[112-114]

In this work, charge transfer at the isocyanide–Au interface was probed by 2PPE measurements of the work function relative to that of the bare Au surface (see Figure 4.3b). In general, adsorbate charge transfer results in an interface dipole that modifies the work function relative to the bare surface, i.e.,

$$\Delta\Phi = (n \times e \times \mu)/\varepsilon_0$$

where μ is dipole moment at interface, n is the adsorbate density, e is the electronic charge and ε_0 is the vacuum permittivity.[117,118] For mPNC on Au(111) at 1 ML, the measured work function change ($\Delta\Phi$ = -1.3 eV) was used to calculate a surface dipole of +1.45 D, compared to ~ 4 D for the isolated molecule in the gas phase. The difference was attributed to the charge transfer at the mPNC–Au interface. We observe a similar work function change ($\Delta\Phi$ = -1.45 eV) for PDI/Au(111) surfaces (~ 1 ML) that were annealed or dosed at 300 K (see Figure 4.4b). This decrease in work function can be ascribed to a net charge transfer from the $[–Au–PDI–]_n$ chains to the Au surface. Using the above expression and the experimental work function change ($\Delta\Phi$ = -1.45 eV) for a saturated PDI monolayer on the Au(111) surface, we calculate an interface dipole moment of +1.0 D per [–Au–PDI–] monomer unit. Within the 1-D chains, the –N≡C groups of the PDI molecules are expected to donate electron density to the coordinatively unsaturated Au adatoms which have been lifted out from the surface, leaving some of their

electron density behind. This leads to a net increase in electron density on the Au surface and a decrease in the work function.

Insight into the origin of the occupied and unoccupied states observed in the 2PPE spectra of PDI/Au(111) (Figures 4.4 and 4.5) can be gained from recent DFT studies of isocyanide molecules bound to the Au(111) surface.[107] According to these calculations, the σ-HOMO state of the unbound PDI molecule is located ~3 eV below the Fermi level. Interactions (hybridization) with the Au $5d_{z^2}$ and 6s orbitals result in a resonance state around 0.8–1.2 eV below the Fermi level, consistent with the binding energy of the occupied state (0.87 eV) observed in our 2PPE spectra. Evidence for this state resulting from PDI–Au interactions comes from the experiments summarized in Figure 4.5b, where the corresponding 2PPE peak can be removed or attenuated by using a 1 ML spacer layer of *n*-heptane or by the formation of PDI multilayers at 95 K, respectively. From molecular conductance experiments on PDI/Au(111) SAMs, a peak at 0.38 ± 0.1 eV below the Fermi level was assigned to the HOMO of PDI which is ~0.5 eV higher than our 2PPE result.[105] This difference may reflect the high packing density of the PDI SAM, as theoretical calculations indicate a weak but finite screening within a SAM which reduces the gap between HOMO and the Fermi level.[107] A similar discrepancy between conductance and photoemission measurements was found for the related system, BPDI on Au(111). In this case, the HOMO level was determined to be 0.53 ± 0.1 eV below E_F by molecular conductance spectroscopy,[105] whereas photoemission studies placed the HOMO level at more than 5 eV below the E_F.[106]

For the unoccupied states above E_F, DFT calculations based on the generalized gradient approximation (GGA) predict that the LUMO and LUMO+1 states of PDI are located at 0.7 eV and 3 eV above E_F, respectively, for a PDI coverage of 0.33 ML.[107] An analysis of the projected

density of states also shows that the LUMO and LUMO+1 levels involve π-type interactions, with the LUMO state being delocalized over the entire molecule.[107] However, DFT calculations using GGA approximation tend to overestimate the shift of the unoccupied levels. To compensate, Li et al., employed GW many-body perturbation theory to estimate that the LUMO-like states shift upward by 1.5~2 eV compared to the DFT results.[110] This places the calculated energy (~2.2–2.7 eV) of the LUMO level into the same energy range as the unoccupied state observed in 2PPE spectra at 3.32 eV above E_F. Hence, we assign this unoccupied level to a π-state with mostly PDI character as found in both the DFT and GW corrected calculations.

Annealing PDI/Au(111) surfaces prepared at 95 K to 300 K results in a considerable change in electronic properties which is clearly related to the formation of the 1-D chains. At 95 K, the growth of PDI adlayers on Au(111) follows a Volmer-Weber mode in which 3-D islands begin to form before completion of a uniform monolayer (Figure 4.2a). After annealing, the chemisorbed and physisorbed structures reorganize into 1-D chains resulting in an increase in the number of PDI molecules interacting directly with the Au surface (see Figures 4.2b and 4.2c) and a concomitant increasing polarization of the interface. As a consequence, the 2PPE peak intensity assigned to the interfacial occupied state increases and the work function decreases. The unoccupied state is also clearly associated with the ordered PDI structures as it is only discernable in 2PPE spectra after annealing. Figure 4.7 provides an overall summary of the electronic structure information obtained from 2PPE and STS measurements of PDI/Au(111) surfaces annealed at room temperature. A more complete analysis of the electronic structure of the 1-D $[–Au–PDI–]_n$ molecular chains on Au(111) using DFT calculations is currently in progress.

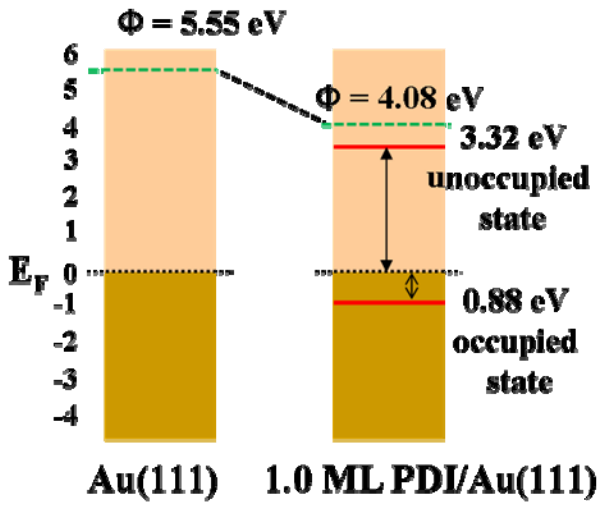

Figure 4.7: Energy level diagrams for clean Au(111) and Au(111) with 1.0 ML of adsorbed PDI. The 1.0 ML PDI was prepared by dosing at 95 K followed by annealing to 300 K.

4.5. Summary

The adsorption structures and electronic properties of 1,4-phenylene diisocyanide adlayers on Au(111) have been investigated with temperature programmed desorption, two-photon photoemission spectroscopy and scanning tunneling microscopy and spectroscopy. Thermal desorption studies versus exposure at 95 K STM show evidence of a wide range of binding sites, including physisorbed multilayers at 230 K and first-layer structures with desorption temperatures that range from 245–450 K. STM images for PDI/Au(111) surfaces dosed and held at 95 K show small disordered 3-D islands and short 1-D chain structures on the terraces, as well molecules bound to step edges. Annealing to 300 K removes the physisorbed molecules, and STM images show that the remaining PDI molecules are adsorbed at step edges or arranged in long, 1-D structures which cover the Au(111) terraces. STM topography measurements show that the 1-D chains are composed of alternating small and large features, whose spacing and height are consistent with a recently proposed model[115] in which chains of PDI molecules are held together by Au adatoms released from the surface.

For deposition at 95 K, the work function as measured by 2PPE decreases rapidly with increasing coverage consistent with an increase in the number of surface dipoles. An occupied interfacial electronic state with a binding energy of 0.87 eV below E_F was observed in 2PPE spectra for PDI dosed at 95 K. Based on previous studies of PDI on Au and other metals, we assign this state as due to σ-type interactions involving charge transfer from the –CN group to the Au surface.[111-113,117] Annealing the PDI/Au(111) to 300 K induces a large change in the work function, even at low coverage, which is attributed to a dramatic increase in the number of PDI molecules interacting strongly with the Au surface as a result of molecular rearrangement into 1-D chains. An *unoccupied* state, located 3.32 eV above E_F, is also observed for annealed surfaces.

The relatively large LUMO–E_F energy gap derived from 2PPE and STS measurements suggests that the PDI/Au system has a relatively high barrier for electron transmission. Further studies of the structure and electronic properties of the unusual 1-D PDI chains is currently underway using low temperature (5 K) STM and periodic DFT calculations.

Chapter 5. Self-assembled one-dimensional molecular chains of aromatic isocyanides on Au(111)

This section is to be published.

5.1. Introduction

With adsorbed organic molecules on a surface spontaneously assembling into densely packed and well-ordered structures, self-assembled monolayers (SAMs) provide a convenient, flexible way to modify the surface properties of metals and have been proposed for a number of applications.[132] Organic thiols on gold are the most widely used and investigated model systems for self-assembly. The high affinity of thiols to bind to the Au surface drives the formation of ordered overlayers with relatively high stability.[101,133] In addition, the terminal groups can be chemically modified to tune the physical and chemical properties of the SAMs for different studies such as molecular electronic devices[2] and passivation of nanoparticles.[101,132] However, susceptibility to oxidation[102,103] and a high electron transfer barrier at the interface[15] have limited their application in molecular electronics and motivated the search for new molecular junctions. Aromatic isocyanides have attracted widespread interest for this application as the N≡C triple bond is expected to effectively connect pπ orbitals of the aromatic moiety with dπ orbitals of the gold surface. These qualitative expectations are supported by recent conductance measurements[18] and theoretical calculations[19] which indicate that molecules bound to Au with terminal isocyanide groups exhibit higher conductance compared to the same molecule with a terminal thiol group. Despite these promising results, the electronic structures of adsorbed aromatic isocyanides on gold surface are lacking, as well as detailed information on surface bonding morphology. The later has been demonstrated to affect the interfacial electronic

properties by our photoemission experiments as described in Chapter 4. In order to carry out further studies of aromatic isocyanides molecules for molecular electronics applications, it is crucial to obtain the geometric and electronic information.

Previous studies of aromatic isocyanide SAMs formed on a Au(111) surface from solutions demonstrated that the isocyanide molecules bind to the Au surface through a single σ–type Au–C bond with a vertical geometry.[111-114,122,123] Support for an upright bonding geometry is based on infrared spectroscopy and sum frequency generation measurements which exhibited the presence of two N≡C stretching frequencies corresponding to a free –N≡C group and one shifted to higher frequency which was assigned to –N≡C group bonded on Au. By contrast, recent scanning tunneling microscope (STM) experiments showed that 1,4-phenyldiisocyanide (PDI) deposited from vapor on Au(111) surface formed one-dimensional, molecular chain structure at very low coverage (~0.004 ML).[115] The proposed adsorption model for this molecular chain includes alternating PDI molecules and Au adatoms, i.e., [–Au–PDI–] monomer unit. Specifically, the PDI molecules lie flat on the surface and are bonded at each end to Au adatoms which are pulled from the surface by the strong Au-isocyanide interaction. In our previous STM experiments described in Chapter 4, similar one-dimensional (1-D) chain structures were observed for PDI/Au(111) surfaces prepared at low temperature (<100 K) that were subsequently annealed to room temperature. The coverage, 0.3 ML, is much higher than that in Ref. [115], but is still expected to be smaller than that in solution-grown SAMs. With increasing coverage, the binding geometry may change from lying down to a more vertical packing. For the case of 1,6-diisocyanohexane binding on a Au surface it has been found that both isocyanide groups bind to the surface at low coverage, whereas the molecules stand up with one free isocyanide group at higher coverage.[124]

The Au herringbone reconstruction has been regarded as the source of Au adatoms upon adsorption of thiolate and chlorine molecules.[128,134] At low coverage, it can provide enough adatoms for $[–Au–PDI–]_n$ structure. However, the total number of Au adatoms provided from the reconstruction is limited, only 0.04 ML.[135] For PDI/Au(111) at high coverage, the adsorption model for the molecular chain structure needs to be reevaluated considering the large amount of Au adatoms required for the $[–Au–PDI–]_n$ molecular chains. It is important to understand the adsorption structures at different coverages, especially at high coverage in terms of potential application of isocyanide SAMs. Moreover, photoemission experiments on PDI/Au(111) showed an unusually large drop in the work function and the appearance of an unoccupied state at 3.3 eV above the Fermi level accompanying the formation of the molecular chain structure. (Chapter 4) To fully understand the unique electronic properties and how they are related with the molecular adsorption structure is essential for optimizing the performance of isocyanide-Au system for potential molecular electronics applications.

In this work, we have combined the low temperature STM measurements and first principle calculations to explore the bonding morphology and electronic structure of two aromatic isocyanides, PDI and 4,4'-biphenyldiisocyanide (BPDI), deposited on a Au(111) surface. PDI and BPDI molecules have the same diisocyanide terminal group. STM images showed that both PDI and BPDI molecules form similar one-dimensional molecular chains on the Au(111) surface with different repeating monomer distances due to the different molecular lengths. These experiments confirm that the diisocyanide molecules lie flat on the surface and provide strong support for the formation of molecular chains involving Au adatoms. In addition, STM experiments of PDI adsorption layer on Au(111) surface at high coverage indicate that the $[–Au–PDI–]_n$ molecular chains retain their structure up to a full monolayer. Scanning tunneling

spectroscopy (STS) measurements provide a probe of the local density of states of the PDI/Au(111) and BPDI/Au(111) including the observation of an electronic state localized on the molecular chain. Density functional theory (DFT) calculations support the favorable energetics for Au adatom formation and isocyanide-Au_{ad} bonding. The calculations also reveal a dipole moment at the interface between the isocyanide molecules and the Au surface that results from the formation of the molecular chain structure. This interfacial dipole moment was found to be responsible for the large work function change observed in the photoemission experiments. (Chapter 4)

5.2. Experimental and theoretical methods

STM experiments were conducted in a Createc low-temperature STM instrument at the Center for Functional Nanomaterials at Brookhaven National Laboratory. The base pressure in the STM chamber was typically lower than 5×10^{-11} Torr. The sample was cleaned and the adsorption layer deposited in a separate preparation chamber with a base pressure lower than 1×10^{-9} Torr. The Au(111) crystal was cleaned by repeated cycles of Ar ion sputtering at 1 kV followed by annealing to 800 K. The clean Au(111) surface showed extended terraces with the characteristic $\left(22\times\sqrt{3}\right)$ herringbone reconstruction pattern.[136] Because both PDI and BPDI molecules have very low vapor pressure ($<10^{-4}$ Torr), the glass sample reservoir is directly connected to a line-of-site dosing tube via a gate valve. When dosing the diisocyanide molecules, the Au(111) surface was exposed to the tube directly with a distance of around 3~4 inches. PDI and BPDI samples were kept at 300 K and ~350 K, respectively. No decomposition products of PDI and BPDI molecules were observed either in residual gas analyzer during dosing or in STM images of the Au surface using these dosing conditions. For annealing the PDI/Au(111) sample,

the STM sample holder is resistively heated to 300 K, then cooled by liquid nitrogen or liquid helium for STM experiments.

All STM images presented here were acquired at 95 K or 5 K using a tungsten tip in constant current mode. The tip was prepared by a direct-current (dc) dropoff electrochemical etching method.[137,138] The tips are prepared in a beaker containing an electrolyte, in this case, 3M KOH. A piece of W wire (0.015 inch in diameter), mounted on a micrometer, was placed at the center of the beaker and acts as the anode. The cathode is a cylindrical surface made of stainless steel in the beaker. When a positive voltage, 8 V is applied to the wire, etching occurs at the air-electrolyte interface. The etching current suddenly drops when the lower part of the wire in electrolyte solution drops off. The dc dropoff circuit can sense the current drop and turn off the power supply to assure a sharp tip. The current imaging tunneling spectroscopy (CITS) experiments were conducted at 5 K to ensure there is no discernible drift occurred during the acquisition of *I–V* curves. In CITS experiments, topographic images in the constant current mode were recorded simultaneously with *I–V* curves and the feedback loop was disabled during spectroscopic acquisition. The STM image and tunneling spectroscopy analysis were carried out using software GXSM.[139,140]

DFT calculations were carried out by Dr. Yan Li in Computational Science Center at Brookhaven National Laboratory. The Quantum ESPRESSO package was used[141] with a plane-wave basis set, GGA/PBE[142] exchange-correlation functionals and norm-conserving pseudopotentials. The unreconstructed Au(111) surface was modeled by a 4-layer slab at the experimental bulk equilibrium lattice constant (4.16 Å).[107] A vacuum space of at least 10 Å was inserted between periodically repeated slabs to avoid spurious interactions between replicas. During structure optimization, the bottom Au layer was kept fixed while the top three Au layers

and the adsorbed molecules were fully relaxed till the maximum force is smaller than 0.026 eV/Å. Dipole corrections were applied along the direction of the surface normal by adding a saw-like potential against the surface potential shift which is caused by the interfacial dipole moment. The work function shift $\Delta\varphi$ was obtained through the Helmholtz equation $\Delta\varphi = -4\pi\mu_z/A_0$, where μ_z is the normal component of the surface dipole moment associated with the unit cell, which has a surface area A_0.

For PDI-Au chains on Au(111), a rectangular ($4 \times 2\sqrt{3}$) unit cell was used, containing a total of 64 Au atoms in the slab. Both full coverage (two PDI-Au chains per unit cell) and half coverage (one PDI-Au chain per unit cell) were studied. All Au adatoms are located along the $\langle 1\bar{1}0 \rangle$ direction, corresponding to a periodicity of $L_0 = 4\ d_{NN}$, where $d_{NN} = 2.9$ Å is the nearest Au-Au distance. A ($4 \times 4 \times 1$) Monkorst-Pack[143] *k*-point grids was employed to sample the first Brillouin zone and a four times denser grid was used to plot the projected density of states (PDOS).

For BPDI-Au chains on Au(111), two slightly different chain configurations were considered. In the first configuration, a ($\sqrt{31} \times 2\sqrt{3}$) unit cell was used, with the two surface lattice vectors along $[6\bar{5}\bar{1}]$ and $[10\bar{1}]$ directions, respectively. The chains run straight with all Au adatoms located at the *fcc* sites, corresponding to a periodicity of $L_0 = \sqrt{31}\ d_{NN} \sim 5.6\ d_{NN}$. In the second configuration, a rectangular ($11 \times 2\sqrt{3}$) unit cell was used. The Au adatoms are located at the *fcc* and *hcp* sites alternatively, corresponding to a small bend between two neighboring PDI-Au motifs with a bend angle of $\theta \sim 6^{\circ}$ and periodicity of $L_0 = 5.5\ d_{NN}$ per PDI-Au motif. A ($2 \times 4 \times 1$) and a ($1 \times 4 \times 1$) *k*–grids were employed for the two configurations, respectively.

5.3. Results and Discussion

5.3.1 Adsorption structures of PDI and BPDI molecules on the Au(111) surface

Figure 5.1a displays a STM image of the clean Au(111) surface. It exhibits the well known herringbone reconstruction with a $\left(22\times\sqrt{3}\right)$ unit cell.[136] The addition of one extra Au atom for every 22 surface atoms into the surface layer along $\left[1\bar{1}0\right]$ direction induces a compression of the surface layer. The surface compression causes a mismatch between surface Au layer and the bulk, and yields alternating domains of regular *fcc* and *hcp* stacking separated by incommensurate regions (soliton lines). With PDI molecules dosed on the Au(111) surface at 95 K, the STM image shows a wide range of surface morphologies that include three-dimensional (3-D) islands, short molecular chains and individual molecules bound at step edges. (Figure 5.1b) On the terraces of Au(111) surface, there are two characteristic PDI morphologies corresponding to small 3-D islands and short molecular chains with a maximum length of ~10 nm. The terraces also exhibit bare regions where the Au(111) herringbone reconstruction is clearly visible.

As shown in Figure 5.2, a dramatic reorganization occurs on the surface after annealing to 300K: long 1-D molecular chains form across the entire Au(111) surface as shown in Figure 5.2. There are still molecules on the step edges, but all of the 3-D islands and short chain structures have disappeared. The majority of the chains are aligned along the $\left\langle 1\,\bar{1}0\right\rangle$ directions of the Au(111) surface. Some of the molecular chains extend across entire Au terraces and are more than 100 nm in length. The line profile shown in Figure 5.2c along one of the chains gives a repeat distance of 11.7 ± 0.2 Å which is the same as that found along the shorter chains observed immediately after deposition at 95 K. It is also consistent with previous experiments on similar

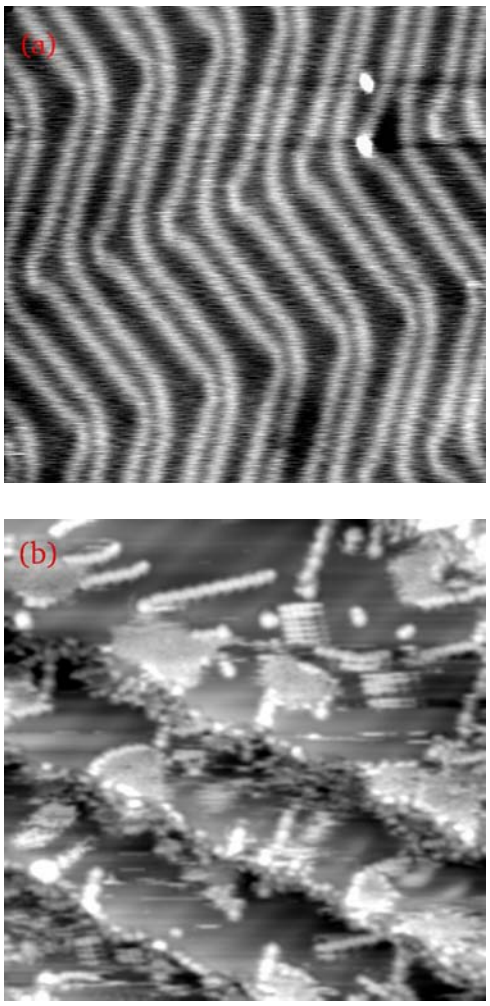

Figure 5.1: STM images of Au(111) before and after dosing PDI at 95 K. (a): clean Au(111) surface, 40×40 nm; tunneling parameters: sample bias voltage (V_b) = -0.50 V, current set point (I_t) = 0.20 nA; (b): PDI on Au(111) dosed at 95 K, 35×35 nm, V_b = -1.14 V, I_t = 0.33 nA.

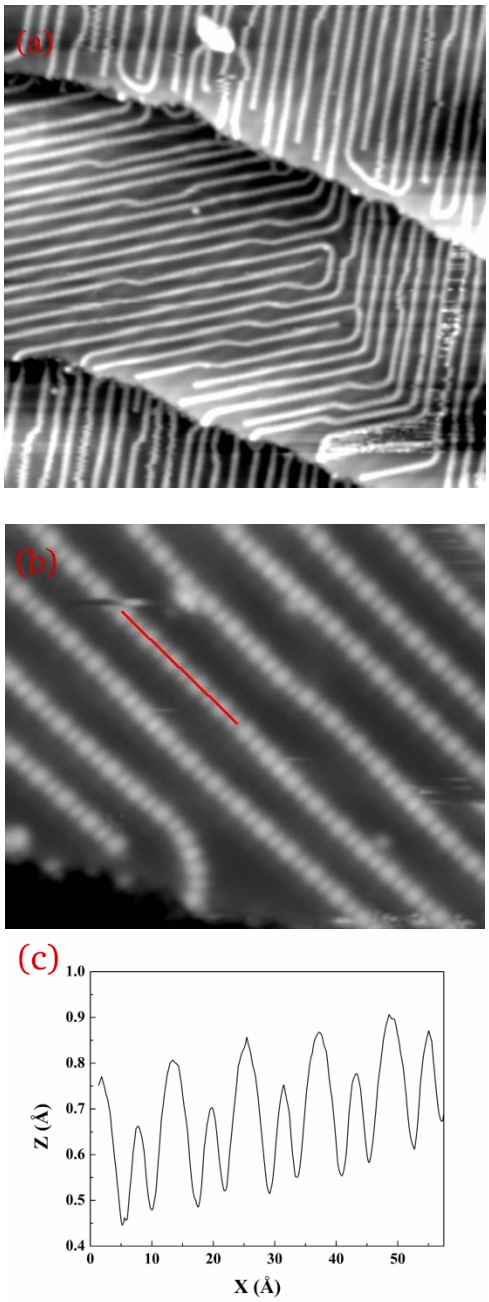

Figure 5.2: STM images of PDI on Au(111) dosed at 95 K and annealed to 300 K. (a): 70×70 nm; V_b = -0.92 V, I_t = 0.35 nA; (b): 17.5×14.8 nm, V_b = -1.03 V, I_t = 0.17 nA; (c): profile of a molecular chain segment showing the repeating distance between basic units.

1-D chain structure of PDI/Au(111) prepared at 300 K.[115] The chains are largely straight and continuous on Au terraces, but form loops that prevent the chains from crossing a step edge. Some kinks are formed when the molecular chains extend across the soliton from *hcp* to *fcc* region. The herringbone reconstruction of the Au surface is still visible below the PDI molecular chains. At the coverage shown in Figure 5.2b, the lateral distance between PDI chains is 21.5 ± 1 Å. The separation between PDI chains is remarkably uniform over the whole surface. From the STM images, we estimate a coverage of 0.3 ML, which is in reasonable agreement with our estimated coverage from previous temperature programmed desorption experiments using similar dosing condition. (Chapter 4)

BPDI molecules are also observed to self-assemble into 1-D molecular chains on the Au surface at 300 K. The distance between the monomer repeating units is 16.1 ± 0.3 Å, which is longer than in the PDI chains by approximately what would be expected for the addition of the second phenyl ring. This provides direct evidence for the adsorption model: isocyanide molecules are lying-down on the surface and the 1-D molecular chains include alternating isocyanide molecules and Au adatoms. The overall BPDI chain lengths are comparable to that of PDI and they also extend across the terraces of the Au(111) surface. The BPDI chains are generally not as straight as for PDI, although the overall orientation still follows the $\langle 1\bar{1}0 \rangle$ directions. Small deviations from linearity (less than 10°) are probably due to the increased length of the BPDI molecule compared to PDI. More specifically, the length of diisocyanide molecule must fit between two Au atoms whose positions must be commensurate with underlying atomic structure of the reconstructed Au(111) surface. Assuming that the Au atoms participating in the diisocyanide chains are adatoms located at 3-fold *fcc* or *hcp* surface sites,

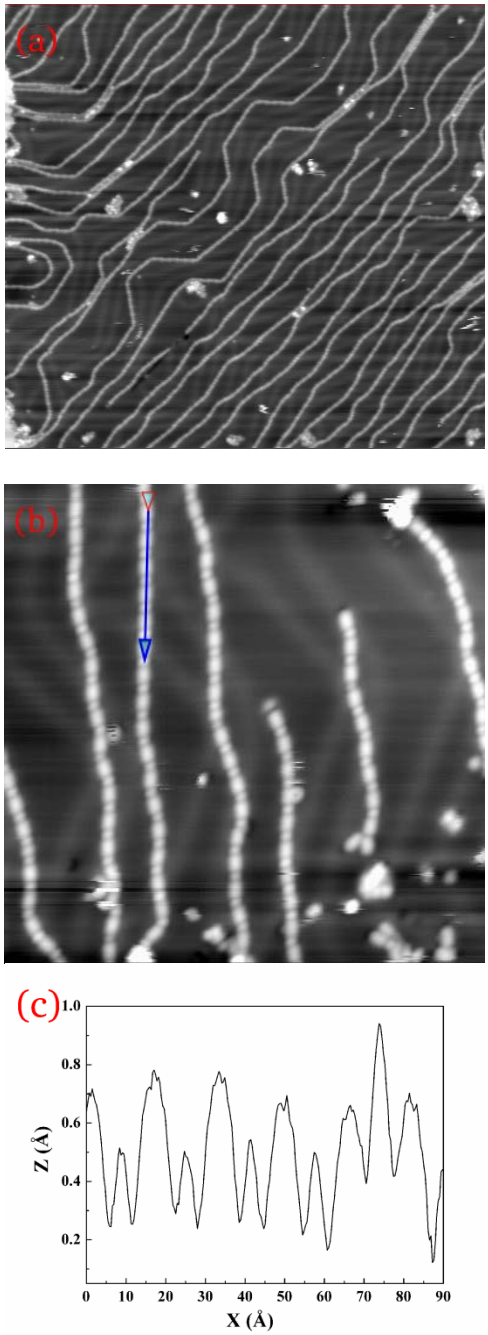

Figure 5.3: STM images of BPDI on Au(111) dosed at 300 K. (a): 51.8×47.4 nm; V_b = -1.6 V, I_t = 0.15 nA; (b): 29×29 nm, V_b = -1.6 V, I_t = 0.2 nA; (c): profile of a molecular chain segment showing the repeating distance between basic units.

then it is possible to determine lattice vectors which match the periodicity of the PDI and BPDI chains. It is straightforward to show that the longer BPDI chains have more possible lattice vector directions (relative to one end fixed in place) than the shorter PDI chain. These simple geometric arguments show that it is possible to have many small changes in direction in the BPDI chains in agreement with the STM observations. Finally, we note that the BPDI molecular chains prefer to grow in *fcc* regions of Au herringbone reconstruction whereas the straighter PDI chains cross both *fcc* and *hcp* regions of the surface (see Figure 5.3).

DFT calculations on PDI/Au(111) and BPDI/Au(111) also support the adsorption model involving isocyanide-Au_{ad} repeating units. Figure 5.4 shows the calculated lowest-energy structures of PDI-Au_{ad} and BPDI-Au_{ad} chains on Au(111) at half coverage. The periodicities are 11.8 Å and 16.2 Å for the two chains respectively, which should be 11.5 Å and 15.9 Å if the experimentally determined gold lattice constant of 4.08 Å is applied for to theoretical results. The calculated monomer chain length of the PDI-Au_{ad} chain is in excellent agreement with the measured unit chain lengths of 11.7 ± 0.2 Å, although different choices of the chain directions and adjacent Au adatom positions (e.g. *fcc-hcp*, *fcc/hcp-bridge*) exist. In our calculations, the PDI-Au_{ad} chains are assumed to run along the $[1\bar{1}0]$ direction which give the best match to the observed chain alignment with respect to the herringbone patterns of the reconstructed of Au(111) (Figure 5.2). The BPDI-Au_{ad} monomer chain length was measured to be 16.1 ± 0.3 Å. We choose the two chain directions described in the theory calculation methods because they make small angles (3° and 0°) with the $[1\bar{1}0]$ direction, as frequently observed in STM images. (Figure 5.3) Table 5.1 lists the computed equilibrium structures of PDI-Au_{ad} and BPDI-Au_{ad} chains on Au(111). Most geometric features are similar for PDI and BPDI chains. The computed

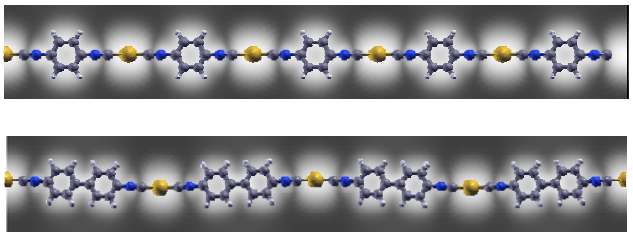

Figure 5.4: DFT-optimized single chain structures of PDI-Au_{ad} (upper panel) and BPDI-Au_{ad} (lower panel) on Au(111). The background plots are simulated STM images at sample bias of □1.5 V. For clarity, the Au(111) substrate is not shown.

Table 5.1: Equilibrium structures and adsorption energy of PDI-Au_{ad} and BPDI-Au_{ad} chains on Au(111). $\theta_{N\equiv C}$ is the tilt angle of N≡C bond from the surface; h_{mol} and h_{Auad} are the maximum height of molecule and the Au adatom from the clean Au(111) surface, respectively. BPDI-Au_{ad} chain configuration 1 corresponds the chain running straight with all Au adatoms located at the *fcc* sites. In the configuration 2, the Au adatoms are located at the *fcc* and *hcp* sites alternatively.

	Coverage (ML)	$d_{N\equiv C}$ (Å)	$\theta_{N\equiv C}$ (°)	$d_{Au_{ad}\square C}$ (Å)	h_{mol} (Å)	$h_{Au_{ad}}$ (Å)	E_{ads} (eV)
PDI	1/2	1.19	14.2	2.02	3.58	2.61	1.23
	1	1.19	14.7	2.03	3.59	2.56	1.03
Ref. [115]	1	1.18	13	2.00	3.6		
BPDI	½ (config. 1)	1.19	10.6	2.05	3.69	2.78	1.32
	½ (config. 2)	1.19	12.8	2.03	3.70	2.62	1.47

distance between the carbon atom on the isocyanide group and the gold adatom is about 0.1 Å longer than that in the case when the BPDI/PDI molecules are vertically adsorbed on the gold adatom (d[Au−C] =1.97 Å). This may be caused by the fact that the gold adatom is attached to two isocyanide groups in the former case but only one in the latter. Moreover, the gold adatom is more loosely bound to the underlying Au(111) substrate for the molecules lying flat, with $h_{\mathrm{Au_{ad}}}$ between 2.6-2.8 Å, while it is much smaller for the vertical adsorption (2.1 Å). Because of the horizontal length of the monomer unit is restricted by the periodicity of the unit cell, the molecular plane is not perfectly flat. The center of the molecule is bulged outwards away from the substrate, and the isocyanide groups at the two ends make an angle between 10-15 degrees with the surface.

For PDI-Au_{ad} on Au(111), the adsorption energy decreases slightly from 1.23 to 1.03 eV as the coverage increases from $\Theta = 1/2$ to $\Theta = 1$. Here, the adsorption energy, E_{ads}, is defined as the difference between the total energy of adsorption system and the total energy sum of the clean Au(111) surface, the gas phase molecule, and a bulk Au atom (to be extracted to become a gold adatom):

$$E_{ads} = E[\mathrm{Au(111)}] + E[\mathrm{molecule}] + E[\mathrm{bulk\ Au\ atom}] - E[\mathrm{molecule\text{-}Au_{ad}}] \qquad (1)$$

In contrast, E_{ad} of PDI vertically adsorbed on a *fcc* Au adatom at low coverage is computed to be about 0.67 eV, which is significantly smaller than that for the flat adsorption geometry. The adsorption geometry and energetics for BPDI-Au_{ad} on Au(111) are similar to those of PDI-Au_{ad}, despite of the different orientation and periodicity of the two chains.

Au atoms can be extracted from the surface layer when the interaction between adsorbates and Au(111) surface is strong enough.[144,145] Previous break junction experiments demonstrate that the strength of Au-CN bond is comparable to Au-S bond and stronger than Au-

Au bond.[146] With thiolate molecules on Au(111) surface, the formation of Au adatoms partially or completely lifts the herringbone reconstruction,[147] and can even induce surface pits or eroded surface terraces at high coverage.[135,148] In the present work, the Au herringbone reconstruction is still visible underneath the PDI molecular chains at a PDI coverage as high as ~0.3 ML. As noted above, the presence of the underlying herringbone reconstruction places constraints on the positions of the Au adatoms and, hence, the orientations of PDI and BPDI molecular chains.

Because less energy is required to lift the Au atoms at elbows of the herringbone reconstruction, the low-coordination Au atoms likely act as adatoms in the molecular chains (Figure 5.3a and 5.3b) and nucleation sites to initiate chain growth. Figure 5.5 displays a few PDI molecular chains dosed at 300 K with very low coverage. Some short chains grow in the *fcc* region and stop growth at the soliton wall which suggests the existence of a small energy barrier for the chain extend into *hcp* region. Both PDI and BPDI molecular chains are terminated with molecules and not Au atoms for both high and low coverage. The later suggests that two isocyanide bonds may be required to stabilize an Au adatom. In addition, the chain ends of both PDI and BPDI exhibit small, faint features with dark halo rim. The latter is attributed to the electron depletion of Au metallic states near the end of the chain which has been observed for similar organic system on metal surface.[149,150]

For a high coverage of PDI on the Au surface, Boscoboinik et, al. proposed that additional PDI molecules could bind vertically to the Au adatoms within the molecular chains and thereby give rise to both bound and free isocyanide groups as indicated by infrared spectroscopy for PDI SAMs prepared from solution.[115] However, our STM images (Figure 5.6) at full monolayer coverage of PDI on Au(111) show no height variations consistent with vertically aligned PDI molecules. Instead of additional PDI molecules binding at Au adatom sites

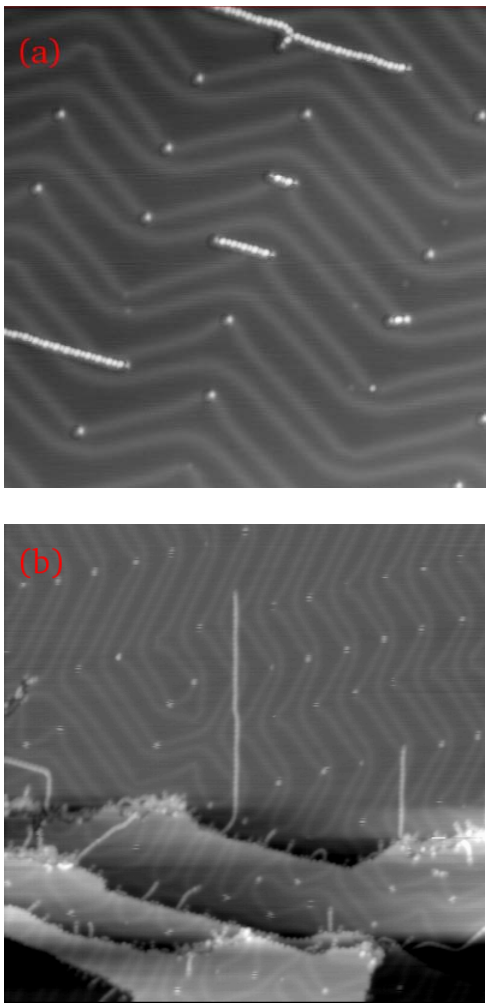

Figure 5.5: STM images of PDI on Au(111) dosed at 300 K. (a): 49×49 nm; V_b = -1.5 V, I_t = 0.12 nA; (b): 80×80 nm; V_b = -0.53 V, I_t = 0.50 nA.

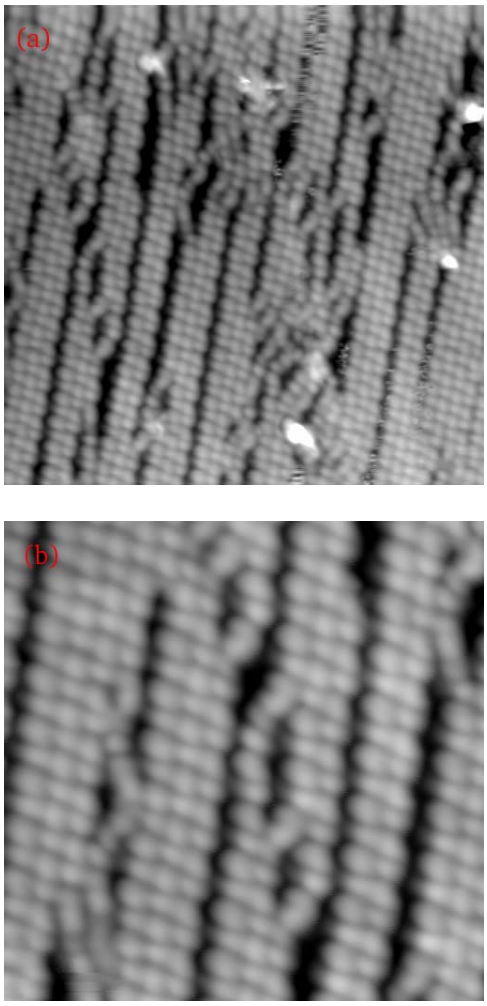

Figure 5.6: STM images of PDI on Au(111) dosed at 95 K and annealed to 300 K. (a): 17.5×17.5 nm; V_b = -1.08 V, I_t = 0.51 nA; (b): 8.8×8.8 nm V_b = -1.08 V, I_t = 0.51 nA.

at high coverage, we observe “interlocking” of adjacent chains when they are crowded close together. Specifically, chains that appear to touch at high coverage (6.5 Å separation) are displaced such that the phenyl rings of the PDI molecules of one chain are aligned with the Au atoms in the neighboring chain. This alignment suggests a weak attraction between the Au adatoms and π electrons of benzyl ring. This high coverage absorption structure is distinctly different from PDI SAMs formed from solution on Au(111) where the molecules are thought to be vertically aligned and anchored via one isocyanide group. It is likely that differences in deposition conditions, i.e., vapor deposition in vacuum versus deposition from solution in the presence of solvent molecules, are responsible for the different high coverage PDI-Au(111) adlayer structures. Being able to control the adsorption morphology by choosing different deposition methods could be especially beneficial where it is possible to exploit other properties, e.g., electronic structure, which strongly depends on the molecular configuration at interface.

5.3.2 Work function change of PDI(BPDI)/Au(111) surface

According to the DFT calculations, substantial charge transfer takes place at the interface when the molecular orbitals of BPDI are coupled to the Au substrate through bonding to the Au adatoms. Such charge transfer processes can be analyzed by looking at the difference between the electron density distribution of the whole adsorption system and those of the isolated subsystems.

Figure 5.7 shows the changes of the electron density when the PDI-Au monomer is adsorbed on the clean Au(111) surface. It can be clearly seen from Figure 5.7c that overall the PDI molecules lose electrons upon adsorption, whereas an accumulation of electron density occurs between the first gold surface layer and the Au adatoms. The normal component of the

surface dipole moment per PDI-Au_{ad} monomer was evaluated to be μ_z = 4.0 Debye (Θ = 1/2) and μ_z = 2.6 Debye (Θ = 1), respectively. The drastic reduction of μ_z at high coverage is caused by the depolarization effect from the repulsive electrostatic interactions between parallel dipole moments on the surface. The corresponding work function shift was evaluated from the Helmholtz equation to be -1.2 and -1.5 eV, which is very close to the measured work function reduction of 1.47 eV at full monolayer coverage. (Chapter 4)

Figure 5.8 shows the changes in the electron density when the BPDI-Au_{ad} chains are adsorbed on a clean Au(111) surface. The molecular chains also lose electrons upon adsorption and the Lowdin population analysis indicates a charge transfer of about 0.6 electrons from the chain to the substrate, which are mostly accumulated between the first layer of Au atoms and the Au adatoms. The isosurface of electron loss (shown in blue color) in Figure 8 bears the same shape as the LUMO of BPDI-Au_{ad}. This state is half occupied in the molecular chain, but is pushed into the conduction band when coupled with Au(111), leading to the overall electron loss of the chain. The normal component of the total surface dipole moment, μ_z, was evaluated to be 5.0 Debye per BPDI-Au_{ad} monomer unit for both chain configurations chosen in calculation (only config.1 is shown in Figure 5.8). The large magnitude of μ_z is mostly induced by charge transfer occurring at the interface, as μ_z of the isolated BPDI-Au_{ad} chain and that of the clean Au(111), both fixed at the optimized geometry of the adsorption system, are evaluated to be nearly negligible (within ±0.15 Debye). According to the Helmholtz equation, the charge transfer induced dipole for BPDI-Au_{ad} leads to a -1.08 eV reduction of the Au(111) work function.

5.3.3 Electronic state of PDI and BPDI molecular chains on the Au(111) surface

STS investigations were conducted on a section of a BPDI-Au_{ad} chain consisting of three

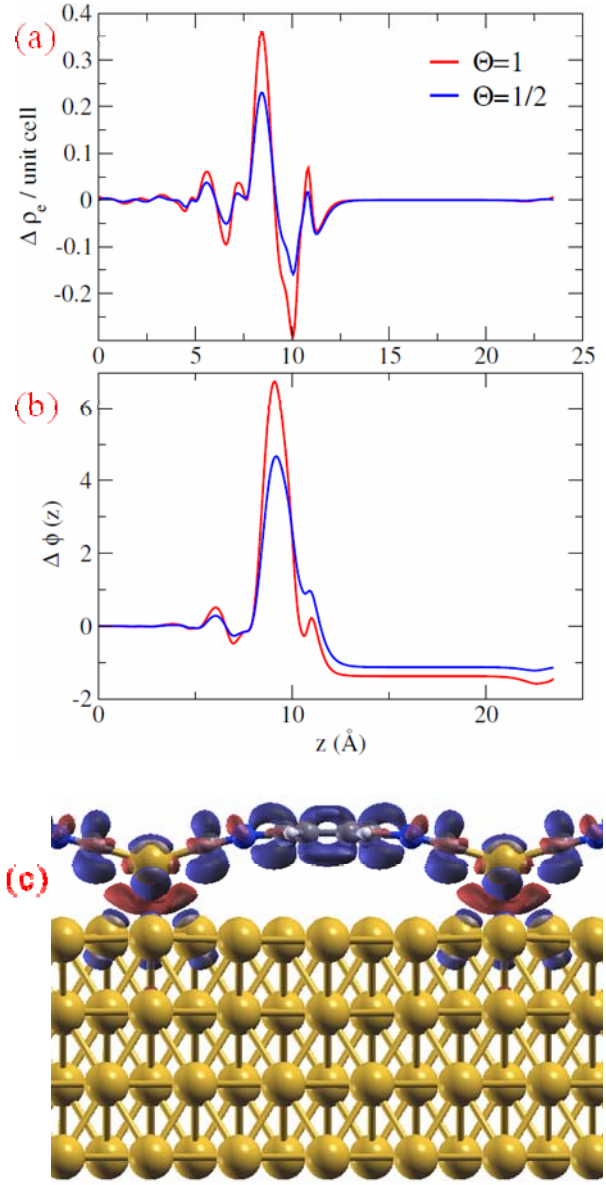

Figure 5.7: Plane averaged changes in (a) electron density and (b) electrostatic potentials with PDI-Au chains are deposited on Au(111) surface; (c) side view of the isosurface for electron density difference between PDI-Au_{ad}/Au(111) and the isolated subsystems, i.e. isolated PDI-Au_{ad} chain and /Au(111).. Red: electron gain; blue electron loss.

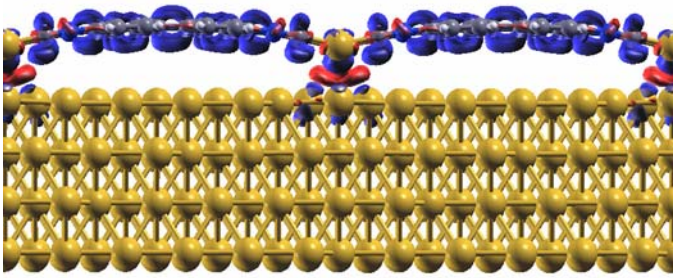

Figure 5.8: side view of the isosurface for electron density difference between BPDI-Au_{ad}/Au(111) and the isolated subsystems, i.e. isolated BPDI- Au_{ad} chain and /Au(111). Red: electron gain; blue electron loss.

BPDI-Au_{ad} monomer units as shown in Figure 5.9. The experimental and theory simulated dI/dV maps at different bias voltages are also presented. Since dI/dV measurements probe the local density of states (LDOS), the image corresponds to a map of LDOS at the specific energy relative to the Fermi level. At a sample bias voltage from –1.0 V to –0.1 V, the Au adatom and the phenyl rings in BPDI molecule appear bright which is consistent with the theoretical simulations. The bright images indicate high LDOS on the BPDI molecule and the Au adatom. Figure 5.10 shows the dI/dV curve on the BPDI-Au_{ad} chain. There is an occupied state at –0.7 eV below the Fermi level which is similar with that observed in 2PPE experiment for PDI molecular chains on Au(111) surface. (refer to Figure 4.5 in Chapter 4) The occupied state results from the interaction between the isocyanide group and the Au adatom. Since the Au-CN bond is the same for both PDI and BPDI in the molecular chain, the occupied sate is observed for both systems. With bias voltage from –0.1 V to about 0.5 V, there is no clear contrast between the BPDI–Au_{ad} chain and Au surface. The localized electronic state below the Fermi level disappears completely. When the bias voltage is increased above 0.5 V, a high LDOS is observed on the isocyanide groups in BPDI molecule and this feature becomes more clearly visible at higher bias voltage. However, theoretical simulation shows that the phenyl rings in BPDI molecule have high LDOS at 1.0 V bias voltage. STS experiments measure the hybridization electronic state between Au(111) surface and BPDI molecular chain. The contribution from the Au substrate in the dI/dV map likely causes this disagreement between the experimental and theoretically simulated images. The dI/dV maps for a PDI-Au_{ad} chain is displayed in Figure 5.11. At negative bias voltage, Au adatom appears brighter than PDI molecule. The contrast switches at positive voltage which indicates that the Au adatom has a higher LDOS below the Fermi level and PDI molecules have a higher one above the Fermi level. These trends are consistent with the

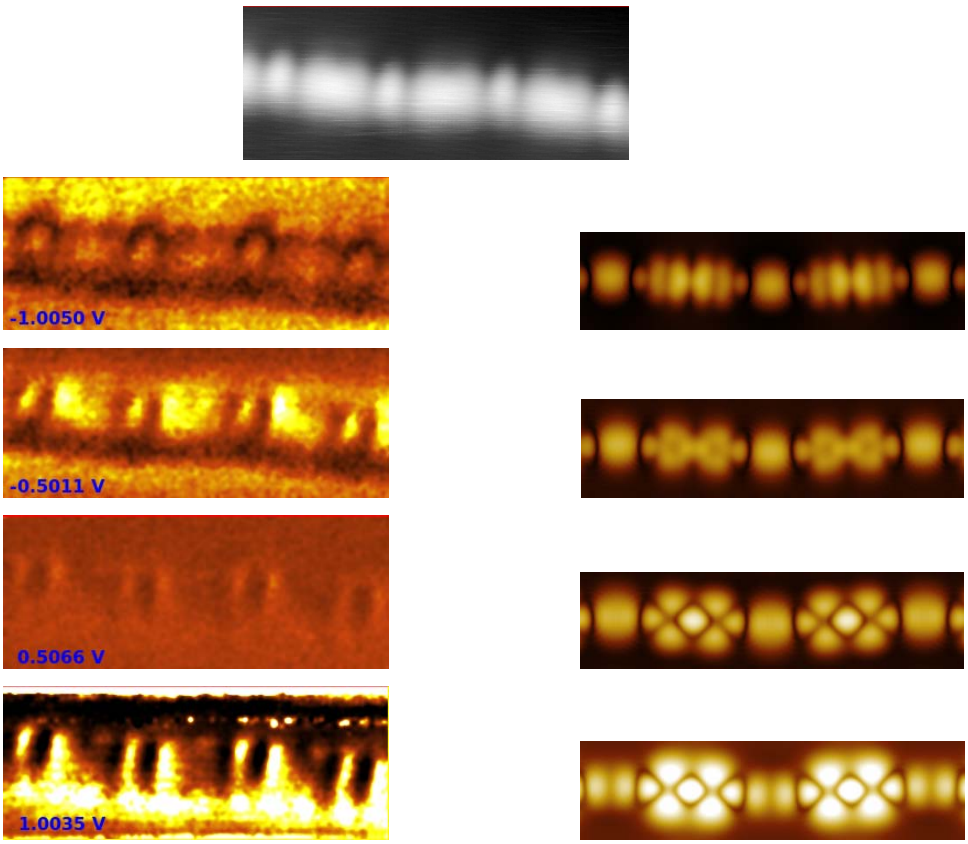

Figure 5.9: Top: STM topography image of BPDI on Au(111) dosed at 300 K; Left: d*I*/d*V* maps of the region presented in the top image at different sample biases; Right: Theory simulated d*I*/d*V* maps of the region at different sample biases.

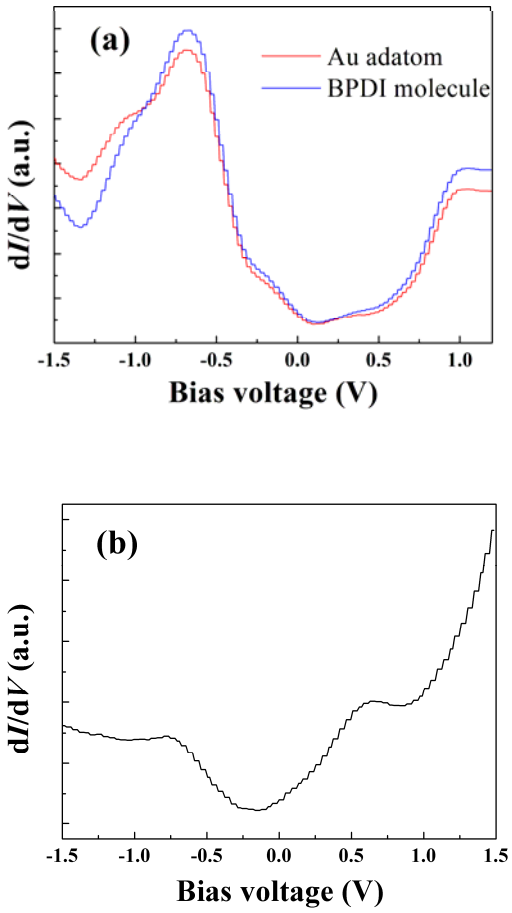

Figure 5.10: d*I*/d*V* curves for (a) BPDI molecule and Au adatom in BPDI-Au_{ad} chain and (b) in PDI-Au_{ad} chain on Au(111) surface.

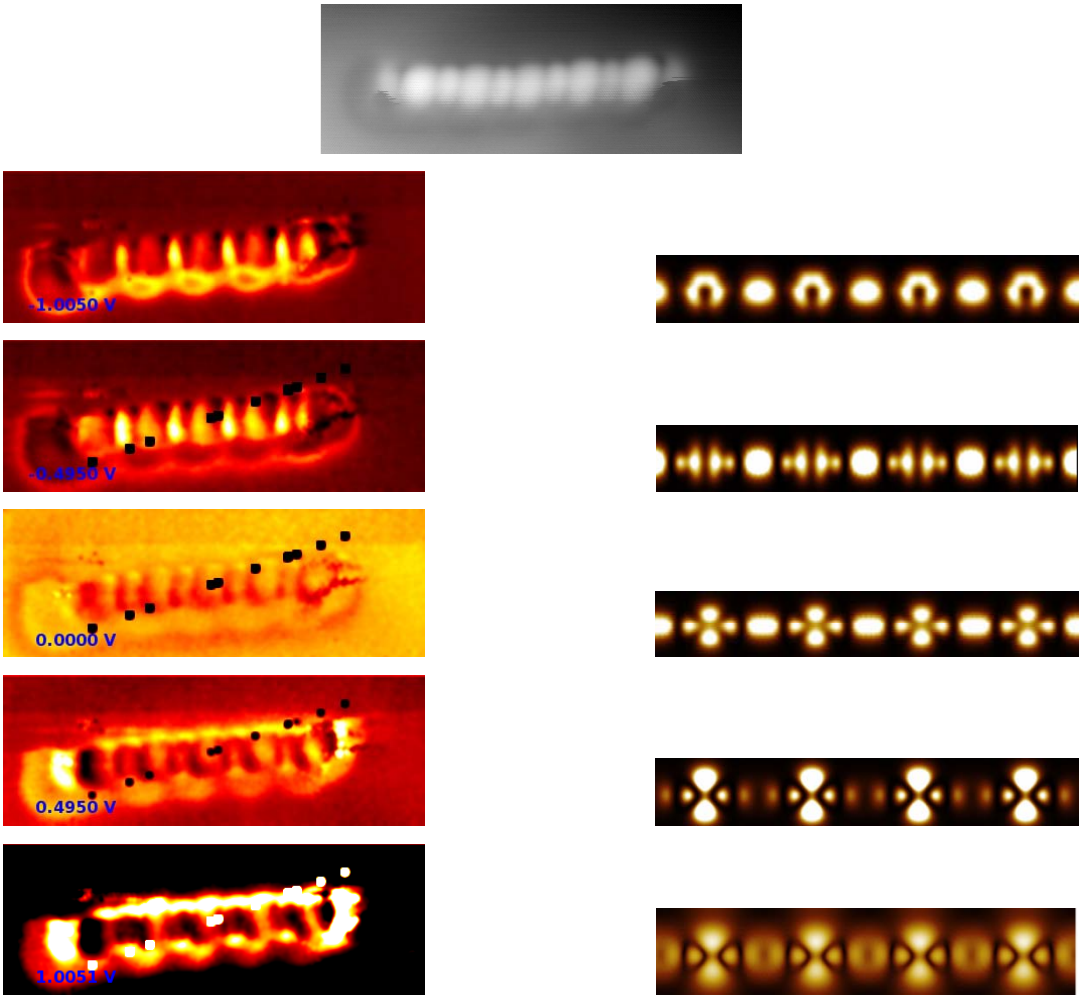

Figure 5.11: Top: STM topography image of PDI on Au(111) dosed at 300 K; Left: d*I*/d*V* maps of the region presented in the top image at different sample biases; Right: Theory simulated d*I*/d*V* maps of the region at different sample biases.

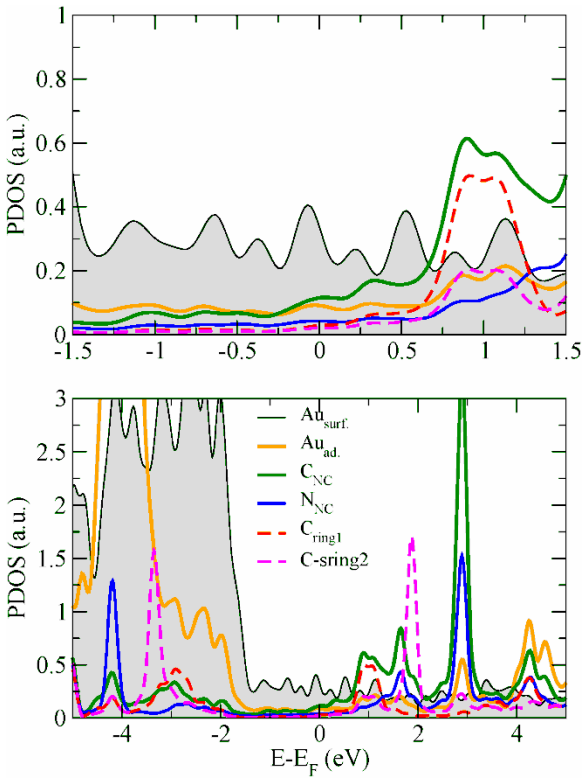

Figure 5.12: Projected density of states of PDI-Au_{ad}/Au(111). Orange, black, green, blue, red and magenta lines represent PDOS from the Au adatom, Au surface atom, carbon atom in isocyanide group, nitrogen atom in isocyanide group and the two rings of PDI molecule, respectively.

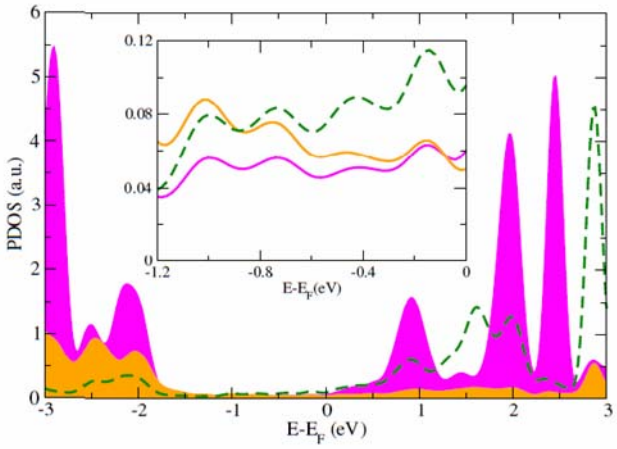

Figure 5.13: Projected density of states of BPDI-Au_{ad}/Au(111) (Config.1). Orange, magenta and green lines represent PDOS from the Au adatom, one of the two rings of BPDI, and one of the two isocyanide groups, respectively.

calculated PDOS of PDI-Au_{ad} chains on Au(111) as shown in Figure 5.12. An unoccupied electronic state is located at 0.8 eV above the Fermi level and has mostly contribution from the PDI molecule. On the other hand, for the occupied state at 2 eV below the Fermi level, the Au adatom has much larger contribution than PDI molecule. Between these two electronic states, the non-vanishing PDOS are mostly bulk resonance states involving the Au *d*-band, which is weakly coupled to the orbitals of the Au adatom and BPDI molecule. For BPDI-Au_{ad} chains on Au(111), the gap is similar with that in PDI-Au_{ad} chains. (Figure 5.13) The magnitude of the gap is consistent with the computed HOMO-LUMO gap for the gas-phase BPDI molecule. However, as DFT with local and semilocal approximations tends to underestimate the HOMO-LUMO gap,[110] one expects the actual state positions to be displayed even further away from the Fermi level.

5.4. Summary

When PDI and BPDI molecules are adsorbed on Au(111) surface at 300 K, these molecules form 1-D diisocyanide-Au_{ad} chains evidenced by the dependence of repeating monomer unit distance on the molecular length. The initial growth of the chain starts from a step edge or an elbow dislocation site on Au surface. At full monolayer the PDI-Au_{ad} chains are displaced such that the phenyl rings of the PDI molecules of one chain are aligned with the Au adatoms in the neighboring chain. This alignment suggests a weak attraction between the Au adatoms and π electrons of phenyl ring. Compared to PDI molecular chain, BPDI-Au_{ad} chain is more flexible and shows small deviations from linearity because of the larger monomer unit length. It provides a possible way to control the growth direction and pattern of diisocyanide molecular chains by the choice of molecular structure. As demonstrated by DFT calculations, the diisocyanide-Au_{ad} chain loses electrons upon adsorption, whereas an accumulation of electron

density occurs between the first gold surface layer and the Au adatoms. This charge transfer induces an interfacial dipole moment that results in large work function decrease, consistent with 2PPE experimental observations on PDI/Au(111).(Chapter 4) STS experiments and PDOS from DFT calculations reveal that the Au adatom is the dominant contribution to the density of states below the Fermi level while the diisocyanide molecules contribute mostly to the unoccupied state.

In the future, it would be useful to investigate the density of states of the duiisocynaide systenms in the absence of the Au substrate contributions which result in a large background tunneling signal. In order to decouple the interaction between the diioscyanide molecules and Au substrate, the diisocynaide molecules could be dosed on a thin insulating layer, i.e., NaCl on Au surface. In addition, by co-depositing Au clusters and diisocyanide molecules onto the insulating layer, it should be possible to examine the self-assembly process and see more clearly how Au adatoms modify the electronic structure of the diisocyanide molecules.

Chapter 6. Local work function of size-selected Mo_xS_y clusters on Al_2O_3/NiAl(110)

6.1. Introduction

Molybdenum sulfide catalysts are widely used in hydrodesulfurization (HDS) and hydrodenitrogenation (HDN) reactions.[25] The need for catalysts with improved activity and selectivity has increased due to strict environmental regulations to control sulfur (SO_x) and nitrogen (NO_x) emissions. This need can only be met through a better understanding of how catalysts like molybdenum sulfide actually activate adsorbates for reaction. Commercial molybdenum sulfide catalysts typically consist of MoS_2 nanoparticles supported on a high surface area alumina powder (γ-Al_2O_3). The catalyst nanoparticles are present primarily as single S–Mo–S trilayers in the shape of slightly truncated triangles.[151,152] Along the edges of the nanoclusters there are metallic states which play a critical role in the HDS reaction. They were observed to be adsorption sites for sulfur-containing organics such as thiophene.[153] The morphology, electronic structure and reaction activity of the MoS_2 clusters change with size.[154,155] Scannning tunneling microscope (STM) experiments showed that the adsorption properties of MoS_2 nanoclusters towards dibenzothiophene enhance when the cluster size is reduced below a threshold value of 1.5 nm.[156]

In order to explore the size-dependent properties of molybdenum sulfide, mass-selected Mo_xS_y clusters have been extensively studied experimentally and theoretically.[157-161] The most stable Mo_xS_y clusters investigated here have structures consisting of a Mo metallic core with most of the sulfur atoms bonding along the edges or in the faces of the metal core structure.[158-160] For instance, the four Mo atoms are arranged in a tetrahedron in the Mo_4S_6 cluster and the S

atoms are bridge-bonded along each edge.[159,161] When deposited on a Au(111) surface, DFT calculations showed that the Mo_4S_6 cluster remains intact with only a small trigonal distortion due to the formation of Au–S and Au–Mo bonding interactions.[158,159] Similar behavior is also found for quasi-cubic cluster Mo_6S_8 on Au(111) surface predicted by DFT calculation.[160,162] In addition, Auger electron spectroscopy (AES) experimental data demonstrated that the deposited clusters tend to deposit on bare areas of the Au(111) surface until forming a single compact layer when depositing at 300 K.[158] This is consistent with the theoretical predictions for Mo_6S_8 clusters on the Au surface.[162] Specifically, there are several quasi-isoenergetic adsorption positions for Mo_6S_8 on Au(111) surface and the barrier is small between adjacent strong adsorption sites. As a result, Mo_6S_8 clusters on Au(111) surface are predicted to form a an ordered monolayer.

As noted above, industrial catalysts for HDS reactions typically use alumina powder as a support in order to disperse and stabilize the molybdenum sulfide nanoparticles. Both the defect structures of the alumina support and its interaction with the molybdenum sulfide particles are important for catalyst performance. Unfortunately, the complex structure of real catalysts makes it difficult to characterize the microscopic processes taking place on the surface. In order to address this problem, a ultrathin aluminum oxide film grown on a metallic substrate has been intensively investigated as a model alumina support.[163-166] The advantage of using an ultrathin oxide film is that the charging of the sample during electron spectroscopy measurements can be avoided. This allows surface science techniques to be exploited to elucidate the electronic and catalytic properties of the model catalyst. The ultrathin aluminum oxide film formed by oxidation of NiAl(110) surface has been studied by various methods, such as STM[167], AFM,[168] LEED, X-ray diffraction[169] and theoretical simulations.[170] From these studies, the structure of

well-ordered alumina/NiAl(110) films are atomically flat with a thickness of approximately 5 Å, corresponding to two Al–O layers. The alumina film is oxygen terminated and grows in two reflection domains which are tilted by ±24° with respect to NiAl[$1\bar{1}0$] direction. Defects on the film include point defects (oxygen vacancies) with a concentration of about 10^{13} cm^{-2} and two types of line defects: reflection domain boundaries and antiphase domain boundaries.[171]

In this work, we present a study of the valence electronic structure of size-selected Mo_xS_y clusters deposited on Al_2O_3/NiAl(110) using two-photon photoemission (2PPE). In particular, 2PPE was used to measure the work function of the surface as a function of cluster size and coverage, which provided a way to probe the electron transfer between the clusters and the alumina support. The latter is expected to lead to a better understanding of electronic effects on the catalytic activity of the Mo_xS_y-Al_2O_3 system. Recent studies by Kelvin probe force microscopy have shown that the work function is a local property in the vicinity of a defect or metal cluster on a metal oxide surface.[172,173] For instance, on the TiO_2(110) surface a crystalline island protruding on a terrace exhibits a local elevation of the work function.[174] The laterally oriented dipoles arrayed on the steps of the island were proposed to explain the local increase of the work function. When depositing Pt clusters with diameters of 2–3 nm on TiO_2(110) surface, the work function on the Pt clusters is smaller than that on the surrounding TiO_2 surface because of the electron transfer from the Pt clusters to the Ti cations on the surface. The decrease of the work function depends on the Pt–TiO_2 interface area. With larger interface area, more dipoles result in a larger increase of the work function.[173]

On the ultrathin Al_2O_3 film prepared by oxidation of a NiAl(110) single crystal,[167,175] line defects and step edges have local work functions which are smaller than that of the reflection domains as measured by frequency modulation atomic force microscope.[176,177] A local band

bending at the line defects predicted by DFT calculations results in a shift of the valence and the conduction bands and concomitantly, a change in the work function.[175] With the formation of an alumina film on NiAl(110) surface, UPS revealed a decrease in the photoelectron intensity from the hybridization of the Ni d and Al sp valence electrons centered at 1.6 eV below the Fermi level.[178] The decrease in UPS signal indicates that the alumina film will reduce the photoelectron intensity from the excitation of underlying NiAl(110) surface although the Al_2O_3 film has a large band gap of 8 eV (8.7 eV for bulk material).[163,171] Previous photoemission experiments on 10 ML MgO/Mo(100) show that electrons originating from molybdenum substrate dominate the spectra excited with photon energies of 3.1~4.7 eV because the mean free path of excited electrons is larger than the thickness of MgO film.[179] Considering that the thickness of a 2 ML alumina film is only about 5 Å, it is not surprising that the photoelectrons excited from NiAl(110) surface are not be blocked by the alumina film.

In this work, Mo_xS_y clusters (x/y: 2/6, 4/6, 6/8, 7/10) were deposited using a size-selected deposition apparatus under ultrahigh vacuum (UHV) conditions. The cluster distribution on the film was investigated by Auger electron spectroscopy (AES) and two-photon photoemission spectroscopy (2PPE) was used to measure the local work function. The existence of a local work function provides the ability to measure the coverage dependence of the work function over the deposition area of a single sample. It reduces the time significantly for collecting data at different coverages, and more importantly, minimizes the effect of day-to-day variations in experimental conditions. With Mo_xS_y clusters deposited on the Al_2O_3 film, the work function on the clusters is larger than that on the surrounding Al_2O_3 film. A correlation between the work function increase and local cluster coverage was observed from which interface dipole moments are derived. The interfacial dipoles are different for the Mo_xS_y clusters

(x/y: 2/6, 4/6, 6/8, 7/10) studied in this work and the clusters are found to behave as independent particles for local coverage up to ~0.7 ML.

6.2. Experimental methods

The UHV deposition chamber (base pressure < 1×10^{-9} Torr) is equipped with surface sensitive instruments for cleaning the surface and carrying out electron spectroscopy and photoemission measurements. Prior to each experiment, the NiAl(110) surface was cleaned by sputtering with Ar^+ ions and annealing at 1300 K between each sputtering cycle. No impurities are detected by AES after the cleaning procedure. The ultrathin Al_2O_3 film was prepared by oxidizing the NiAl(110) crystal surface as established earlier.[175] The clean NiAl(110) was exposed to 1500 L of O_2 at 550 K, followed by an annealing cycle in vacuum at 1100 K. Two additional oxidation cycles were applied to fill open patches in the film. The film quality was monitored by AES, X-ray photoelectron spectroscopy (XPS) and low-energy electron diffraction (LEED).

The clusters are produced, size-selected and deposited using a cluster deposition beam line which has been described in detail elsewhere.[158] Briefly, molybdenum sulfide clusters were produced in a magnetron sputtering source where a molybdenum target was sputtered using a gas mixture of 4% H_2S in Ar. The $Mo_xS_y^+$ ions produced in the source were guided through an ion guide followed by a quadrupole mass spectrometer which selects a specific cluster mass by its mass-to-charge ratio. The mass-selected cluster beam was guided into the UHV deposition chamber using a hexapole ion guide. At the exit of the hexapole ion guide there is a quadrupole bender to deflect the $Mo_xS_y^+$ ions by 90° to prevent the deposition of neutral species. The kinetic energy distribution of the mass-selected ions was measured by applying a voltage ramp to the

Faraday cup while monitoring the cluster ion current. Normally, the clusters are deposited on the surface at a kinetic energy of 0.1~0.2 eV/atom to assure a soft-landing deposition. A LabView program was used to control the cluster deposition and measure the ion current on the crystal during deposition. The total number of clusters deposited on the surface was determined by integrating the ion current.

The cluster deposition area on the surface was obtained by Auger "line scans". Specifically, Auger spectra were taken at different positions on the crystal by translating along the horizontal (x-axis) and vertical directions (z-axis) with a spacing of by 0.5 mm. A 5 keV electron beam was used to excite the Auger transitions. The Auger peak intensity ratio of sulfur (154 eV) originating from the deposited clusters to oxygen (512 eV) from the alumina film was used to determine the deposition area. Under our operation conditions, the size of the Auger electron beam was less than 0.2 mm in diameter, significantly smaller than the measured deposition area (an ellipse, vertical radius ≈ 2 mm, horizontal radius ≈ 2.5 mm), thereby allowing reasonably precise measurements. No damages on the clusters by the electron beam have been observed evidenced by the same AES and 2PPE spectra before and after the Auger "line scans" experiments. The average cluster coverage was determined by multiplying the total number of clusters deposited on surface by the estimated area per cluster and dividing by the deposition area which contains 95% of the clusters. The cluster area was estimated assuming a circular cross section using the cluster radius (~3 Å) derived from previous density functional theory (DFT) calculations for the isolated neutral cluster.[41]

The setup for 2PPE experiments has been described in detail elsewhere,[116] and a brief description is given here. Laser radiation was generated by a Ti:sapphire oscillator (Spectra-Physics Tsunami) pumped by a 5 W cw solid-state Nd:YVO_4 laser at 532 nm (Spectra-Physics

Millennia V). The tunable Ti:sapphire fundamental wavelength (700–900 nm, 80 MHz repetition rate, 0.9-W average power, 100-fs pulse width) was frequency doubled and tripled in a time-plate harmonic generator (Photop TP-2000B). Both second (~400-nm) and third harmonic (~267-nm) beams were used to perform one-color 2PPE experiments. The laser pulses were p-polarized at an incident angle of 47.5° with respect to the surface normal. The beam was focused at the sample surface by an achromatic lens with a 38-cm focal length. The focused beam size on the crystal is estimated to be less than 250 μm.

Photoelectrons were detected with a hemispherical electron energy analyzer (Specs Phoibos 100) with an instrumental resolution of 35 meV. A bias voltage of -4 V was applied to the crystal in order to improve the collection efficiency of low-energy electrons. This allows for a more accurate determination of the low-energy secondary electron cutoff from which the surface work function is calculated. The 2PPE spectra were acquired with the crystal perpendicular to the electron energy analyzer. For Mo_xS_y clusters on the alumina film, the crystal was translated along the horizontal and vertical directions to take 2PPE spectra at different positions on the surface spaced by 0.25 mm.

6.3. Results and discussion

6.3.1. Cluster distribution on Al_2O_3/NiAl(110) surface

Figure 6.1a displays a typical Auger spectrum for Mo_6S_8 clusters deposited on the Al_2O_3 film. The Auger spectra were analyzed in the regions of S (154 eV), Mo (190 eV), O (512 eV) and Ni (849 eV). The Auger peak intensity ratio of sulfur to oxygen was plotted as a function of distance from the center of the cluster deposition area which was determined from the maximum sulfur to oxygen intensity ratio (Figure 6.1b). In both the horizontal and vertical directions, the

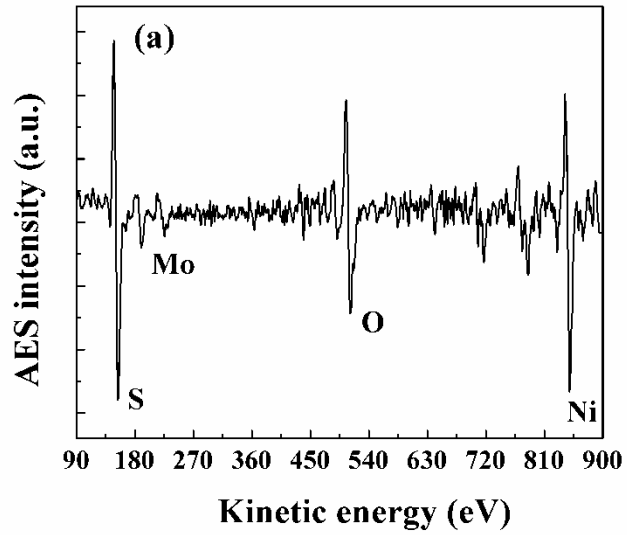

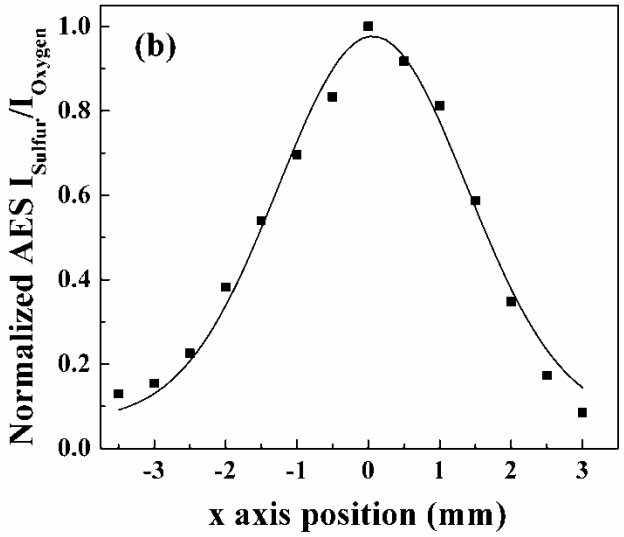

Figure 6.1: (a) AES spectrum of Mo_6S_8 deposited on Al_2O_3/NiAl(110) with an average coverage of 0.3 ML; (b) The normalized AES data of Mo_6S_8/Al_2O_3/NiAl(110) in horizontal direction on surface. The solid line is a Gaussian fit to the experimental data.

cluster density decreases from the center to the edge of the deposition area and the distributions are well described by Gaussian functions. Due to the velocity dispersion in the electrostatic field of the quadrupole bender, the distribution in the horizontal direction is wider than that in vertical direction. The deposition area containing 95% of the clusters is approximated by an ellipse with an area of 10~15 mm^2 and used to calculate the average cluster coverage within the deposition area. Based on the fitted Gaussian functions and total number of deposited clusters, the local cluster coverage can be determined. For all clusters investigated in this work (Mo_2S_6, Mo_4S_6, Mo_6S_8 and Mo_7S_{10}), the deposition area and the cluster distributions are similar.

The kinetic energy of the incoming clusters is measured to be 0.1~0.2 eV per atom which is low enough to assure that little damage will occur to either the cluster or alumina film during the deposition.[180] The sulfur atoms bridge-bonded to Mo atoms along the edge of the clusters also help to stabilize the clusters. Previous experimental and theoretical data also proved that the change in cluster structure after depositing on a Au(111) surface is not significant under soft-landing conditions.[158-160,162,181]

6.3.2. Local work function of Mo_xS_y clusters (x/y: 2/6, 4/6, 6/8, 7/10) on Al_2O_3/NiAl(110) surface

The measured work function of the clean NiAl(110) surface is 4.86 eV which is consistent with previous experiments.[178,182,183] With the formation of the ultrathin alumina film, the work function decreases due to the compression of the intrinsic dipole layer at the interface.[184] In our experiments, the work function of the alumina film exhibits a slight variations between 4.38 eV and 4.47 eV which agrees well with the reported value of 4.2 ~ 4.6 eV depending on the oxygen exposure during oxidation.[178] Single photon photoemission from

Al_2O_3/NiAl(110) is observed with an photon energy of 4.6 eV. This signal is not from the excitation of the O2p valence band of Al_2O_3 because the valence band is located ~7 eV below the Fermi level.[178] An alternative explanation for the single photon photoemission is the presence of surface imperfections of the Al_2O_3 film which induces defect states within the Al_2O_3 band gap. The defect-induced states in the band gap are common for semiconductor surfaces and metal oxide films formed on metal substrates.[179,185]

The 2PPE spectra for the Mo_xS_y (x/y = 2/6, 4/6, 6/8, 7/10) clusters on the Al_2O_3/NiAl(110) surface exhibit similar behavior with changes in coverage. Therefore only the 2PPE spectra of Mo_6S_8 will be discussed in detail. Figure 6.2a shows the 2PPE spectra on Mo_6S_8/Al_2O_3/NiAl(110) with an average coverage of 0.3 ML. As discussed in section 6.3.1, the local cluster coverage decreases from the center to the edge of the deposition area. The 2PPE spectra were taken at several positions in the deposition area along the horizontal and vertical directions. The local cluster coverage within the focused beam area is regarded as a circle of 250 μm in diameter which was estimated in section 6.3.1. In this case, the highest local coverage at the center is 0.5 ML, where the cutoff of the 2PPE spectrum is located at 5.36 eV corresponding to the work function. From the center to the edge of cluster area, the cutoff of the 2PPE spectra shifts to lower final state energy. At the positions outside of the cluster region, the local work function is the same as that of the alumina film before cluster deposition. The local work function change follows an approximately linear relationship with the local cluster coverage as displayed in Figure 6.2b.

The local work function of Mo_6S_8 on alumina film is verified by the photoemission spectra with different photon energies as shown in Figure 6.3. At a photon energy of 4.71 eV (263 nm), single photon photoemission is observed on the bare alumina film (Figure 6.3a),

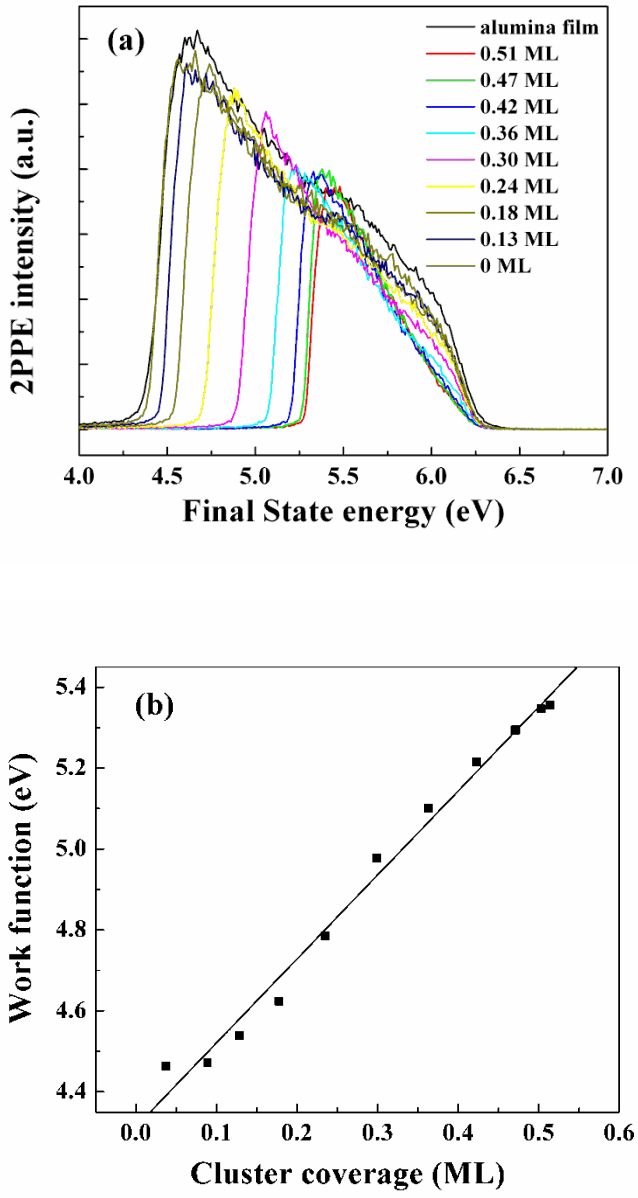

Figure 6.2: (a) 2PPE spectra of $Mo_6S_8/Al_2O_3/NiAl(110)$ with different local cluster coverage and aluminum oxide film without clusters covering. The Mo_6S_8 average cluster coverage is 0.3 ML and the excitation photon energy is 3.14 eV; (b) dependence of local work function of Mo_6S_8 clusters on $Al_2O_3/NiAl(110)$ as a function of cluster local coverage. The solid line is a linear fit with a slope of 2.07±0.08.

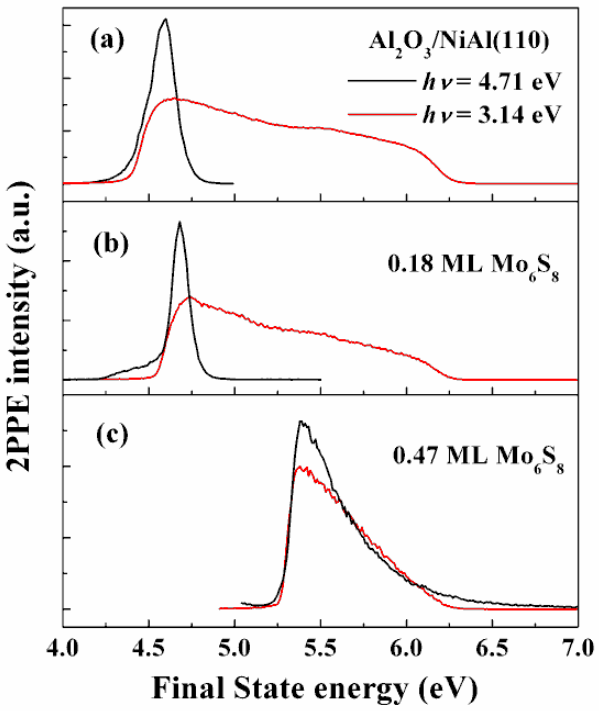

Figure 6.3: 2PPE spectra of Mo_6S_8/Al_2O_3/NiAl(110) and aluminum oxide film with different photon energies. Black line for 3rd harmonic light with photon energy of 4.71 eV and red line for 2nd harmonic light with photon energy of 3.14 eV. Because the cross section of one photon photoemission is a few orders of magnitude larger than that of two photon photoemission process, the laser power of 3rd harmonic light employed to obtain the spectra in (a) and (b) is more than 10 times lower than that of 2nd harmonic light in order to avoid saturating channeltron detector. (a) aluminum oxide film formed on NiAl(110) surface; (b) with local Mo_6S_8 coverage of 0.18 ML; (c) with local Mo_6S_8 coverage of 0.47 ML.

whereas photons at 3.14 eV (395 nm), can only produce photoelectrons by a two photon process. Nonetheless, the cutoff of the photoemission spectra for both photon energies have the same low energy cut-off corresponding to the work function. With Mo_6S_8 clusters of 0.18 ML (local cluster coverage, Figure 6.3b), both the one photon photoemission spectrum and two photon photoemission spectrum shift to a higher final state energy but still have the same cutoff, indicating that the change is correlated with the local work function. At a higher coverage of 0.47 ML (local cluster coverage, Figure 6.3c), light at 263 nm is no longer sufficient for one photon photoemission. The work function derived from these two spectra once again agrees with each other. The overlap of the low energy cutoff using different exciting photon energies and different photoexcitation processes provide confidence assigning the local work function.

The increase of the work function induced by the Mo_xS_y clusters is significant. For example, when the local cluster coverage is 0.5 ML, the increase of local work function for all Mo_xS_y clusters is more than 0.5 eV. The highest is 0.9 eV for the Mo_6S_8 cluster. The enhancement of the work function suggests that the electron transfer is from the substrate to the deposited clusters. By contrast, the work function change induced by clusters deposited on metal surface is much smaller. Previous UPS and 2PPE experiments on the deposited Mo_4S_6 clusters on Au(111) surface show that the work function increase is less than 0.1 eV even at high coverage.[158] DFT calculations for Mo_4S_6 and Mo_6S_8 on Au(111) also predict that the electron transfer donated from the Au surface to the clusters is negligible.[159,160] For example, the total electron transfer to Mo_4S_6 from Au is only 0.1 electron.[159] Significantly larger charge transfer has been observed for metals deposited on metal oxide films. For example, metal atoms like Cu, Au, Pt have been predicted to accept electrons and form full anions when deposited on MgO films on a Mo(100) substrate.[186] Gold monomers and chains formed on a ultrathin alumina film

on NiAl(110) surface are negative charged as well, as revealed by STM experiments and DFT calculations. The electron transferred from the substrate to an Au monomer is around one electron and up to three electrons for an Au_7 chain.[164,187] DFT calculations demonstrate that the large electron transfer is related to the adsorption structure of Au on the surface. Specifically, there are no stable adsorption sites for a Au trimer chain on the topmost oxygen layer of the oxygen terminated alumina film. The Au atoms at the end of the trimer chain are inclined to bind to the Al atoms underneath the topmost oxygen layer. As a result, the Al atoms are lifted above the surface plane and the bonds to interfacial oxygen ions in the layer below break. The broken bonds cause the electron transfer from Al atoms to the adsorbed Au atoms. Although the interfacial oxygen ion loses bond with Al atom, it is able to form another bond with Al atom in the NiAl substrate which helps to maintain a stable binding configuration.[187]

The most stable structures of the isolated Mo_4S_6 and Mo_6S_8 clusters have a Mo metallic core decorated with sulfur atoms.[158-160] When the clusters are deposited on the Au(111) surface, DFT calculations show that the clusters prefer to adsorb on the surface through sulfur atoms.[158-160] For example, the Mo_4S_6 cluster binds to the Au(111) surface through three S atoms at Au-Au bridging sites. On oxygen terminated Al_2O_3/NiAl(110) surface, the surface oxygen atoms are not able to form strong bonds with sulfur atoms of the clusters. Moreover, the molybdenum core atoms cannot be easily accessed by the oxygen atoms due to the steric effects of the surrounding sulfur atoms. A plausible adsorption geometry of Mo_xS_y clusters on alumina film is similar with that of Au atoms. The sulfur atoms bind to the Al atoms below the topmost oxygen layer and electron transfer from Al atoms to the clusters.

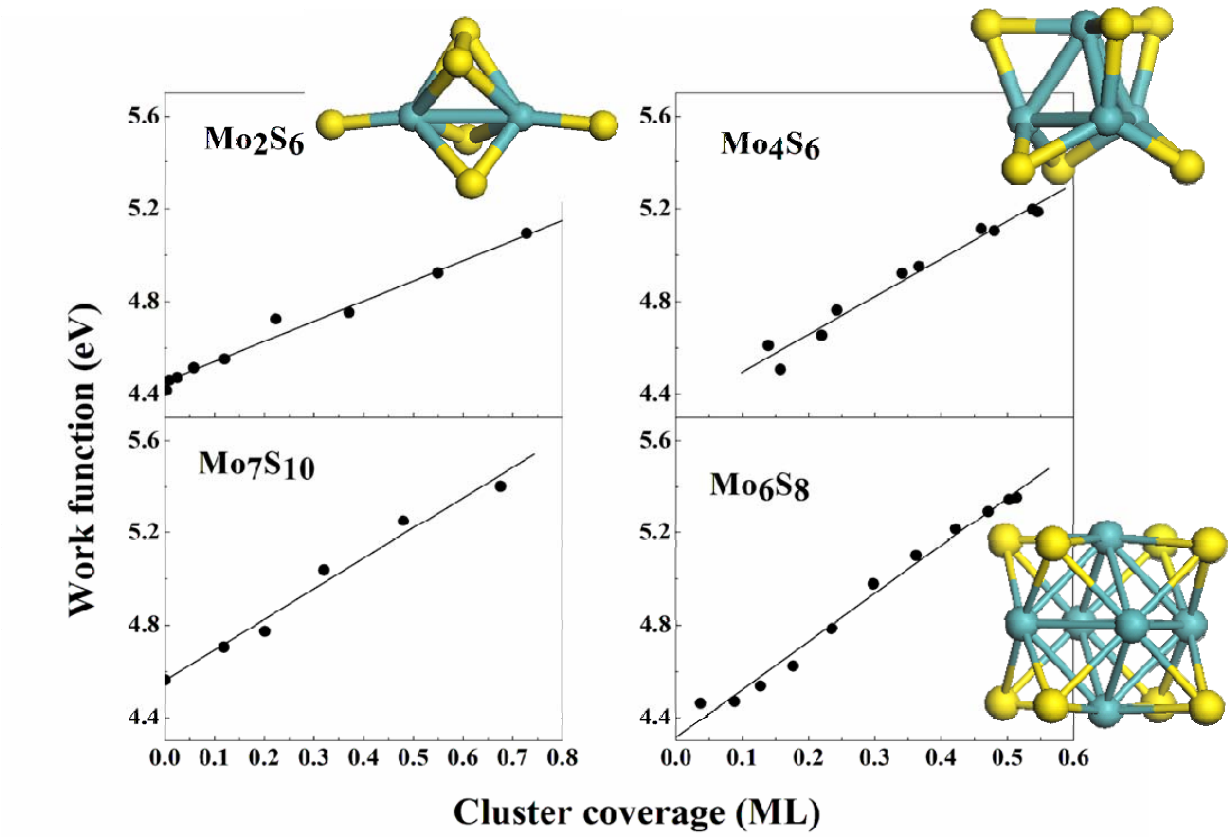

Figure 6.4: Dependence of local work function of different clusters (Mo_2S_6, Mo_4S_6, Mo_6S_8, Mo_7S_{10}) on Al_2O_3/NiAl(110) as a function of cluster local coverage. For Mo_2S_6, Mo_4S_6 and Mo_6S_8, the most stable structures optimized using DFT calculations are shown. Yellow: sulfur atoms; Blue: molybdenum atoms. Each solid line is a linear fit for the specific cluster.

6.3.3. Dipole moments of different Mo_xS_y clusters on Al_2O_3/NiAl(110) surface

The correlation between work function change and local cluster coverage for all clusters are shown in Figure 6.4. The solid lines in Figure 6.4 are linear fits to the experimental data obtained for the different clusters. The intercept at zero coverage corresponds to the work function of alumina film. The difference in the intercepts for different clusters is not related to the cluster properties but originates from the variation of the work function of alumina film as discussed in section 6.3.2. With the same cluster coverage, Mo_6S_8 induces the largest work function change and Mo_2S_6 has the smallest. Based on the work function and the cluster coverage, the dipole moments for each cluster at the interface can be calculated by the equation:

$$\Delta\Phi = (n \times e \times \mu)/\varepsilon_0 \qquad (6.1)$$

where μ is dipole moment at interface, n is the cluster density, e is the electronic charge and ε_0 is the vacuum permittivity.[118] The calculated dipole moments are shown in Table 6.1. As the cluster itself is symmetric and has no permanent dipole moment, the formation of the dipole moment is attributed to the electron transfer from the surface to the deposited clusters at the interface. With the proposed adsorption geometry for clusters discussed above, the electron transfer from Al atoms could be significant enough to result in observed interfacial dipole moments.

As shown by DFT calculations for the isolated neutral clusters, all four clusters studied here have similar sizes with a radius of 3 Å although they contain different number of atoms.[41,158] Therefore, the different interfacial dipole moments are unlikely size-dependent. Of the four clusters present here, Mo_4S_6 and Mo_6S_8 have highly symmetric structures. They have Mo atoms arranged in a tetrahedral (for Mo_4S_6) or octahedral (for Mo_6S_8) core with S atoms bridge-bonded along each edge.[41,158,160,188] Previous DFT calculations on the adsorption

Table 6.1: Interfacial dipole moments of different clusters on Al_2O_3/NiAl(110) surface derived from the change of local work function based on equation 6.1.

Cluster	Dipole moment (D)
Mo_2S_6	–0.65 ± 0.02
Mo_4S_6	–1.22 ± 0.07
Mo_6S_8	–1.55 ± 0.06
Mo_7S_{10}	–0.99 ± 0.10

geometries of Mo_4S_6 and Mo_6S_8 clusters on Au(111) surface demonstrated that they adsorb via a face and the number of sulfur atoms directly bond with Au atoms on the surface are three and four, respectively.[158-160] As discussed above, the cluster tends to bind to the Al atoms in the alumina film. The adsorption geometry for the cluster could be similar with that on Au(111) surface. There would be three and four S-Al bonds for Mo_4S_6 and Mo_6S_8 clusters respectively. Each of them has equal contribution to the interfacial dipole moment. Therefore, the dipole moment ratio of Mo_4S_6 to Mo_6S_8 at interface would be expected to 3:4 which agrees well with experimental data derived from the change of work function for Mo_4S_6 and Mo_6S_8. On the other hand, the structure of Mo_2S_6 is different than Mo_4S_6 and Mo_6S_8. It includes four Mo-S-Mo bridge bonds and two terminal sulfur bonds.[41] To our knowledge, the adsorption structure of Mo_2S_6 on a surface has not been studied. However, the less compacted cluster structure of Mo_2S_6 could lead to a large distortion when deposited on the surface and induces different interfacial dipole moment with those of Mo_4S_6 and Mo_6S_8 clusters. For Mo_7S_{10} cluster, the most stable structure is still unknown. It is possible that Mo_7S_{10} does not have a symmetric structure as those of Mo_4S_6 and Mo_6S_8. As a result, the interfacial dipole moment of Mo_7S_{10} on Al_2O_3/NiAl(110) surface is smaller than those of Mo_4S_6 and Mo_6S_8 on surface.

With the cluster coverage increasing, the intermolecular distance declines. Assuming that the clusters are uniformly distributed in the focused laser beam spot, the distance between closest clusters is small at a local coverage of 0.7 ML. However, the work function still follows the linear relationship with local cluster coverage. It indicates that the interaction between neighboring clusters is not strong enough to make a discernible contribution and the electronic properties observed are from individual clusters. It also suggests that the deposited cluster maintains its integrity on the surface and behaves independently, which is consistent with

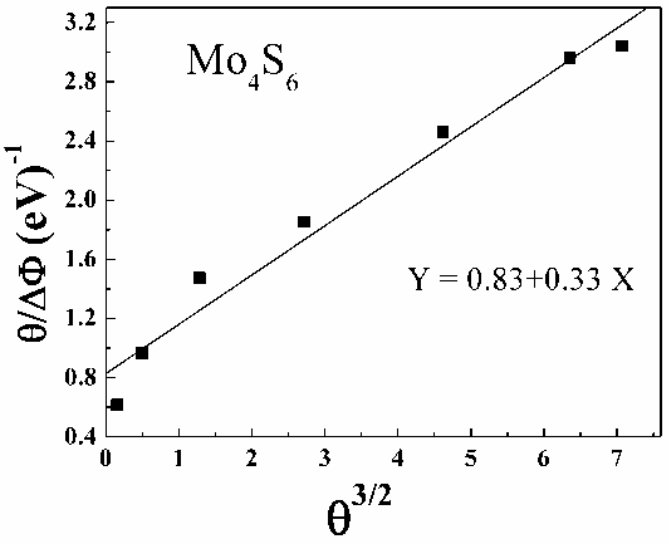

Figure 6.5: Plot of $\theta/\Delta\Phi$ vs $\theta^{3/2}$ for Mo_4S_6 on Al_2O_3/NiAl(110) surface. The average coverage of Mo_4S_6 is 1.0 ML. θ is the local cluster coverage and $\Delta\Phi$ is the change of work function at the corresponding coverage. The solid line is a linear fit with a slope of 0.33±0.03.

previous experimental and theoretical results.[158,159,162] With further enhancement of the clusters' coverage, the local work function increases slowly but does not grow with local cluster coverage linearly. For the case of Mo_4S_6 with a coverage of 1.0 ML over the whole deposition area, the highest work function at the center is 5.54 eV where the local coverage is 3.7 ML. The deviation from the linear relationship with cluster coverage is attributed to the depolarization effect. Considering the depolarization effect in a point-dipole model, the work function change can be described by the equation:[118]

$$\Delta\Phi = (n \times e \times \mu) / [(1 + 9 \times n^{3/2} \times \alpha) \times \varepsilon_0] \qquad (6.2)$$

where μ is dipole moment at interface, n is the cluster density, e is the electronic charge, α is effective polarizability and ε_0 is the vacuum permittivity. Equation (6.2) can be rearranged to

$$\theta/\Delta\Phi = (1/C_1) + (C_2/C_1) \times \theta^{3/2} \qquad (6.3)$$

where $C_1 = n_0 \times e \times \mu_0 / \varepsilon_0$, and $C_2 = 9 \times n_0^{3/2} \times \alpha$, θ is the cluster coverage with n_0 is the number of clusters at full monolayer coverage which is taken as 3.54×10^{18} atoms/m^2. Figure 6.5 shows the plot of $\theta/\Delta\Phi$ vs $\theta^{3/2}$ for Mo_4S_6 with an overall coverage of 1.0 ML. The dipole moment calculated from the linear fit is 0.90 Debye which agrees fairly well with the one (1.22 Debye) deduced from the work function change at low coverage. The effective polarizability is 6.64 Å^3. When the cluster coverage is high, the depolarization effect contradicts partly the effect from the increase of interfacial dipoles. As a result, the increase of the work function is small and not proportional to the cluster coverage anymore.

6.4. Summary

In this work, we have investigated the local work function of size-selected Mo_xS_y (x/y: 2/6, 4/6, 6/8, 7/10) clusters deposited on Al_2O_3/NiAl(110) surface. The four clusters display similar trends in cluster distribution on the surface and the local work function change. The cluster deposition area is obtained by Auger line scans and estimated to be 10~15 mm^2. The cluster density decreases from the center to the edge in the cluster deposition area. The work function of the clusters is larger than that on the alumina film and is proportional to the local cluster coverage. The increase of the work function indicates electron transfer from the surface to the clusters which is similar to the Au monomers and chains on alumina film.[164,187] The Al atoms below the topmost oxygen layer are the possible adsorption sites for the sulfur atoms in the cluster. No significant deviation from the linear relationship between the local work function and the cluster coverage is observed for a local cluster coverage up to ~0.7 ML where the intermolecular distance is small. It implies that the cluster is not damaged after deposition and the interaction between neighboring clusters is small. The dipole moments for each cluster are derived from the work function change. The Mo_6S_8 has the largest dipole moment of 1.55 D induced at the interface and Mo_2S_6 has the smallest one, 0.65 D. The different dipole moments are related to the cluster structures. The highly symmetric clusters, Mo_6S_8 and Mo_4S_6 have the two highest interfacial dipole moments. These results demonstrate that the Mo_xS_y clusters have strong interaction with the alumina film and the distinct electronic properties of different Mo_xS_y clusters might induce unique catalytic activities on the Al_2O_3 support.

List of References

(1) Lindstrom, C.D.; Zhu, X.Y. *Chem. Rev.* **2006**, *106*, 4281-4300.

(2) Salomon, A.; Cahen, D.; Lindsay, S.; Tomfohr, J.; Engelkes, V.B.; Frisbie, C.D. *Adv. Mater.* **2003**, *15*, 1881-1890.

(3) Adams, D.M.; Brus, L.; Chidsey, C.E.D.; Creager, S.; Creutz, C. *J. Phys. Chem. B* **2003**, *107*, 6668-6697.

(4) Zhu, X.Y. *Surf. Sci. Rep.* **2004**, *56*, 1-83.

(5) Gao, Y.L. *Acc. Chem. Res.* **1999**, *32*, 247-255.

(6) Ishii, H.; Sugiyama, K.; Ito, E.; Seki, K. *Adv. Mater.* **1999**, *11*, 605-+.

(7) Himpsel, F.J. *Adv. Phys.* **1983**, *32*, 1-51.

(8) Smith, N.V. *Rep. Prog. Phys.* **1988**, *51*, 1227-1294.

(9) Mujica, V.; Kemp, M.; Ratner, M.A. *J. Chem. Phys.* **1994**, *101*, 6856-6864.

(10) Mujica, V.; Kemp, M.; Ratner, M.A. *J. Chem. Phys.* **1994**, *101*, 6849-6855.

(11) Vondrak, T.; Wang, H.; Winget, P.; Cramer, C.J.; Zhu, X.Y. *J. Am. Chem. Soc.* **2000**, *122*, 4700-4707.

(12) Miller, A.D.; Gaffney, K.J.; Harris, C.B. *J. Phys. Chem. A* **2002**, *106*, 7636-7638.

(13) Camillone III, N.; Leung, T.Y.B.; Schwartz, P.; Eisenberger, P.; Scoles, G. *Langmuir* **1996**, *12*, 2737-2746.

(14) Poirier, G.E. *Chem. Rev.* **1997**, *97*, 1117-1128.

(15) Lindstrom, C.D.; Muntwiler, M.; Zhu, X.Y. *J. Phys. Chem. B* **2005**, *109*, 21492-21495.

(16) Perepichka, I.F.; Perepichka, D.F.; Meng, H.; Wudl, F. *Adv. Mater.* **2005**, *17*, 2281-2305.

(17) Fichou, D. *J. Mater. Chem.* **2000**, *10*, 571-588.

(18) Chu, C.; Ayres, J.A.; Stefanescu, D.M.; Walker, B.R.; Gorman, C.B.; Parsons, G.N. *J. Phys. Chem. C* **2007**, *111*, 8080-8085.

(19) Seminario, J.M.; De la Cruz, C.E.; Derosa, P.A. *J. Am. Chem. Soc.* **2001**, *123*, 5616-5617.

(20) Kim, B.; Beebe, J.M.; Jun, Y.; Zhu, X.Y.; Frisbie, C.D. *J. Am. Chem. Soc.* **2006**, *128*, 4970-4971.

(21) Woodruff, D.P. *Surf. Sci. Rep.* **2007**, *62*, 1-38.

(22) Gross, L.; Mohn, F.; Moll, N.; Meyer, G.; Ebel, R.; Abdel-Mageed, W.M.; Jaspars, M. *Nat. Chem.* **2010**, *2*, 821-825.

(23) Yoon, B.; Hakkinen, H.; Landman, U.; Worz, A.S.; Antonietti, J.M.; Abbet, S.; Judai, K.; Heiz, U. *Science* **2005**, *307*, 403-407.

(24) Matthey, D.; Wang, J.G.; Wendt, S.; Matthiesen, J.; Schaub, R.; Laegsgaard, E.; Hammer, B.; Besenbacher, F. *Science* **2007**, *315*, 1692-1696.

(25) Chianelli, R.R.; Berhault, G.; Torres, B. *Catal. Today* **2009**, *147*, 275-286.

(26) Valden, M.; Lai, X.; Goodman, D.W. *Science* **1998**, *281*, 1647-1650.

(27) Chen, M.S.; Goodman, D.W. *Science* **2004**, *306*, 252-255.

(28) Lauritsen, J.V.; Kibsgaard, J.; Helveg, S.; Topsoe, H.; Clausen, B.S.; Laegsgaard, E.; Besenbacher, F. *Nat. Nanotechnol.* **2007**, *2*, 53-58.

(29) Lauritsen, J.V.; Bollinger, M.V.; Laegsgaard, E.; Jacobsen, K.W.; Norskov, J.K.; Clausen, B.S.; Topsoe, H.; Besenbacher, F. *J. Catal.* **2004**, *221*, 510-522.

(30) Besenbacher, F.; Brorson, M.; Clausen, B.S.; Helveg, S.; Hinnemann, B. *Catal. Today* **2008**, *130*, 86-96.

(31) J.K. Ranka, A.L.G. *Opt. Lett.* **1997**, *22*, 1344.

(32) Yariv, A. *Quantum Electronics*; John Wiley & Sons Inc. , 1989.

(33) Szymanski, P.; Garrett-Roe, S.; Harris, C.B. *Prog. Surf. Sci.* **2005**, *78*, 1-39.

(34) Haberland, H.; Karrais, M.; Mall, M.; Thurner, Y. *J. Vac. Sci. Technol., A* **1992**, *10*, 3266-3271.

(35) Haberland, H.; Mall, M.; Moseler, M.; Qiang, Y.; Reiners, T.; Thurner, Y. *J. Vac. Sci. Technol., A* **1994**, *12*, 2925-2930.

(36) Dawson, P.H. *Quadrupole mass spectrometry and its applications*; Elsevier, Amsterdam, 1976.

(37) Wortmann, B.; Mende, K.; Duffe, S.; Gronhagen, N.; von Issendorff, B.; Hovel, H. *Phys. Status Solidi B 247*, 1116-1121.

(38) Busolt, U.; Cottancin, E.; Rohr, H.; Socaciu, L.; Leisner, T.; Woste, L. *Eur. Phys. J. D* **1999**, *9*, 523-527.

(39) Meiwes-Broer, K.-H., *Metal Clusters at Surfaces*; Springer-Verlag, Berlin, 2000.

(40) Kretzschmar, I.; Schroder, D.; Schwarz, H.; Rue, C.; Armentrout, P.B. *J. Phys. Chem. A* **2000**, *104*, 5046-5058.

(41) Patterson, M.J.; Lightstone, J.M.; White, M.G. *J. Phys. Chem. A* **2008**, *112*, 12011-12021.

(42) Redhead, P.A. *Vacuum* **1962**, *12*, 203-211.

(43) Powell, C.J.J., A. NIST Electron Inelastic-Mean-Free-Path Database, ed. 1.1; National Institute of Standards and Technology, Gaithersburg, MD, 2000.

(44) Watts, J.F.W., J *An introduction to surface analysis by XPS and AES*; John Wiley & Sons Ltd: Chichester, England, 2003.

(45) Flink, S.; van Veggel, F.; Reinhoudt, D.N. *Adv. Mater.* **2000**, *12*, 1315-1328.

(46) Balzani, V.; Credi, A.; Venturi, M. *Chem.-Eur. J.* **2008**, *14*, 26-39.

(47) Zhu, X.Y. *J. Phys. Chem. B* **2004**, *108*, 8778-8793.

(48) Magoga, M.; Joachim, C. *Phys. Rev. B* **1997**, *56*, 4722.

(49) Zhong, Q.; Gahl, C.; Wolf, M. *Surf. Sci.* **2002**, *496*, 21-32.

(50) Nambu, A.; Kondoh, H.; Nakai, I.; Amemiya, K.; Ohta, T. *Surf. Sci.* **2003**, *530*, 101-110.

(51) Milligan, P.K.; Murphy, B.; Lennon, D.; Cowie, B.C.C.; Kadodwala, M. *J. Phys. Chem. B* **2001**, *105*, 140-148.

(52) Nara, J.; Higai, S.; Morikawa, Y.; Ohno, T. *Appl. Surf. Sci.* **2004**, *237*, 433-438.

(53) Matsuura, T.; Nakajima, M.; Shimoyama, Y. *Jpn. J. Appl. Phys., Part 1* **2001**, *40*, 6945-6950.

(54) Matsuura, T.; Shimoyama, Y. *Eur. Phys. J. E* **2002**, *7*, 233-240.

(55) Chen, X.; Frank, E.R.; Hamers, R.J. *J. Vac. Sci. Technol., B* **1996**, *14*, 1136-1140.

(56) Su, G.J.; Zhang, H.M.; Wan, L.J.; Bai, C.L. *Surf. Sci.* **2003**, *531*, L363-L368.

(57) Sony, P.; Puschnig, P.; Nabok, D.; Ambrosch-Draxl, C. *Phys. Rev. Lett.* **2007**, *99*, 176401-176404.

(58) Roncali, J. *Chem. Rev.* **1997**, *97*, 173-206.

(59) Roncali, J. *Handbook of Oligo- and Polythiophenes*; Wiley-VCH: Werheim, Germany, 1999.

(60) Delley, B. *J. Chem. Phys.* **1990**, *92*, 508-517.

(61) Delley, B. *J. Chem. Phys.* **2000**, *113*, 7756-7764.

(62) Perdew, J.P.; Chevary, J.A.; Vosko, S.H.; Jackson, K.A.; Pederson, M.R.; Singh, D.J.; Fiolhais, C. *Phys. Rev. B* **1992**, *46*, 6671.

(63) Monkhorst, H.J.; Pack, J.D. *Phys. Rev. B* **1976**, *13*, 5188.

(64) Liu, G.; Rodriguez, J.A.; Dvorak, J.; Hrbek, J.; Jirsak, T. *Surf. Sci.* **2002**, *505*, 295-307.

(65) Fawcett, F.S.; Rasmussen, H.E. *J. Am. Chem. Soc.* **1945**, *67*, 1705-1709.

(66) Noh, J.; Ito, E.; Nakajima, K.; Kim, J.; Lee, H.; Hara, M. *J. Phys. Chem. B* **2002**, *106*, 7139-7141.

(67) Hansson, G.V.; Flodstrom, S.A. *Phys. Rev. B* **1978**, *18*, 1572-1585.

(68) Hussain, Z.; Smith, N.V. *Phys. Lett. A* **1978**, *66*, 492-494.

(69) Whelan, C.M.; Barnes, C.J.; Walker, C.G.H.; Brown, N.M.D. *Surf. Sci.* **1999**, *425*, 195-211.

(70) Qiao, M.H.; Cao, Y.; Tao, F.; Liu, Q.; Deng, J.F.; Xu, G.Q. *J. Phys. Chem. B* **2000**, *104*, 11211-11219.

(71) Lindstrom, C.; Dutton, G.; Quinn, D.P.; Zhu, X.Y. *Isr. J. Chem.* **2005**, *45*, 195-203.

(72) Lindstrom, C.D.; Muntwiler, M.; Zhu, X.Y. *J. Phys. Chem. B* **2007**, *111*, 6913-6920.

(73) Gudde, J.; Berthold, W.; Hofer, U. *Chem. Rev.* **2006**, *106*, 4261-4280.

(74) Hotzel, A. *Prog. Surf. Sci.* **2007**, *82*, 336-354.

(75) Petek, H.; Ogawa, S. *Prog. Surf. Sci.* **1997**, *56*, 239-310.

(76) Wolf, M.; Hotzel, A.; Knoesel, E.; Velic, D. *Phys. Rev. B* **1999**, *59*, 5926-5935.

(77) Steinmann, W. *Phys. Status Solidi B* **1995**, *192*, 339.

(78) Fauster, T.; Steinmann, W. *Photonic probes of surfaces, electromagnetic waves: recent developments in research*; North-Holland: Amsterdam, 1995; Vol. 2.

(79) Wolf, M.; Tegeder, P. *Surf. Sci.* **2009**, *603*, 1506-1517.

(80) Palmer, M.H.; Walker, I.C.; Guest, M.F. *Chem. Phys.* **1999**, *241*, 275-296.

(81) Weinkauf, R.; Lehr, L.; Schlag, E.W.; Salzmann, S.; Marian, C.M. *Phys. Chem. Chem. Phys.* **2008**, *10*, 393-404.

(82) Dutton, G.; Pu, J.; Truhlar, D.G.; Zhu, X.Y. *J. Chem. Phys.* **2003**, *118*, 4337-4340.

(83) Wang, H.F.; Dutton, G.; Zhu, X.Y. *J. Phys. Chem. B* **2000**, *104*, 10332-10338.

(84) Ryu, S.M.; Chang, J.Y.; Kim, S.K. *J. Chem. Phys.* **2005**, *123*, 9.

(85) Weaver, J.H., Krafka, C., Lynch, D. W., Koch, E. E. *Physics data*; Fachinformationszentrum, Karlsruhe, 1981; Vol. 18.

(86) Yu, M.; Driver, S.M.; Woodruff, D.P. *Langmuir* **2005**, *21*, 7285-7291.

(87) Noh, J.; Hara, M. *Langmuir* **2001**, *17*, 7280-7285.

(88) Poirier, G.E.; Tarlov, M.J. *Langmuir* **1994**, *10*, 2853-2856.

(89) Camillone III, N.; Chidsey, C.E.D.; Liu, G.-Y.; Scoles, G. *J. Chem. Phys.* **1993**, *98*, 3503-3511.

(90) Chidsey, C.E.D.; Loiacono, D.N. *Langmuir* **1990**, *6*, 682-691.

(91) Bacon, G.E. *Acta Crystallogr.* **1951**, *4*, 558.

(92) Dishner, M.H.; Hemminger, J.C.; Feher, F.J. *Langmuir* **1996**, *12*, 6176-6178.

(93) Vondrak, T.; Zhu, X.Y. *J. Phys. Chem. B* **1999**, *103*, 3449-3456.

(94) Dutton, G.; Quinn, D.P.; Lindstrom, C.D.; Zhu, X.Y. *Phys. Rev. B* **2005**, *72*.

(95) Dutton, G.; Zhu, X.Y. *J. Phys. Chem. B* **2002**, *106*, 5975-5981.

(96) Abe, T. *J. Phys. Chem.* **1986**, *90*, 713-715.

(97) Tegeder, P.; Balog, R.; Mason, N.J.; Illenberger, E. *Phys. Chem. Chem. Phys.* **2005**, *7*, 685-690.

(98) *CRC Handbook of chemistry and physics*; CRC, 2009.

(99) Jones, D.; Guerra, M.; Favaretto, L.; Modelli, A.; Fabrizio, M.; Distefano, G. *J. Phys. Chem.* **1990**, *94*, 5761-5766.

(100) Fahlman, M.; Crispin, A.; Crispin, X.; Henze, S.K.M.; de Jong, M.P.; Osikowicz, W.; Tengstedt, C.; Salaneck, W.R. *J. Phys.: Condens. Matter* **2007**, *19*, 183202.

(101) Kind, M.; Woll, C. *Prog. Surf. Sci.* **2009**, *84*, 230-278.

(102) Schoenfisch, M.H.; Pemberton, J.E. *J. Am. Chem. Soc.* **1998**, *120*, 4502-4513.

(103) Jang, Y.H.; Goddard, W.A. *J. Phys. Chem. C* **2010**, *114*, 4646-4651.

(104) Willey, T.M.; Vance, A.L.; van Buuren, T.; Bostedt, C.; Terminello, L.J.; Fadley, C.S. *Surf. Sci.* **2005**, *576*, 188-196.

(105) Hong, S.; Reifenberger, R.; Tian, W.; Datta, S.; Henderson, J.I.; Kubiak, C.P. *Superlattices Microstruct.* **2000**, *28*, 289-303.

(106) Caruso, A.N.; Rajesh, R.; Gallup, G.; Redepenning, J.; Dowben, P.A. *J. Phys. Chem. B* **2004**, *108*, 6910-6914.

(107) Li, Y.; Lu, D.Y.; Swanson, S.A.; Scott, J.C.; Galli, G. *J. Phys. Chem. C* **2008**, *112*, 6413-6421.

(108) Xue, Y.Q.; Ratner, M.A. *Phys. Rev. B* **2004**, *69*, 085403.

(109) Toher, C.; Sanvito, S. *Phys. Rev. Lett.* **2007**, *99*, 056801.

(110) Li, Y.; Lu, D.Y.; Galli, G. *J. Chem. Theory Comput.* **2009**, *5*, 881-886.

(111) Angelici, R.J.; Lazar, M. *Inorg. Chem.* **2008**, *47*, 9155-9165.

(112) Henderson, J.I., Feng, S., Bein, T., Kubiak, C.P. *Langmuir* **2000**, *16*, 6183-6187.

(113) Murphy, K.L., Tysoe, W.T., Bennett, D.W. *Langmuir* **2004**, *20*, 1732-1738.

(114) Swanson, S.A.; McClain, R.; Lovejoy, K.S.; Alamdari, N.B.; Hamilton, J.S.; Scott, J.C. *Langmuir* **2005**, *21*, 5034-5039.

(115) Boscoboinik, J.A.; Calaza, F.C.; Habeeb, Z.; Bennett, D.W.; Stacchiola, D.J.; Purino, M.A.; Tysoe, W.T. *Phys. Chem. Chem. Phys.* **2010**, *12*, 11624-11629.

(116) Zhou, J.; Yang, Y.X.; Liu, P.; Camillone, N.; White, M.G. *J. Phys. Chem. C* **2010**, *114*, 13670-13677.

(117) Sohn, Y.; White, J.M. *J. Phys. Chem. C* **2008**, *112*, 5006-5013.

(118) Schmidt, L.D.; Gomer, R. *J. Chem. Phys.* **1966**, *45*, 1605-1623.

(119) Katano, S.; Herceg, E.; Trenary, M.; Kim, Y.; Kawai, M. *J. Phys. Chem. B* **2006**, *110*, 20344-20349.

(120) Zangmeister, C.D.; Robey, S.W.; van Zee, R.D.; Kushmerick, J.G.; Naciri, J. *J. Phys. Chem. B* **2006**, *110*, 17138-17144.

(121) Lindstrom, C.D.; Quinn, D.; Zhu, X.Y. *J. Chem. Phys.* **2005**, *122*, 124714.

(122) Stapleton, J.J.; Daniel, T.A.; Uppili, S.; Cabarcos, O.M.; Naciri, J.; Shashidhar, R.; Allara, D.L. *Langmuir* **2005**, *21*, 11061-11070.

(123) Ito, M.; Noguchi, H.; Ikeda, K.; Uosaki, K. *Phys. Chem. Chem. Phys.* **2010**, *12*, 3156-3163.

(124) Lin, S.; McCarley, R.L. *Langmuir* **1999**, *15*, 151-159.

(125) Kim, S.; Ihm, K.; Kang, T.H.; Hwang, S.; Joo, S.W. *Surf. Interface Anal.* **2005**, *37*, 294-299.

(126) Esplandiu, M.J.; Carot, M.L.; Cometto, F.P.; Macagno, V.A.; Patrito, E.M. *Surf. Sci.* **2006**, *600*, 155-172.

(127) Zhang, J.M.; Song, X.L.; Zhang, X.J.; Xu, K.W.; Ji, V. *Surf. Sci.* **2006**, *600*, 1277-1282.

(128) Maksymovych, P.; Voznyy, O.; Dougherty, D.B.; Sorescu, D.C.; Yates, J.T. *Prog. Surf. Sci.* **2010**, *85*, 206-240.

(129) Wong, Y.T.; Hoffmann, R. *J. Phys. Chem.* **1991**, *95*, 859-867.

(130) Nilsson, A.; Pettersson, L.G.M. *Surf. Sci. Rep.* **2004**, *55*, 49-167.

(131) Ikeda, K.; Fujimoto, N.; Uehara, H.; Uosaki, K. *Chem. Phys. Lett.* **2008**, *460*, 205-208.

(132) Love, J.C.; Estroff, L.A.; Kriebel, J.K.; Nuzzo, R.G.; Whitesides, G.M. *Chem. Rev.* **2005**, *105*, 1103-1169.

(133) Vericat, C.; Vela, M.E.; Benitez, G.; Carro, P.; Salvarezza, R.C. *Chem. Soc. Rev.* **2010**, *39*, 1805-1834.

(134) Gao, W.W.; Baker, T.A.; Zhou, L.; Pinnaduwage, D.S.; Kaxiras, E.; Friend, C.M. *J. Am. Chem. Soc.* **2008**, *130*, 3560-3565.

(135) Voznyy, O.; Dubowski, J.J.; Yates, J.T.; Maksymovych, P. *J. Am. Chem. Soc.* **2009**, *131*, 12989-12993.

(136) Woll, C.; Chiang, S.; Wilson, R.J.; Lippel, P.H. *Phys. Rev. B* **1989**, *39*, 7988-7991.

(137) Ibe, J.P.; Bey, P.P.; Brandow, S.L.; Brizzolara, R.A.; Burnham, N.A.; Dilella, D.P.; Lee, K.P.; Marrian, C.R.K.; Colton, R.J. *J. Vac. Sci. Technol., A* **1990**, *8*, 3570-3575.

(138) Nakamura, Y.; Mera, Y.; Maeda, K. *Rev. Sci. Instrum.* **1999**, *70*, 3373-3376.

(139) Zahl, P.; Bierkandt, M.; Schroder, S.; Klust, A. *Rev. Sci. Instrum.* **2003**, *74*, 1222-1227.

(140) Zahl, P.; Wagner, T.; Moller, R.; Klust, A. *J. Vac. Sci. Technol., B* **2010**, *28*, C4E39-C34E47.

(141) Giannozzi, P.; Baroni, S.; Bonini, N.; Calandra, M.; Car, R. *J. Phys.: Condens. Matter* **2009**, *21*, 395502.

(142) Perdew, J.P.; Burke, K.; Ernzerhof, M. *Phys. Rev. Lett.* **1996**, *77*, 3865-3868.

(143) Monkhorst, H.J.; Pack, J.D. *Phys. Rev. B* **1976**, *13*, 5188-5192.

(144) Driver, S.M.; Zhang, T.F.; King, D.A. *Angew. Chem.-Int. Edit.* **2007**, *46*, 700-703.

(145) Maksymovych, P.; Sorescu, D.C.; Yates, J.T. *Phys. Rev. Lett.* **2006**, *97*.

(146) Kiguchi, M.; Miura, S.; Hara, K.; Sawamura, M.; Murakoshi, K. *Appl. Phys. Lett.* **2006**, *89*.

(147) Bellisario, D.O.; Jewell, A.D.; Tierney, H.L.; Baber, A.E.; Sykes, E.C.H. *J. Phys. Chem. C* **2010**, *114*, 14583-14589.

(148) Zhang, J.D.; Chi, Q.J.; Ulstrup, J. *Langmuir* **2006**, *22*, 6203-6213.

(149) Vitali, L.; Levita, G.; Ohmann, R.; Comisso, A.; De Vita, A.; Kern, K. *Nat. Mater.* **2010**, *9*, 320-323.

(150) Bocquet, M.L.; Wang, B. *Prog. Surf. Sci.* **2010**, *85*, 435-459.

(151) Brorson, M.; Carlsson, A.; Topsoe, H. *Catal. Today* **2007**, *123*, 31-36.

(152) Helveg, S.; Lauritsen, J.V.; Laegsgaard, E.; Stensgaard, I.; Norskov, J.K.; Clausen, B.S.; Topsoe, H.; Besenbacher, F. *Phys. Rev. Lett.* **2000**, *84*, 951-954.

(153) Lauritsen, J.V.; Nyberg, M.; Vang, R.T.; Bollinger, M.V.; Clausen, B.S. *Nanotechnology* **2003**, *14*, 385-389.

(154) Chikan, V.; Kelley, D.F. *J. Phys. Chem. B* **2002**, *106*, 3794-3804.

(155) Wilcoxon, J.P.; Samara, G.A. *Phys. Rev. B* **1995**, *51*, 7299-7302.

(156) Tuxen, A.; Kibsgaard, J.; Gobel, H.; Laegsgaard, E.; Topsoe, H.; Lauritsen, J.V.; Besenbacher, F. *ACS Nano* **2010**, *4*, 4677-4682.

(157) Bertram, N.; Kim, Y.D.; Gantefor, G.; Sun, Q.; Jena, P.; Tamuliene, J.; Seifert, G. *Chem. Phys. Lett.* **2004**, *396*, 341-345.

(158) Lightstone, J.M.; Patterson, M.J.; Liu, P.; Lofaro, J.C.; White, M.G. *J. Phys. Chem. C* **2008**, *112*, 11495-11506.

(159) Gemming, S.; Seifert, G. *Appl. Phys. A-Mater. Sci. Process.* **2006**, *82*, 175-179.

(160) Popov, I.; Gemming, S.; Seifert, G. *Phys. Rev. B* **2007**, *75*, 245436.

(161) Gemming, S.; Tamuliene, J.; Seifert, G.; Bertram, N.; Kim, Y.D.; Gantefor, G. *Appl. Phys. A-Mater. Sci. Process.* **2006**, *82*, 161-166.

(162) Popov, I.; Kunze, T.; Gemming, S.; Seifert, G. *Eur. Phys. J. D* **2007**, *45*, 439-446.

(163) Baumer, M.; Freund, H.J. *Prog. Surf. Sci.* **1999**, *61*, 127-198.

(164) Nilius, N.; Ganduglia-Pirovano, M.V.; Brazdova, V.; Kulawik, M.; Sauer, J.; Freund, H.J. *Phys. Rev. Lett.* **2008**, *100*, 096802.

(165) Worren, T.; Hansen, K.H.; Laegsgaard, E.; Besenbacher, F.; Stensgaard, I. *Surf. Sci.* **2001**, *477*, 8-16.

(166) Martinez, U.; Jerratsch, J.F.; Nilius, N.; Giordano, L.; Pacchioni, G.; Freund, H.J. *Phys. Rev. Lett.* **2009**, *103*, 056801.

(167) Kulawik, M.; Nilius, N.; Rust, H.P.; Freund, H.J. *Phys. Rev. Lett.* **2003**, *91*, 256101.

(168) Simon, G.H.; Konig, T.; Rust, H.P.; Heyde, M.; Freund, H.J. *New J. Phys.* **2009**, *11*, 093009.

(169) Stierle, A.; Renner, F.; Streitel, R.; Dosch, H.; Drube, W.; Cowie, B.C. *Science* **2004**, *303*, 1652-1656.

(170) Kresse, G.; Schmid, M.; Napetschnig, E.; Shishkin, M.; Kohler, L.; Varga, P. *Science* **2005**, *308*, 1440-1442.

(171) Frank, M.; Baumer, M. *Phys. Chem. Chem. Phys.* **2000**, *2*, 3723-3737.

(172) Sommerhalter, C.; Matthes, T.W.; Glatzel, T.; Jager-Waldau, A.; Lux-Steiner, M.C. *Appl. Phys. Lett.* **1999**, *75*, 286-288.

(173) Sasahara, A.; Pang, C.L.; Onishi, H. *J. Phys. Chem. B* **2006**, *110*, 17584-17588.

(174) Sasahara, A.; Uetsuka, H.; Onishi, H. *Surf. Sci.* **2003**, *529*, L245-L250.

(175) Schmid, M.; Shishkin, M.; Kresse, G.; Napetschnig, E.; Varga, P.; Kulawik, M.; Nilius, N.; Rust, H.P.; Freund, H.J. *Phys. Rev. Lett.* **2006**, *97*, 046101.

(176) Heinke, L.; Lichtenstein, L.; Simon, G.H.; Konig, T.; Heyde, M.; Freund, H.J. *Phys. Rev. B* **2010**, *82*, 075430.

(177) Heinke, L.; Lichtenstein, L.; Simon, G.H.; Konig, T.; Heyde, M.; Freund, H.J. *ChemPhysChem* **2010**, *11*, 2085-2087.

(178) Song, W.J.; Yoshitake, M. *Appl. Surf. Sci.* **2005**, *251*, 14-18.

(179) Vaida, M.E.; Gleitsmann, T.; Tchitnga, R.; Bernhardt, T.M. *J. Phys. Chem. C* **2009**, *113*, 10264-10268.

(180) Busolt, U.; Cottancin, E.; Rohr, H.; Socaciu, L.; Leisner, T.; Woste, L. *Appl. Phys. B-Lasers Opt.* **1999**, *68*, 453-457.

(181) Duffe, S.; Irawan, T.; Bieletzki, M.; Richter, T.; Sieben, B.; Yin, C.; Issendorff, B.; Moseler, M.; Hovel, H. *Eur. Phys. J. D* **2007**, *45*, 401-408.

(182) Hanbicki, A.T.; Rous, P.J.; Plummer, E.W. *Phys. Rev. B* **2003**, *67*, 205405.

(183) Tzvetkov, G.; Ramsey, M.G.; Netzer, F.P. *Surf. Sci.* **2003**, *526*, 383-393.

(184) Benia, H.M.; Nilius, N.; Freund, H.J. *Surf. Sci.* **2007**, *601*, L55-L58.

(185) Onda, K.; Li, B.; Petek, H. *Phys. Rev. B* **2004**, *70*.

(186) Sicolo, S.; Giordano, L.; Pacchioni, G. *J. Phys. Chem. C* **2009**, *113*, 16694-16701.

(187) Nilius, N.; Ganduglia-Pirovano, M.V.; Brazdova, V.; Kulawik, M.; Sauer, J.; Freund, H.J. *Phys. Rev. B* **2010**, *81*, 045422.

(188) Lightstone, J.M.; Patterson, M.J.; White, M.G. *Chem. Phys. Lett.* **2005**, *413*, 429-433.